Wavelet based multifractal formalism: Applications to DNA sequences, satellite images of the cloud structure and stock market data

A. Arneodo, B. Audit, N. Decoster, J-F. Muzy, and C. Vaillant

1   Introduction

In the real world, it is often the case that a wide range of scales is needed to characterize physical properties. Actually, multi-scale phenomena seem to be ubiquitous in nature. A paradigmatic illustration of such situation are *fractals* which are complex mathematical objects that have no minimal natural length scale. The relevance of fractals to physics and many other fields was pointed out by Mandelbrot [1] who demonstrated the richness of fractal geometry and stimulated many theoretical, numerical and experimental studies. Actually, in many situations in physics as well as in some applied sciences, one is faced to the problem of characterizing very irregular functions [1–20]. The examples range from plots of various kinds of random walks, e.g., Brownian signals [21, 22], to financial time-series [19, 20, 23], to geologic shapes [1, 16], to medical time-series [9, 13, 14] , to interface developing in far from equilibrium growth processes [6, 10, 17], to turbulent velocity signals [15] and to DNA "walks" coding nucleotide sequences [24–26]. These functions can be qualified as *fractal functions* [1, 22, 27, 28] whenever their graphs are fractal sets in $\mathbb{R}^2$ (in this introduction we will only consider functions from $\mathbb{R}$ to $\mathbb{R}$). They are commonly called *self-affine* functions since their graphs are self-affine sets which are similar to themselves when transformed by anisotropic dilations, *i.e.*, when shrinking along the x-axis by a factor λ followed by a rescaling of the increments of the function by a different factor λ^{-H}. This can be stated mathematically in the following way: if $f(x)$ is a self-affine function then, $\forall x_0 \in \mathbb{R}$, $\exists H \in \mathbb{R}$ such that for any $\lambda > 0$, one has

$$f(x_0 + \lambda x) - f(x_0) \simeq \lambda^H \left(f(x_0 + x) - f(x_0) \right) . \tag{1}$$

If f is a stochastic process, this identity holds in law for fixed λ and x_0. The exponent H is called the *roughness* or Hurst exponent [1, 5, 10]. Let us note that if $H < 1$, then

f is not differentiable and the smaller the exponent H, the more singular f. Thus the Hurst exponent provides indication of how globally irregular the function f is. Indeed H is supposed to be related to the fractal dimension $D_F = 2 - H$ of the graph of f [1, 5, 10, 22].

In various contexts, several methods have been used to estimate the Hurst exponent. For instance, for the growth of rough surfaces [5, 6, 10, 17, 18], the average height difference between points separated by a distance l has been considered to scale as:

$$< |f(x + l) - f(x)| > \sim l^H . \tag{2}$$

Alternatively, the root-mean square (r.m.s.) of the height fluctuations over a distance l is a quantitative measure of the width or thickness of the rough interface [5, 6, 10, 17, 18]:

$$w(l) = \left[< f^2 >_l - < f >_l^2 \right]^{1/2} \sim l^H . \tag{3}$$

Note that in the pioneering analysis of DNA sequences [24, 25], the r.m.s. fluctuations about the average displacement of the DNA walk has been mainly used to detect the presence of long-range correlations ($H \neq 1/2$). A more classical method consists in investigating the scaling behavior of the power spectrum as a function of the wavevector k [1–20]:

$$S(k) \sim k^{-(2H+1)} . \tag{4}$$

But some care is required when using these methods, since they may lead to conflicting estimates of the Hurst exponent [29, 30]. Limited resolution as well as finite-size effects are well known to introduce biases in the estimate of H. Moreover, on a more fundamental ground, these methods are not adapted when the fractal function under consideration is not an homogeneous fractal function with a constant roughness associated to a unique exponent H [31, 32].

Fractal functions can possess multi-affine properties in the sense that their roughness (or regularity) may fluctuate from point to point [31–36]. To describe these *multifractal* functions, one thus needs to change slightly the definition of the Hurst regularity of f so that it becomes a local quantity [31, 32]:

$$|f(x + l) - f(x)| \sim l^{h(x)} . \tag{5}$$

This "local Hurst exponent" $h(x)$ is generally call the *Hölder exponent* of f at the point x. A more rigourous definition of the Hölder exponent, as the strength of the singularity of a function f at the point x_0, is given by the largest exponent such that there exists a polynomial $P_n(x - x_0)$ of order $n < h(x_0)$ and a constant $C > 0$, so that for any point x in the neighborhood of x_0, one has [37–42]:

$$|f(x) - P_n(x - x_0)| \leq C|x - x_0|^h . \tag{6}$$

If f is n times continuously differentiable at the point x_0, then one can use for the polynomial $P_n(x - x_0)$, the order-n Taylor series of f at x_0 and thus prove that $h(x_0) > n$. Thus

$h(x_0)$ measures how irregular the function f is at the point x_0. The higher the exponent $h(x_0)$, the more regular the function f.

The aim of a quantitative theory of multi-affine functions is to provide mathematical concepts and numerical tools for the description of the fluctuations of regularity of these objects based on some limited amount of information. In the early eighties, a phemomenological approach to the characterization of fractal objects has been proposed and advanced: the *multifractal formalism* [43–51]. In its original form, this approach was essentially adapted to describe statistically the scaling properties of *singular measures* [45, 46, 51]. Notable examples include the invariant probability distribution on a strange attractor [45, 46, 51] , the distribution of voltage drops across a random resistor network [2, 5, 11], the distribution of growth probabilities on the boundary of a diffusion-limited aggregate [5, 6, 52] and the spatial distribution of dissipative regions in a turbulent flow [15, 48, 53, 54]. This formalism relies upon the determination of the so-called $f(\alpha)$ *singularity spectrum* [45], which characterizes the relative contribution of each singularity of the measure: let S_α be the subset of points x where the measure of an ϵ-box $B_x(\epsilon)$, centered at x, scales like $\mu(B_x(\epsilon)) \sim \epsilon^\alpha$ in the limit $\epsilon \rightarrow 0^+$, then, by definition, $f(\alpha)$ is the Hausdorff dimension of S_α: $f(\alpha) = \dim_{\mathrm{H}}(S_\alpha)$. Actually, there exists a deep analogy that links the multifractal formalism with that of statistical thermodynamics [55–57]. This analogy provides a natural connection between the $f(\alpha)$ spectrum and a directly observable spectrum $\tau(q)$ defined from the power-law behavior, in the limit $\epsilon \rightarrow 0^+$, of the partition function [45]:

$$Z_q(\epsilon) = \sum_i \mu\left(B_i(\epsilon)\right)^q \sim \epsilon^{\tau(q)}, \tag{7}$$

where the sum is taken over a partition of the support of the singular measure into boxes of size ϵ. The variables q and $\tau(q)$ play the same role as the inverse of temperature and the free energy in thermodynamics, while the Legendre transform

$$f(\alpha) = \min_q(q\alpha - \tau(q)) \tag{8}$$

indicates that instead of energy and entropy, we have α and $f(\alpha)$ as the thermodynamical variables conjugate to q and $\tau(q)$ [36, 45–47, 50]. Let us mention that the so-called generalized fractal dimensions D_q [49, 58] are nothing else than $D_q = \tau(q)/(q-1)$. Most of the rigourous mathematical results concerning the multifractal formalism have been obtained in the context of dynamical system theory [46, 51] and of modelling of random cascades in fully developed turbulence [53, 59, 60]. It has been developed into a powerful technique (e.g. box-counting algorithms, fixed-size and fixed-mass correlation algorithms) [49, 61–66] accessible also to experimentalists. Successful applications have been reported in various fields [8, 11, 13, 15] and the pertinence of the multifractal approach seems, nowadays, to be well admitted in the scientific community at large.

There have been several attempts to extend the concept of multifractal to *singular functions* [33, 34]. In the context of fully developed turbulence [15], the intermittent character of turbulent velocity signals was investigated by calculating the moments of the probability

density function (pdf) of (longitudinal) velocity increments $\delta v_l(x) = v(x + l) - v(x)$, over inertial separation [15, 33]:

$$S_p(l) = <|\delta v_l|^p> \sim l^{\zeta_p}. \tag{9}$$

By Legendre transforming the scaling exponents ζ_p of these *structure functions* (SF) of order p [67], one aims to estimate the Hausdorff dimension $D(h)$ of the subset of $\mathbb{R}$ where velocity increments behave as $\delta v_l \sim l^h$ [33]:

$$D(h) = \min_p(ph - \zeta_p + 1). \tag{10}$$

In a more general context, $D(h)$ can be defined as the spectrum of Hölder exponents for the singular signal under study, in full analogy with the $f(\alpha)$ singularity spectrum (8) for singular measures. However, as discussed in the next section, there are some fundamental limitations to the structure function approach which intrinsically fails to fully characterize the $D(h)$ singularity spectrum [68].

Our purpose here, is to report on an alternative strategy that we have proposed and which is likely to provide a unified thermodynamical description of multifractal distributions including measures and functions [31, 32, 35, 36, 42]. This approach relies on the use of a mathematical tool introduced in signal analysis: the *wavelet transform* [69–81]. The wavelet transform has been proved to be very efficient to detect singularities [37–42, 77–80]. In that respect, it is a well adapted technique to study fractal objects [77, 82–85]. Since a wavelet can be seen as an oscillating variant of a box (*i.e.*, a "square" function), we will show, as a first step, that one can generalize the multifractal formalism by defining new partition functions in terms of wavelet coefficients [31, 32, 35, 36, 42]. In particular, by choosing a wavelet which is orthogonal to polynomial behavior up to some order N, one can make the wavelet transform blind to regular behavior, remedying in this way for one of the main failures of the classical approaches (*e.g.*, the box-counting method in the case of measures and the struture function method in the case of functions). The other fundamental advantage of using wavelets is that the skeleton defined by the *wavelet transform modulus maxima* [40, 41] provides an adaptative space-scale partition of the fractal distribution under study, from which one can extract the $D(h)$ singularity spectrum [31, 32, 35, 36, 42]. As a second step, we will demonstrate that one can go even deeper in the multifractal analysis by studying correlation functions in both space and scales [86, 87]. Actually, in the arborescent structure of the wavelet transform skeleton, is somehow uncoded the multiplicative cascade process that underlies the multifractal properties of the considered function. To illustrate our purpose, we will report on the most significant results obtained when applying our concepts and methodology to three different experimental situations, namely the statistical analysis of DNA sequences, of high resolution satellite images of the cloud structure and of stock market data.

2   The wavelet transform modulus maxima method for the multifractal analysis of 1D signals

The continuous wavelet transform (WT) is a mathematical technique introduced in signal analysis in the early eighties [88–90]. Since then, it has been the subject of considerable theoretical developments and practical applications in a wide variety of fields [69–81]. The WT has been early recognized as a mathematical microscope that is well adapted to reveal the hierarchy that governs the spatial distribution of the singularities of multifractal measures [83–85]. What makes the WT of fundamental use in the present study is that its singularity scanning ability equally applies to singular functions than to singular measures [31, 32, 35–42, 77–80, 82].

2.1   The continuous wavelet transform

The WT is a space-scale analysis which consists in expanding signals in terms of *wavelets* which are constructed from a single function, the *analyzing wavelet* ψ, by means of translations and dilations. The WT of a real-valued function f is defined as [88–90]:

$$T_\psi[f](x_0, a) = \frac{1}{a} \int_{-\infty}^{+\infty} f(x)\psi(\frac{x - x_0}{a})dx \ , \tag{11}$$

where x_0 is the space parameter and a (> 0) the scale parameter. The analyzing wavelet ψ is generally chosen to be well localized in both space and frequency. Usually ψ is required to be of zero mean for the WT to be invertible. But for the particular purpose of singularity tracking that is of interest here, we will further require ψ to be orthogonal to low-order polynomials [31, 32, 35–42]:

$$\int_{-\infty}^{+\infty} x^m \psi(x)dx \ , \quad \forall m \ , \quad 0 \le m < n_\psi \ . \tag{12}$$

As originally pointed out by Mallat and collaborators [40, 41], for the specific purpose of analyzing the regularity of a function, one can get rid of the redundancy of the WT by concentrating on the WT skeleton defined by its modulus maxima only. These maxima are defined, at each scale a, as the local maxima of $|T_\psi[f](x, a)|$ considered as a function of x (Fig. 1c). As illustrated in Fig. 1d, these WTMM are disposed on connected curves in the space-scale (or time-scale) half-plane, called *maxima lines*. Let us define $\mathcal{L}(a_0)$ as the set of all the maxima lines that exist at the scale a_0 and which contain maxima at any scale $a \le a_0$. An important feature of these maxima lines, when analyzing singular functions, is that there is at least one maxima line pointing towards each singularity (Fig. 1d) [32, 40–42] .

2.2   Scanning singularities with the wavelet transform modulus maxima

As introduced in section 1, the strength of a singularity of a function is quantified by the *Hölder exponent* (6). This definition of the singularity strength naturally leads to a
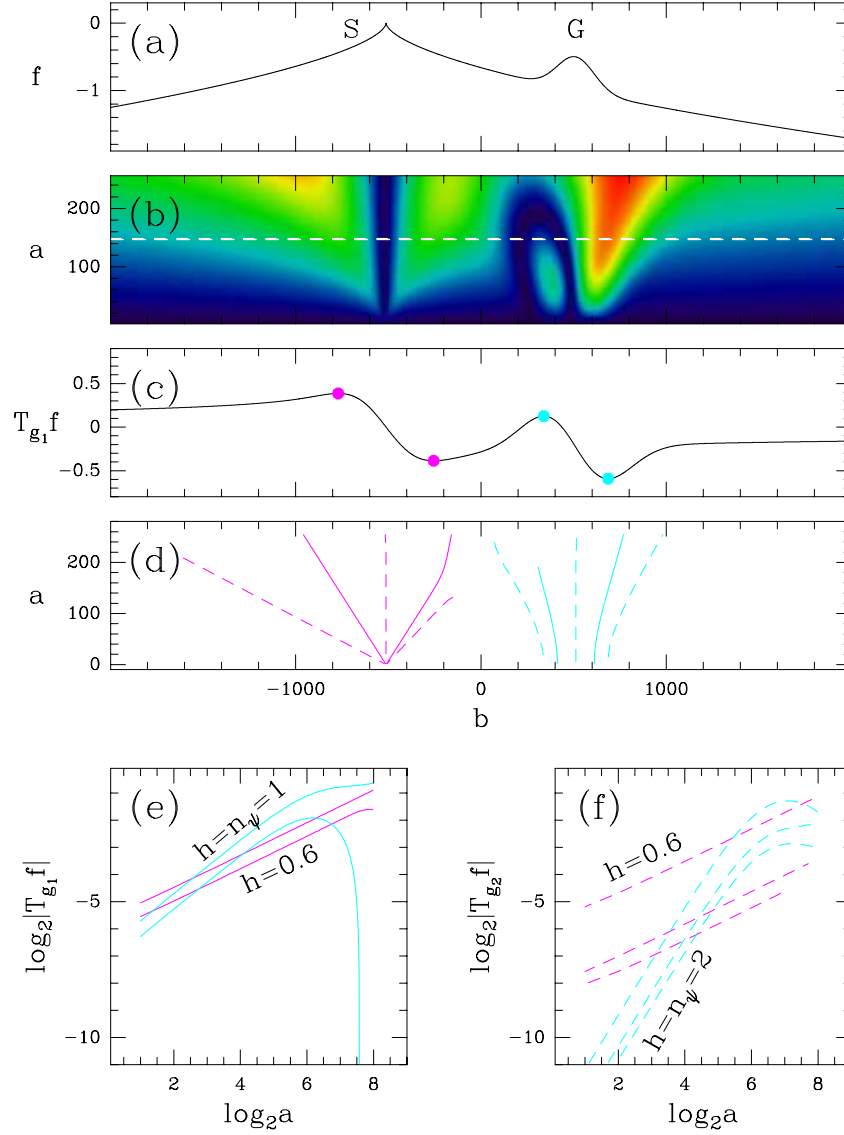
Fig. 1. How to estimate the Hölder exponent from the behavior of the WT modulus along the maxima lines. (a) Graph of the function $f(x) = -|\frac{x-x_0}{1024}|^{0.6} + \frac{1}{2}\exp(-\frac{1}{2}(\frac{x-x_1}{100})^2)$, which displays a singularity S of Hölder exponent $h = 0.6$ located at $x_0 = -512$ and a smooth localized behavior G at $x_1 = 512$. (b) The WT of f(x) computed using the first-order derivative of the Gaussian function $g^{(1)}$ (20) as coded according to the natural order of the light spectrum from black ($|T_\psi| = 0$) to red ($\max_{b,a}|T_\psi|$). (c) Horizontal section of $T_\psi[f](b,a)$ at the scale $a = a_0$; the symbols (•) represent the modulus maxima. (d) Maxima lines of the WT in the (b,a) half-plane as computed when using the first-order (——) or the second-order (– – –) derivative of the gaussian function. (e) Local measurement of the scaling exponent along the maxima lines when using $g^{(1)}$ ($n_\psi = 1$): $h(x_0) = 0.6$, $h(x_1) = n_\psi = 1$; the slope of the curve $\log_2|T_\psi f|$ vs $\log_2 a$ provides an estimate of the scaling exponent. (f) Same computation as in (e) but when using a second-order analyzing wavelet $g^{(2)}$ ($n_\psi = 2$): $h(x_0) = 0.6$, $h(x_1) = n_\psi = 2$. The results in (e) and in (f) are therefore in good agreement with the theoritical predictions given by (14) and (15). Let us remark that the number of maxima lines that point to a given singularity is $n_\psi + 1$.

generalization of the so-called $f(\alpha)$ singularity spectrum (8) introduced for fractal measures in Refs. [45, 46, 51]. As originally defined by Parisi and Frisch [33], we will denote $D(h)$ the Hausdorff dimension of the set where the Hölder exponent is equal to h [31, 32, 36]:

$$D(h) = dim_H\{x \ , \ h(x) = h\} \ , \tag{13}$$

where h can take, *a priori*, positive as well as negative real values (*e.g.*, the Dirac distribution $\delta(x)$ corresponds to the Hölder exponent $h(0) = -1$).

The main interest in using the WT for analyzing the regularity of a function lies in its ability to be blind to polynomial behavior by an appropriate choice of the analyzing wavelet ψ. Indeed, let us assume that according to (6), f has, at the point x_0, a local scaling (Hölder) exponent $h(x_0)$; then, assuming that the singularity is not oscillating [40, 91, 92], one can easily prove that the local behavior of f is mirrored by the WT which locally behaves like [37, 39–42, 82, 93] :

$$T_\psi[f](x_0, a) \sim a^{h(x_0)} \ , a \to 0^+ \ , \tag{14}$$

provided $n_\psi > h(x_0)$, where n_ψ is the number of vanishing moments of ψ (12). Therefore one can extract the exponent $h(x_0)$ as the slope of a log-log plot of the WT amplitude versus the scale a. On the contrary, if one chooses $n_\psi < h(x_0)$, the WT still behaves as a power-law but with a scaling exponent which is n_ψ :

$$T_\psi[f](x_0, a) \sim a^{n_\psi} \ , a \to 0^+ \ . \tag{15}$$

Thus, around a given point x_0, the faster the WT decreases when the scale goes to zero, the more regular f is around that point. In particular, if $f \in C^\infty$ at x_0 ($h(x_0) = +\infty$), then the WT scaling exponent is given by n_ψ, *i.e.* a value which is dependent on the shape of the analyzing wavelet. According to this observation, one can hope to detect the points where f is smooth by just checking the scaling behavior of the WT when increasing the order n_ψ of the analyzing wavelet [32, 35, 36, 42]. Let us also remark that if $h(x_0)$ is negative, then the WT no longer decreases but instead increases when the scale a goes to zero; this remark has been of fundamental use in Ref. [94] for detecting vorticity filaments in turbulent pressure signals.

A very important point (at least for practical purpose) raised by Mallat and Hwang [41] is that the local scaling exponent $h(x_0)$ can be equally estimated by looking at the value of the WT modulus along a maxima line converging towards the point x_0. Indeed one can prove that both (14) and (15) still hold when following a maxima line from large down to small scales [41, 42]. This is illustrated in Fig. 1 for the particular case of an isolated singularity "interacting" with a localized smooth structure. The situation is somewhat more intricate when investigating fractal functions. Indeed the characteristic feature of these singular functions is the existence of a hierarchical distribution of singularities [31, 32, 35, 36, 42, 82]. Locally, the Hölder exponent $h(x_0)$ is governed by the singularities which accumulate at x_0. This results in unavoidable oscillations around the expected power-law behavior of the WT amplitude [31, 32, 36, 42, 95]. Therefore the exact determination of h

from log-log plots on a finite range of scales is somewhat uncertain [96–98]. Of course, there have been many attempts to circumvent these difficulties [31, 97]. Nevertheless there exist fundamental limitations (which are not intrinsic to the WT technique) to the estimate of Hölder exponents of fractal functions. Consequently, the determination of statistical quantities like the $D(h)$ singularity spectrum, requires a method which is more feasible and more appropriate than a systematic investigation of the local scaling behavior of the WT. This is the purpose of the recently developed waveled-based multifractal formalism [32, 35, 36, 42] that we will explicitly use in section 3 to analyze the statistical scaling properties of DNA walks.

2.3   A wavelet-based multifractal formalism : the wavelet transform modulus maxima method

A natural way of performing a multifractal analysis of fractal functions consists in generalizing the "classical" multifractal formalism [43–51] using wavelets instead of boxes. By taking advantage of the freedom in the choice of the "generalized oscillating boxes" that are the wavelets, one can hope to get rid of possible smooth behavior that could mask singularities or perturb the estimation of their strength h. But the major difficulty with respect to box-counting techniques [49, 61, 62, 64, 65] for singular measures, consists in defining a covering of the support of the singular part of the function with our set of wavelets of different sizes. A simple method would rely on the definition of the following *partition function* in terms of WT coefficients [82] :

$$Z(q,a) = \int |T_\psi[f](x,a)|^q dx ,\tag{16}$$

where $q \in \mathbb{R}$. This method based on a continuous covering of the real line would be however unstable for negative q values since nothing prevents the WT coefficients from vanishing at some point (x_0, a) of the space-scale half-plane.

   The wavelet transform modulus maxima (WTMM) [32, 35, 36, 42] method implies that one changes the continuous sum over space in (16) into a discrete sum over the local maxima of $|T_\psi[f](x,a)|$:

$$Z(q,a) = \sum_{l \in \mathcal{L}(a)} \left(\sup_{\substack{(x,a') \in l \\ a' \leq a}} |T_\psi[f](x,a')| \right)^q .\tag{17}$$

As emphasized in Refs. [32, 35, 36, 42], the branching structure of the WT skeleton in the (x, a) half-plane enlightens the hierarchical organization of the singularities (see Figs 3e and 3f). Thus the WT skeleton indicates how to position, at the considered scale a, the oscillating boxes in order to obtain a partition of the singularities of f. The sup in (17) can be regarded as a way to define a scale adaptive "Hausdorff-like" partition. Now from the deep analogy that links the multifractal formalism to thermodynamics [36, 47, 50], one

can define the exponent $\tau(q)$ from the power-law behavior of the partition function :

$$Z(q, a) \sim a^{\tau(q)} , \quad a \to 0^+ , \tag{18}$$

where q and $\tau(q)$ again play respectively the role of the inverse temperature and the free energy. The main result of this wavelet-based multifractal formalism is that in place of the energy and the entropy (*i.e.* the variables conjugated to q and τ), one has h, the Hölder exponent, and $D(h)$, the singularity spectrum. This means that the singularity spectrum of f can be determined from the Legendre transform of the partition function scaling exponent $\tau(q)$ [42, 99]:

$$D(h) = \min_q(qh - \tau(q)) . \tag{19}$$

From the properties of the Legendre transform, it is easy to see that *homogeneous* fractal functions that involve singularities of unique Hölder exponent $h = \partial\tau/\partial q$, are characterized by a $\tau(q)$ spectrum which is a *linear* function of q. On the contrary, a *nonlinear* $\tau(q)$ curve is the signature of nonhomogeneous functions that exhibit *multifractal* properties, in the sense that the Hölder exponent $h(x)$ is a fluctuating quantity that depends upon the spatial position x.

Remark 1: The partition function exponents $\tau(q)$ are much more than simply some intermediate quantities of a rather easy experimental access. For some specific values of q, they have well known meaning [31, 32]. In full analogy with standard box-counting arguments, $-\tau(0)$ can be identified to the capacity of the set of singularities of f: $-\tau(0) = d_C(\{x, h(x) < +\infty\})$. Similarly, $\tau(1)$ is related to the capacity of the graph $\mathcal{G}$ of the considered function: $d_C(\mathcal{G}) = \max(1, 1 - \tau(1))$. Finally $\tau(2)$ is related to the scaling exponent β of the spectral density $S(k) = |\hat{f}(k)|^2 \sim k^{-\beta}$ with $\beta = 2 + \tau(2)$.

Remark 2: Since the WTMM method is mainly devoted to practical applications to stochastic systems, let us point out that the theoretical treatment of *random multifractal functions* requires special attention. A priori, there is no reason that all the realizations of the same stochastic multifractal process correspond to a unique $D(h)$-curve. Each realization has its own unique distribution of singularities and one crucial issue is to relate these distributions to some averaged versions computed experimentally. As emphasized by Hentschel [100], one can take advantage of the analogy that links the multifractal description to statistical thermodynamics [36, 45–47, 50], by using methods created specifically to study disorder in spin-glass theory [101]. When carrying out replica averages of the random partition function associated with a stochastic function, one gets multifractal spectra $\tau(q, n)$ that generally depend on the number n of members in the replica average (let us

note that $n = 0$ and $n = 1$ respectively correspond to commonly used *quenched* and *annealed* averaging [100]. Then, by Legendre transforming $\tau(q, n)$, some type of average $D(h)$ spectra are being found [100]. Some care is thus required when interpreting these average spectra in order to avoid some misunderstanding of the underlying physics. We refer the reader to Refs. [42, 99] for rigorous mathematical results concerning the application of the WTMM method to stochastic functions.

2.4   Defining our battery of analyzing wavelets

There are almost as many analyzing wavelets as applications of the continuous WT. In our original works [32, 36, 77, 83–85], we have mainly used the class of analyzing wavelets defined by the successive derivatives of the Gaussian function:

$$g^{(N)}(x) = \frac{d^N}{dx^N} e^{-x^2/2} \; , \tag{20}$$

for which $n_\psi = N$. Throughout this study, we will rather use the set of compactly supported analyzing wavelets $\psi_{(m)}^{(n)}$ plotted in Fig. 2 [94, 102, 103]. They are constructed from Dirac distributions $(\psi_{(0)}^{(n)})$ via successive convolutions with the box function χ. The index m_ψ, corresponding to the number of convolutions, characterizes the smoothness of the analyzing wavelet. n_ψ is by definition the number of vanishing moments of ψ.

Let us note that the functions $\psi_{(m)}^{(0)}$ are not analyzing wavelets since there are not of zero mean. However, when using $\psi_{(1)}^{(0)}$ (which is nothing else than the box function χ) into the (continuous) partition function defined in (16), one recovers some variant of classical box-counting techniques [49, 61, 62, 64, 65] commonly used for multifractal analysis of singular measures. Let us also remark that when using $\psi_{(0)}^{(1)}(x) = \delta(x-1) - \delta(x)$, the WT is nothing but the local increment of the considered function and the (continuous) partition function (16) then reduces to the so-called structure function of order q (9) [15, 33, 67] . We refer the reader to Ref. [68] where a comparative study of the structure function approach and the WTMM method is carried out. The main messages of this study are reported in the next section.

2.5   The structure function approach versus the WTMM method

It is tempting to relate the exponents $\tau(q)$, defined from the WT partition functions (17,18), to the scaling exponents ζ_p of the structure functions (9). A simple comparison of (10) and (19) gives immediately [31, 32]:
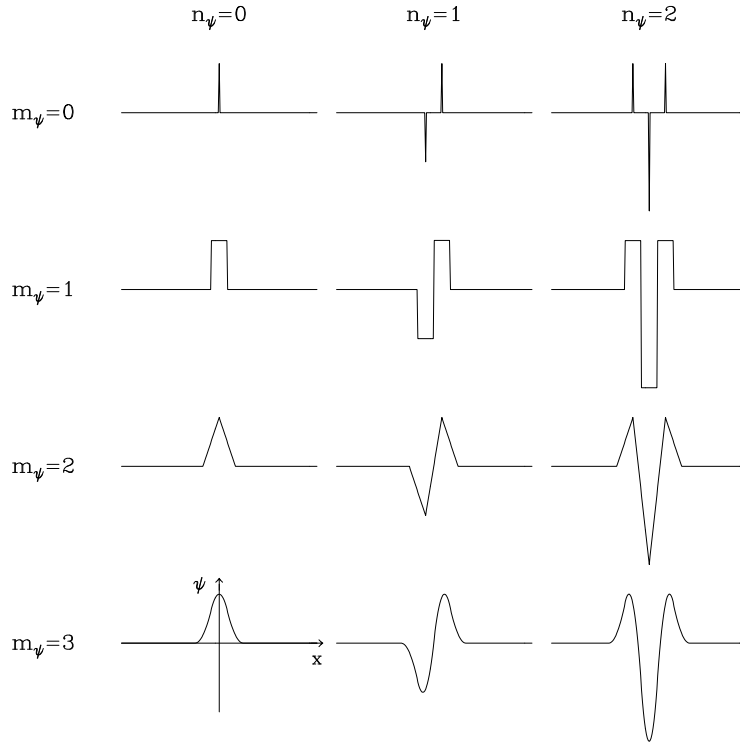
$$\tau(q) = \zeta_q - 1. \tag{21}$$

Fig. 2. Set of compactly supported analyzing wavelets $\psi_{(m)}^{(n)}$. n_ψ corresponds to the number of vanishing moments. The functions $\psi_{(m)}^{(n)}$ are smooth versions of $\psi_{(0)}^{(n)}$ obtained after m successive convolutions with the box function χ.

But this relationship does not hold for all values of q; this results from intrinsic limitations of the SF approach [68]. As pointed out just above [31, 32, 97], the local increment of a function can be seen as its WT computed at point x_0 and scale l, with the "poor man's wavelet" $\Delta(x) = \psi_{(0)}^{(1)}(x) = \delta(x-1) - \delta(x)$. In this spirit, the SF's (9) are analogous to the naive partition functions defined in (16):

$$S_q(l) = \int |\delta f_l(x)|^q dx. \tag{22}$$

However, there are two main differences between the WTMM partition functions (17) and the SF's (22) from which result the insufficiencies of the SF method [68].

(i) *The continuous integral used to define $S_q(l)$*. Indeed, there is no reason, *a priori*, that the increment pdf vanishes around $\delta f_l = 0$. Thus the SF $S_q(l)$ may diverge for $q \leq -1$. Consequently, the ζ_q spectrum estimate is unstable for $q < 0$ and from the Legendre transform properties, only the (increasing) part of the $D(h)$ singularity spectrum (*e.g.*, the left part of the $D(h)$ curve in Fig. 4) corresponding to the strongest singularities is amenable to the SF approach. The first crucial advantage of the WTMM method is that the partition function (17) is computed using a discrete summation over the WT skeleton where the WT coefficients do not vanish (by definition of the WTMM); this keeps the calculation of $Z(q, a)$ stable for $q < 0$.

(ii) *The poorness of the analyzing wavelet* $\Delta(x)$. The second main disadvantage of the SF method is that the "poor's man wavelet" $\Delta(x)$ [31, 32, 97] does not satisfy the criteria to be an efficient analyzing wavelet. First $\Delta(x)$ is only orthogonal to constants but not to higher order polynomials ($n_\psi = 1$). This precludes the detection of singularities with $h \geq 1$. Thus, as demonstrated in Ref. [68], if the maximum value of $D(h)$ is reached for some $h \geq 1$, the accessible range of singularities is even more truncated to values $h < h_{\mathrm{crit}} < 1$. Moreover, $\Delta(x)$ is a singular analyzing wavelet made of two Dirac distributions and therefore it cannot generally be integrated against tempered distributions. When using (22) to study some distribution which involves singularities with $h \leq 0$, one is generally faced to severe instabilities in the computation of the SF's. Therefore, the range of Hölder exponents accessible to the SF method is not only limited from above ($h < h_{\mathrm{crit}} \leq 1$), but also from below ($h > 0$). Because one has the freedom to select an analyzing wavelet ψ which is smooth and which has enough vanishing moments ($n_\psi > h_{\max}$), the WTMM method does not possess any of these drawbacks [68] . This is why the WTMM method is much more than a simple generalization of commonly used box-counting and structure functions techniques [31, 32, 35, 36, 42, 77].

2.6   Discriminating multifractal from monofractal synthetic random 1D signals

This section is devoted to test applications of the WTMM method to random functions generated either by *additive* models like fractional Brownian motions [21, 22] or by *multiplicative* models like random $\mathcal{W}$-cascades on wavelet dyadic trees [102–106]. For each model, we first wavelet transform 1000 realizations of length $L = 65536$ with a first order ($n_\psi = 1$) analyzing wavelet. From the WT skeletons defined by the WTMM, we compute the mean partition function (17) from which we extract the annealed $\tau(q)$ (18) and, in turn, $D(h)$ (19) multifractal spectra. We systematically test the robustness of our estimates with respect to some change of the shape of the analyzing wavelet, in particular when increasing the number n_ψ of zero moments.

Fractional Brownian signals

Since its introduction by Mandelbrot and Van Ness [21], the fractional Brownian motion (fBm) has become a very popular model in signal and image processing [1–22, 27]. In 1D, fBm has proved useful for modeling various physical phenomena with long-range dependence, e.g., "$1/f$" noises. The fBm exhibits a power spectral density $S(k) \sim 1/k^\beta$, where the spectral exponent $\beta = 2H + 1$ is related to the Hurst exponent H. fBm has been extensively used as test stochastic signals for Hurst exponent measurements. The performances of classical methods (e.g., height-height correlation function, variance and power spectral methods, first return and multireturn probability distributions, maximum likelihood techniques) [29, 30, 107–114] have been recently competed by wavelet-based techniques [115–125] . A fBm $B_H(x)$ indexed by $H \in]0, 1[$, is a Gaussian process of mean value

0 and whose correlation function is given by

$$< B_H(x)B_H(y) >= \frac{\sigma^2}{2}\left(|x|^{2H} + |y|^{2H} - |x - y|^{2H}\right) \ ,\tag{23}$$

where $<>$ represents the mean value. The variance of such process is

$$\mathrm{var}(B_H(x)) = \sigma^2|x|^{2H} \ .\tag{24}$$

The classical Brownian motion corresponds to $H = 1/2$ and to a variance $\mathrm{var}(B_{1/2}(x)) = \sigma^2|x|$. On can easily show that the increments of a fBm, i.e, $\delta B_{H,l} = B_H(x + l) - B_H(x)$ ($l \in \mathbb{R}^{+*}$ fixed), are stationary. Indeed, the correlation function depends only on $x - y$ and l:

$$< \delta B_{H,l}(x)\delta B_{H,l}(y) >= \frac{\sigma^2}{2}\left(|x - y + l|^{2H} + |x - y - l|^{2H} - 2|x - y|^{2H}\right) \ .\tag{25}$$

For $H = 1/2$, we recover the fact that the increments of the classical Brownian motion are independent. For any other value of H, the increments are either positively correlated ($H > 1/2$: persistent random walk) or anti-correlated ($H < 1/2$: antipersistent random walk). Moreover, from (23) one gets:

$$B_H(x + \lambda y) - B_H(x) \simeq \lambda^H \left(B_H(x + y) - B_H(x)\right) \ ,\tag{26}$$

where $\simeq$ stands for the equality in law. This means that fBm's are self-affine processes (1) and that the Hurst exponent is H. The higher H, the more regular the motion. But since (26) holds for any x and y, this means that almost all realizations of the fBm are continuous, everywhere non differentiable with a unique Hölder exponent $h(x) = H$, $\forall x$ [1, 22, 32, 126]. Thus the fBm's are homogeneous fractals characterized by a singularity spectrum which reduces to a single point:

$$D(h) = 1 \ \text{if} \ h = H \ ,\tag{27}$$
$$= -\infty \ \text{if} \ h \neq H \ .$$

By Legendre transforming $D(h)$, one gets the following expression for the partition function exponents:

$$\tau(q) = qH - 1 \ .\tag{28}$$

$\tau(q)$ is a linear function of q with a slope given by the index H of the fBm. Let us point out that $\tau(2) \neq 0$ (i.e. $H \neq 1/2$) indicates the presence of long-range correlations.

In Figs 3 and 4, we report the results of a statistical analysis of fBm's using the WTMM method [32, 35, 36, 68]. We mainly concentrate on $B_{1/3}$ since it has a $k^{-5/3}$ power-spectrum similar to the spectrum of the multifractal stochastic signal we will study in the next section. Actually, our goal is to demonstrate that, where the power spectrum analysis fails, the WTMM method succeeds in discriminating unambiguously between these two fractal signals. The numerical signals were generated by filtering uniformly generated pseudo-random

noise in Fourier space in order to have the required $k^{-5/3}$ spectral density. A $B_{1/3}$ fractional Brownian trail is shown in Fig. 3a. Fig. 3c illustrates the WT coded, independently at each scale a, using 256 colors. The analyzing wavelet is $\psi_{(3)}^{(1)}$ ($n_\psi = 1$). Fig. 4a displays some plots of $\log_2 Z(q,a)$ versus $\log_2(a)$ for different values of q, where the partition function $Z(q,a)$ has been computed on the WTMM skeleton shown in Fig. 3e, according to the definition (17). Using a linear regression fit, we then obtain the slopes $\tau(q)$ of these graphs. As shown in Fig. 4c, when plotted versus q, the data for the exponents $\tau(q)$ consistently fall on a straight line that is remarkably fitted by the theoretical prediction $\tau(q) = q/3 - 1$ (28). As expected theoretically, we find from the numerical application of the WTMM method, that the fBm $B_{1/3}$ is a nowhere differentiable homogeneous fractal signal with a unique Hölder exponent $h = H = 1/3$ as given by the slope of the linear $\tau(q)$ spectrum (the hallmark of homogeneous fractal scaling). Similar good estimates are obtained when using analyzing wavelets of different orders, and this whatever the value of the index H of the fBm.

Random $\mathcal{W}$-cascades

Multiplicative cascade models have enjoyed increasing interest in recent years as the paradigm of multifractal objects [1, 45, 48, 53, 54, 100]. The notion of cascade actually refers to a self-similar process whose properties are defined multiplicatively from coarse to fine scales. In that respect, it occupies a central place in the statistical theory of turbulence [15, 54, 67]. Since Richardson's scenario [127], the turbulent cascade picture has been often invoked to account for the intermittency phenomenon observed in fully developed turbulent flows [15, 53, 54, 67]: energy is transferred from large eddies down to small scales (where it is dissipated) through a cascade process in which the transfer rate at a given scale is not spatially homogeneous, as supposed in the theory developed by Kolmogorov in 1941 [128], but undergoes local intermittent fluctuations [15, 53, 54, 67]. Over the past fourty years, refined models including the log-normal model of Kolmogorov [129] and Obukhov [130], multiplicative hierarchical cascade models like the random β-model [43], the α-model [131], the p-model [132] (for a review, see Ref. [54]), the log-stable models [133–135] and more recently the log-infinitely divisible cascade models [136–140], have grown in the literature as reasonable models to mimic the energy cascading process in turbulent flows. On a very general ground, a self-similar cascade is defined by the way the scales are refined and by the statistics of the multiplicative factors at each step of the process [53, 54, 100, 135]. One can thus distinguish discrete cascades that involve discrete scale ratios leading to log-periodic corrections to scaling (*discrete scale invariance* [32, 84, 85, 95]), from continuous cascades without preferable scale factors (*continuous scale invariance*). More fundamentally, there are two main classes of self-similar cascade processes : *deterministic cascades* that generally correspond to solvable models and *random cascades* that are likely to provide more realistic models but for which some theoretical care is required as far as their multifractal limit and some basic multifractal properties (including multifractal phase transitions) are concerned [100]. As a notable member of the later class, the independent random cascades
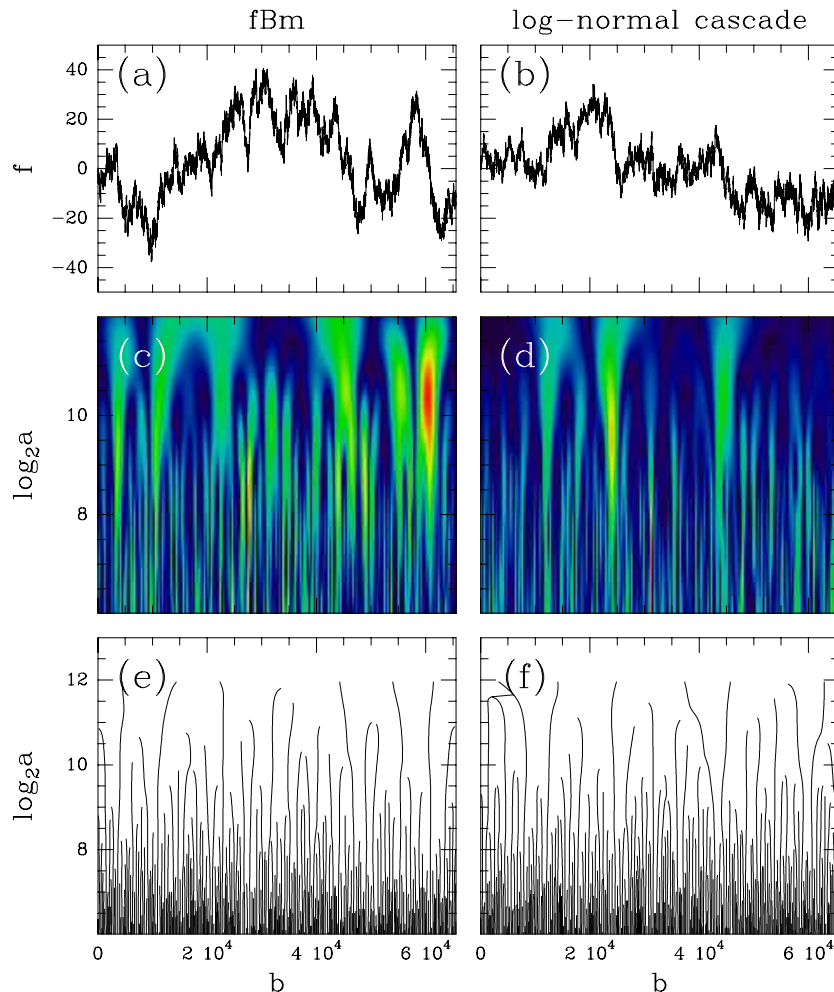
fBm   log−normal cascade

Fig. 3. WT of monofractal and multifractal stochastic signals. *Fractionnal Brownian motion:* (a) a realization of $B_{1/3}$ ($L = 65536$); (c) WT of $B_{1/3}$ as coded, independently at each scale a, using 256 colors from black ($|T_\psi| = 0$) to red ($\max_b |T_\psi|$); (e) WT skeleton defined by the set of all the maxima lines. *Log-normal random $\mathcal{W}$-cascades:* (b) a realization of the log-normal $\mathcal{W}$-cascade model ($L = 65536$) with the following parameter values $m = -0.355 \ln 2$ and $\sigma^2 = 0.02 \ln 2$ (see Refs. [103–105]); (d) WT of the realization in (b) represented with the same color coding as in (c); (f) WT skeleton. The analyzing wavelet is $\psi_{(3)}^{(1)}$ (see Fig. 2).

introduced by Mandelbrot (commonly called $\mathcal{M}$-*cascades* [53, 141, 142]) as a general model of random curdling in fully developed turbulence, have a special status since they are the main cascade model for which deep mathematical results have been obtained [59, 60]. Moreover, as pointed out by Schertzer and Lovejoy [143], this "first generation" of cascade models is *static* in the sense that it accounts for the multiplicative hierarchical structure of the data in the spatial domain only [135]. With the specific goal to model temporal evolution, these authors have proposed a "second generation" of space-time cascade models that take into account both the scaling anisotropy between space and time, and the breaking of the mirror symmetry along the temporal axis, *i.e.*, causality [135, 143, 144].
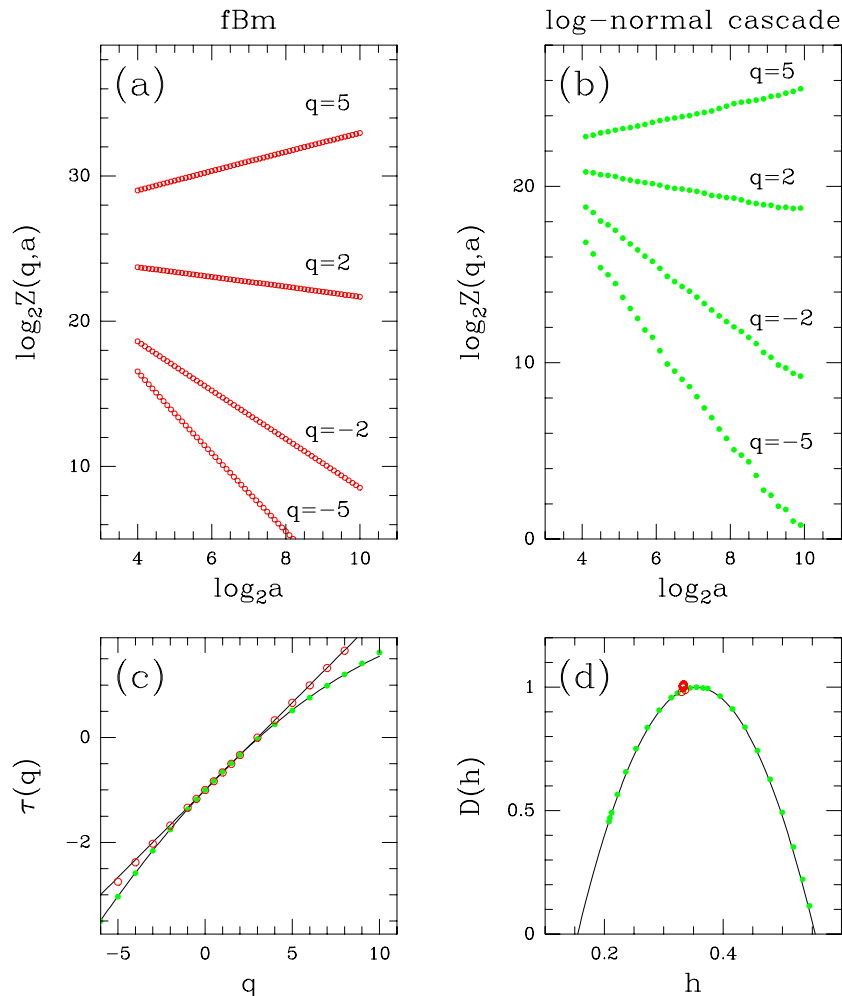
Fig. 4. Determination of the $\tau(q)$ **and** $D(h)$ **multifractal spectra** of fBm $B_{1/3}$ (red circles) and log-normal random $\mathcal{W}$-cascades (green dots) using the WTMM method. (a) $\log_2 Z(q,a)$ vs $\log_2 a$: $B_{1/3}$. (b) $\log_2 Z(q,a)$ vs $\log_2 a$: log-normal $\mathcal{W}$-cascades with the same parameters as in Fig. 3b. (c) $\tau(q)$ vs q; the solid lines correspond respectively to the theoretical spectra (28) and (29). (d) $D(h)$ vs h; the solid lines correspond respectively to the theoretical predictions (27) and (30). The analyzing wavelet is $\psi_{(3)}^{(1)}$. The reported results correspond to annealed averaging over 1000 realizations of $L = 65536$.

Paradoxically, if there is a plethora of mono and multifractal cascade models in the literature that generate deterministic as well as random singular measures in the small-scale limit, there are still only a handful of distinct algorithms for synthesizing "rough" functions of a single variable with multifractal statistics. Beyond the problem of the multifractal description of singular functions that has been solved with the WTMM method [32, 35, 36, 42], there is thus the practical issue of defining in any concrete way how to build a multifractal function. Schertzer and Lovejoy [133] suggested a simple power-law filtering (fractional integration) of singular cascade measures. So, this model combines a multiplicative procedure with an additive one reminiscent of some algorithms to generate fBm [1, 27, 30]. In Refs. [34, 145], the midpoint displacement technique for building fBm was generalized

to generate deterministic or random multi-affine functions. The same goal was achieved in Refs. [32, 42] by combining fractional or ordinary integration with signed measures obtained by recursive cascade like procedures. Several other attempts to simulate "synthetic turbulence" that shares the intermittency properties of turbulent velocity data have partially succeeded [146–149]. More recently, the concept of self-similar cascades leading to multifractal measures has been generalized to the construction of scale-invariant signals using orthonormal wavelet basis [102–106]. Instead of redistributing the measure over subintervals with multiplicative weights, one allocates the wavelet coefficients in a multiplicative way on the dyadic grid. This method has been implemented to generate multifractal functions from a given deterministic or probalistic multiplicative process (see section 6.2). From a mathematical point of view, the convergence of these $\mathcal{W}$-*cascades* and the regularity properties of the so-obtained deterministic or stochastic functions have been discussed in Ref. [105].

As inspired from the modelling of fully developed turbulent signals by log-infinitely divisible multiplicative processes [136–140], we will mainly concentrate here on the log-normal $\mathcal{W}$-cascades in order to calibrate the WTMM method. If m and σ^2 are respectively the mean and the variance of $\ln W$ (where W is a multiplicative random variable with log-normal probability distribution), then, as shown in Refs. [103–105], a straitghtforward computation leads to the following $\tau(q)$ spectrum:

$$\tau(q) = -\log_2 <W^q> -1 \ , \ \forall \ q \ \in \mathbb{R} \tag{29}$$
$$= -\frac{\sigma^2}{2\ln 2}q^2 - \frac{m}{\ln 2}q - 1 \ ,$$

where $< ... >$ means ensemble average. The corresponding $D(h)$ singularity spectrum is obtained by Legendre transforming $\tau(q)$ (29):

$$D(h) = -\frac{(h + m/\ln 2)^2}{2\sigma^2/\ln 2} + 1 \ . \tag{30}$$

According to the convergence criteria established in Ref. [105] , m and σ^2 have to satisfy the conditions:

$$m < 0 \ \text{ and } \ \frac{|m|}{\sigma} > \sqrt{2\ln 2}. \tag{31}$$

Moreover, by solving $D(h) = 0$, one gets the following bounds for the support of the $D(h)$ singularity spectrum:

$$h_{\min} = -\frac{m}{\ln 2} - \frac{\sqrt{2}\sigma}{\sqrt{\ln 2}} \ , \ h_{\max} = -\frac{m}{\ln 2} + \frac{\sqrt{2}\sigma}{\sqrt{\ln 2}} \ . \tag{32}$$

In Fig. 3b is illustrated a realization of a log-normal $\mathcal{W}$-cascade for the parameter values $m = -0.355 \ln 2$ and $\sigma^2 = 0.02 \ln 2$. The corresponding WT and WT skeleton as computed with $\psi_{(3)}^{(1)}$ are shown in Figs 3d and 3f respectively. The results of the application of the

WTMM method are reported in Fig. 4. As shown in Fig. 4b, when plotted versus the scale parameter a in a logarithmic representation, the annealed average of the partition functions $Z(q, a)$ displays a well defined scaling behavior over a range of scales of about 5 octaves. Let us point out that scaling of quite good quality is found for a rather wide range of q values : $-5 \leq q \leq 10$. When processing to a linear regression fit of the data over the first four octaves, one gets the $\tau(q)$ spectrum shown in Fig. 4c. This spectrum is clearly a nonlinear function of q, the hallmark of multifractal scaling. Moreover, the numerical data are in remarkable agreement with the theoretical quadratic prediction (29). Similar quantitative agreement is observed on the $D(h)$ singularity spectrum in Fig. 4d which displays a single humped parabola shape that characterizes intermittent fluctuations corresponding to Hölder exponents values ranging from $h_{\min} = 0.155$ to $h_{\max} = 0.555$ (32). Unfortunately, to capture the strongest and the weakest singularities, one needs to compute the $\tau(q)$ spectrum for very large values of $|q|$. This requires the processing of many more realizations of the considered log-normal random $\mathcal{W}$-cascade.

The test applications reported in this section demonstrate the ability of the WTMM method to resolve multifractal scaling of 1D signals, a hopeless task for classical power spectrum analysis. They were used on purpose to calibrate and to test the reliability of our methodology and of the corresponding numerical tools with respect to finite-size effects and statistical convergence.

3   Wavelet based fractal analysis of DNA sequences

Applications of the WTMM method to 1D signals have already provided insight into a wide variety of outstanding problems [77] such as fully developed turbulence [32, 35, 36, 94, 102–104, 150], finance [151, 152], medical time series analysis [153], fractal growth phenomena [154–157]. In this section, we report a recent developments in the context of statistical analysis of the complexity of DNA sequences [158–162].

The possible relevance of scale invariance and fractal concepts to the structural complexity of genomic sequences is the subject of considerable increasing interest [25, 26, 163]. During the past few years, there has been intense discussion about the existence, the nature and the origin of *long-range correlations* in DNA sequences. Different techniques including mutual information functions [164, 165], autocorrelation functions [166–168], power spectra [24, 163, 165, 169–171], *DNA walk* representation [24, 25, 172–177], Zipf analysis [178–181] were used for statistical analysis of DNA sequences. But despite the effort spent, there is still some continuing debate on rather struggling questions. In that respect, it is of fundamental importance to corroborate the fact that the reported long-range correlations are not just an artefact of the compositional heterogeneity of the genome organization [166–168, 171, 172, 175–177]. Furthermore, it is still an open question whether the long-range correlation properties are different for *protein-coding* (exonic) and *noncoding* (intronic, intergenetic) sequences [24, 25, 163–170, 173, 174, 176, 178–182]. One of the main obstacles to long-range correlation analysis is the *mosaic structure* of DNA sequences which are well known to be formed of "patches" ("strand bias") of different underlying compositions [24, 25, 172]. These patches appear as trends in the DNA walk landscapes and are likely

to introduce some breaking of scale invariance [24, 25, 171, 172, 175, 176]. Most of the techniques used so far for characterizing the presence of long-range correlations are not well adapted to study patchy sequences. In a preliminary work [158, 159], we have emphasized the WT as a very powerful technique for fractal analysis of DNA sequences. By considering analyzing wavelets that make the WT microscope blind to low-frequency trends, one can reveal and quantify the scaling properties of DNA walks. Here we report on recent results obtained by applying the WTMM method to various genomic sequences selected in the human genome as well as in other genomes of the three kingdoms [158–162].

3.1   How to make the WT microscope blind to compositional patchiness ?

A DNA sequence is a four-letter (A,C,G,T) text where A, C, G and T are the bases adenine, cytosine, guanine and thymine respectively. A popular method to graphically portray the genetic information stored in DNA sequences consists in mapping them in some variants of a n-dimensional random walk [183–185]. In this work, we will follow the strategy originally proposed by Peng *et al.* [24]. The so-called "DNA walk" analysis requires first to convert the DNA text into a binary sequence. This can be done, for example, on the basis of purine (Pu = A,G) versus Pyrimidine (Py = C,T) distinction, by defining an incremental variable that associates to position i the value $\chi(i) = 1$ or -1, depending on wheter the ith nucleotide of the sequence is Pu or Py. Each DNA sequence is thus represented as a string of purines and pyrimidines. Then the graph of the DNA walk is defined by the cumulative variables:

$$f(n) = \sum_{i=1}^{n} \chi(i) \ . \tag{33}$$

As an illustration, we show in Fig. 5a the graph of the DNA walk for the sequence of the bacteriophage λ. The patchiness of this coding sequence is patent; one clearly recognizes four regions of different strand bias, while the fluctuations about these main trends are hardly perceptible to eyes at the scale of the entire sequence. Actually, if one proceeds to some enlargements of this picture, one notices that the fluctuations involved are quite complex and possess some scale-invariant properties. The mosaic character of DNA consisting of patches of different composition (purine-rich regions, as compared to the average concentration over the entire strand, alternate with pyrimidine-rich regions corresponding to different trends in the DNA landscape shown in Fig. 5a) is generic of coding sequences. Nonconding sequences also display some patchiness which seems generally less obvious to distinguish from the bare fluctuations as already noticed in previous works [24, 25, 111, 172, 186]. This mosaic structure is recovered whatever the coding rule one uses. We refer the reader to Ref. [159] for the use of alternative base pair codings. In the present study, we will also consider a representation inspired by the binary coding proposed by Voss [169, 170] and which consists in decomposing the nucleotide sequence into 4 sequences corresponding to A, C, T or G, coding with $\chi(i) = 1$ at the nucleotide position
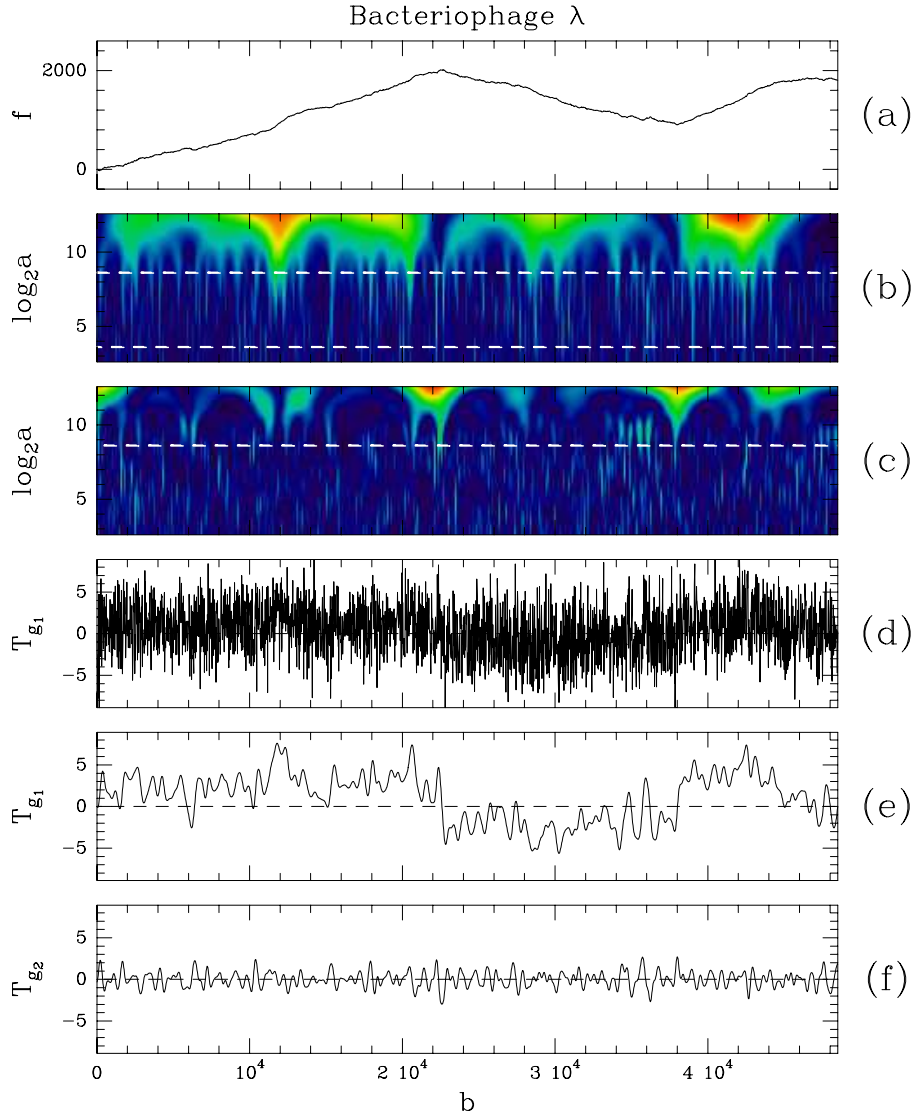
Fig. 5. WT analysis of the bacteriophage λ genome ($L = 48502$). (a) DNA walk displacement $f(x)$ based on purine-pyrimidine distinction, vs nucleotide distance x. (b) WT of $f(x)$ computed with $g^{(1)}$ (20); $T_{g^{(1)}}(b, a)$ is coded, independently at each scale a, using 256 colors from black ($min_b|T_{g^{(1)}}|$) to red ($max_b|T_{g^{(1)}}|$). (c) Same analysis as in (b) but with the second-order analyzing wavelet $g^{(2)}$. (d) $T_{g^{(1)}}(b, a = a_1)$ vs b for $a_1 = 12$ (nucleotides). (e) $T_{g^{(1)}}(b, a = a_2)$ vs b for $a_2 = 384$ (nucleotides). (f) Same analysis as in (e) but with $g^{(2)}$.

and $\chi(i) = -1/3$ at other positions. The DNA walk obtained with the A mononucleotide coding for the yeast chromosome I is shown in Fig. 7a for illustration [161].

Even though the patchy structure of DNA sequences probably contains biological informations of great importance, it is rather cumbersome as far as long-range correlation investigation is concerned. A lot of effort has been spent in order to master the presence of trends in DNA walks (and of course of trend changing). Several phenomenological methods have been proposed mainly by the Boston group. The "min-max" method in the pioneering

work of Peng *et al.* [24] has for major drawback that it requires the investigator to remove by hand the trends after identifying the local minima and maxima of the DNA landscape. The "detrended fluctuation analysis" [111, 186] recently used by this group looks much more reliable since it does not require, a priori, any decision of the investigator. This method consists in partitioning the entire landscape into boxes of length l and in computing the "detrended walk" as the difference between the original walk and the local trend. But as emphasized by Voss [170], some care is required when attempting to remove bias.

The wavelet analysis of the bacteriophage λ sequence is shown in Fig. 5. Figure 5b shows the WT space-scale representation of this DNA signal when using the first derivative of the gaussian function (20). When using a coding similar to the one prompted in previous studies, the WT is organized in a tree like structure from large to small scales, that looks qualitatively similar to the fractal branching observed in the WT representations of fBm's (Fig. 3c) and log-normal random signals (Fig. 3d). In Figs 5d and 5e, two horizontal cuts of $T_{g^{(1)}}(b, a)$ are shown at two different scales $a = a_1 = 2^2$ and $a_2 = 2^7$ that are represented by the dashed lines in Fig. 5b. When taking into account the characteristic size of the analyzing wavelet at the scale $a = 1$ corresponding to 3 nucleotides, these two scales correspond to looking at the fluctuations of the DNA walk over a characteristic length of the order of 12 and 384 nucleotides respectively. When focusing the WT microscope at the small scale $a = a_1$ in Fig. 5d, since $g^{(1)}$ is orthogonal to constants ($n_\psi = 1$), one filters out the low frequency component and reveals the local (high frequency) fluctuations of $f(x)$, *i.e.*, the local fluctuations in purine and pyrimidine compositions over small size (~ 12 nucleotides) domains. When increasing the WT magnification in Fig. 5e, one realizes that these fluctuations actually occur around three successive linear trends; $g^{(1)}$ not being blind to linear behavior, the WT coefficients fluctuate about non zero constant behavior that correspond to the slopes of those linear trends. Although this phenomenon is more pronounced when progressively increasing the scale parameter a towards a value that corresponds to the characteristic size (~ 15000 nucleotides) of these strand bias, it is indeed present at all scales. In Fig. 5f, at the same coarse scale $a = a_2$ as in Fig. 5e, the fluctuations of the WT coefficients are shown as computed with the order-2 analyzing wavelet $g^{(2)}$ ($n_\psi = 2$). The WT microscope now being also orthogonal to linear behavior, the WT coefficients fluctuate about zero and one does not see the influence of the strand bias anymore, and this at all scales (Fig. 5c). Furthermore, by considering successively $g^{(3)}$, $g^{(4)}$,..., one can hope not only to restore the stationarity of the increments of the DNA signal but also to eliminate more complicated nonlinear trends, that could be confused with the presence of long-range correlations in DNA sequences [158, 159].

3.2   Application of the WTMM method to human DNA sequences

Demonstration of the monofractality of DNA walks

As a first application of the WTMM method, let us focus on the statistical analysis of coding and noncoding sequences in the human genome [158–160, 162]. The results reported in Fig. 6 correspond to the study of 2184 introns of length $L \geq 800$ and of 226 exons of
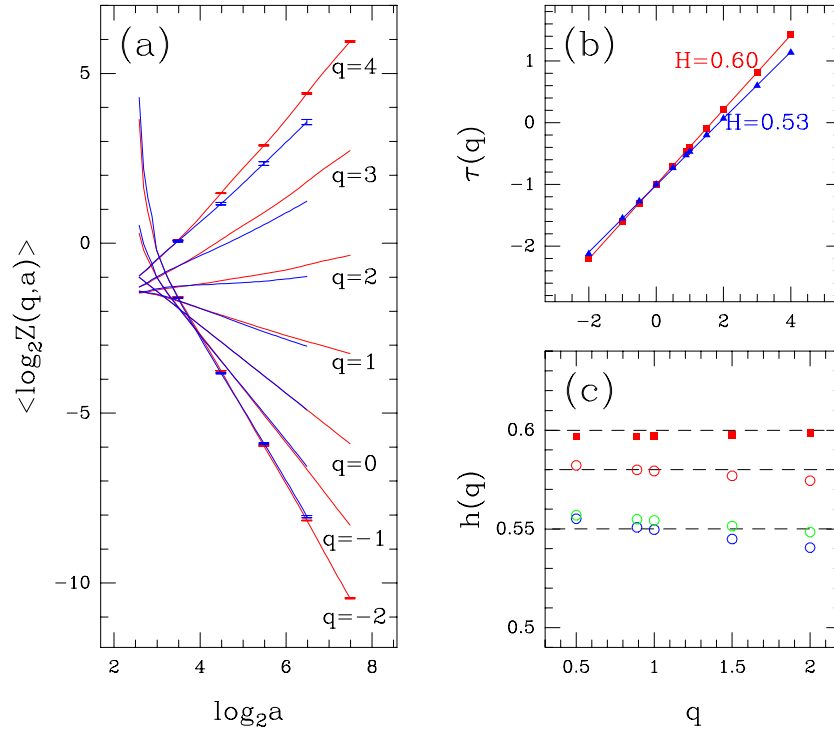
Fig. 6. Comparative WTMM analysis of the DNA walks of 2184 **introns** ($L \geq 800$) **and** 226 **exons** ($L \geq 600$) **in the human genome**. The analyzing wavelet is $g^{(2)}$. The DNA walks are generated using the G mononucleotide coding for introns (red) and exons (blue). The reported results correspond to quenched averaging over our statistical samples of introns and exons respectively. (a) $< \log_2 Z(q,a) >$ vs $\log_2 a$ for various values of q. (b) $\tau(q)$ vs q; the solid lines correspond to the theoretical spectrum $\tau(q) = qH - 1$ (28) for fBm's with $H = 0.60 \pm 0.02$ (introns) and 0.53 ± 0.02 (exons). (c) $h(q) = (\tau(q) + 1)/q$ vs q for the coding subsequences relative to position 1 (blue circles), 2 (green circles) and 3 (red circles) of the bases within the codons; the data for the introns (red squares) are shown for comparison; the horizontal broken-lines correspond to the following respective values of the Hurst exponent $H = 0.55$, 0.58 and 0.60.

length $L \geq 600$ selected in the EMBL data bank [162]. The lenght criteria used to select these sequences result from some compromise between the control of finite-size effects in the WTMM scaling analysis (those sequences are rather short sequences: $< L >_{\text{introns}} \simeq 800$, $< L >_{\text{exons}} \simeq 150$) and the achievement of statistical convergence (2184 introns and 226 exons are rich enough statistical samples). Figure 6a displays plots of the partition functions $Z(q, a)$, computed from the WT skeletons using $g^{(2)}$ as analyzing wavelet, versus the scale parameter a in a logarithmic representation. These results correspond to quenched averaging over the corresponding 2184 intron walks (red curves) and 226 exon walks (blue curves) generated using the G mononucleotide coding. For a rather wide range of q values: $-2 \leq q \leq 4$, scaling actually operates over a sufficiently large range of scales for the estimate of the $\tau(q)$ exponents to be meaningful. The $\tau(q)$ spectra obtained from linear regression fits of the intron and exon data are shown in Fig. 6b. For both these noncoding and coding sequences, the data points fall remarkably on a straight line which indicates that the considered intron walks and exon walks are likely to display monofractal scaling. But

the slope of the staight line obtained for introns $H = \partial\tau(q)/\partial q = 0.60 \pm 0.02$ is definitely larger than the slope of the straight line derived for the exons $H = 0.53\pm0.02$. This is a clear indication that intron walks display long-range correlations ($H > 1/2$), while exon walks look much more like uncorrelated random walks ($H \simeq 1/2$). At first sight these results are in good agreement with the conclusions of previous studies concerning the existence of long-range correlations in noncoding DNA sequences only [24, 25, 164, 182] . Similar observations are reported in Refs. [158, 162], when investigating the largest individual introns and exons found in the EMBL data bank.

One of the most striking result of our WTMM analysis in Fig. 6, is the fact that the $\tau(q)$ spectra extracted for both sets of introns and exons, are well fitted by (28), $i.e.$, the analytical spectrum for fBm's. Let us note that this remarkable finding is robust with respect to change in the considered mononucleotide coding used to generate the random walks.

About the Gaussian character of the fluctuations in DNA walk landscapes

Within the perspective of confirming the monofractality of DNA walks, we have studied the probability density function (pdf) of wavelet coefficient values $\rho_a(T_{g^{(2)}}(.,a))$, as computed at a fixed scale a in the fractal scaling range. According to the monofractal scaling properties, one expects these pdfs to satisfy the self-similarity relationship:

$$a^H \rho_a(a^H T) = \rho(T) \ , \tag{34}$$

where $\rho(T)$ is a "universal" pdf (actually the pdf obtained at scale $a = 1$) that does not depend on the scale parameter a. In Refs. [158, 162], we have shown that when plotting $a^H \rho_a$ vs $a^H T$, all the ρ_a curves corresponding to different scales actually collapse on a unique curve when using the exponent $H = 0.6$ for the set of human introns and $H = 0.53$ for the set of human exons. Moreover, independently of the coding or noncoding nature of the sequences, the so-obtained universal pdfs cannot be distinguished from a Gaussian distribution. We will see in Fig. 9c and 9d, that similar gaussian WT coefficient statistics are observed, on a comparable range of (small) scales in between 10 and 200 nucleotides, for both the yeast and E-coli genomes. Thus, as explored through the optics of the WT microscope, the basic fluctuations (about the low frequency trends due to compositional patchiness) in DNA walks are likely to have monofractal Gaussian statistics. The presence of long-range correlations in the human introns is in fact contained in the scale dependence of the variance of this distribution, $\sigma^2(a) \sim a^{2H}$, with $H = 0.60 \pm 0.02$ like for persistent random walk fBms, as compared to the uncorrelated random walk value $H = 0.53\pm0.02 \simeq 1/2$ obtained for the coding sequences.
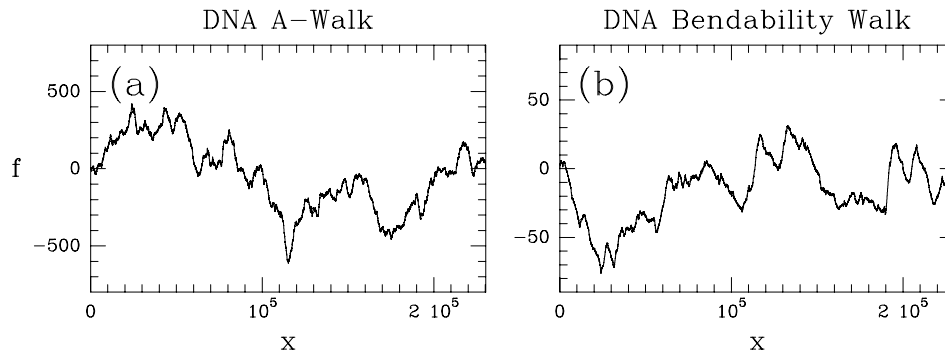
DNA A−Walk   DNA Bendability Walk

Fig. 7. DNA walk landscapes of the yeast chromosome I ($L = 230\,209$). (a) "A" mononucleotide coding. (b) Trinucleotide (PNuc) coding proposed in Ref. [188] to account for the fluctuations of the local DNA curvature.

Uncovering long-range correlations in coding DNA sequences

Because of the "period three" codon structure of coding DNA, it is natural to investigate separately the three subsequences relative to the position (1, 2 or 3) of the bases within their codons [160, 187]. We have build up these subsequences from our set of 226 human exons and we have repeated the WTMM analysis. The data obtained for the corresponding $\tau(q)$ spectra again fall on straight lines which corroborates monofractal scaling properties for the three subsequences. As shown in Fig. 6c for the subsequences relative to positions 1 and 2, one gets the same slope $h(q) = \partial\tau(q)/\partial q = 0.55 \pm 0.02$, which is undistinguishable from the value obtained for the overall coding sequences. Surprisingly, the data for the subsequence relative to position 3, exhibit a slope which is clearly larger $H = 0.58 \pm 0.02$, *i.e.*, a value which is very close to the exponent $H = 0.60 \pm 0.02$ estimated for the set of introns. This observation suggests that this third coding subsequence is likely to display the same degree of long-range correlations as noncoding sequences [160, 162]. We refer the reader to Refs. [160, 162] for the experimental demonstration that these long-range correlations are actually GC content dependent. Several mechanisms involved in the plasticity of genomes can be proposed to account for the observed long-range correlations. Among these mechanisms, one can exclude insertion-deletion events of DNA fragments of widely variable sizes which are very rare in exonic regions due to the strong constraints imposed by their coding properties. Selection pressure arguments can be further invoked to explain the difference between the correlations observed for the third bases of the codons as compared to those for bases 1 and 2. Indeed it is well known that most of the degeneracy of the genetic code is contained in codon position 3.

3.3   Towards a structural interpretation of the long-range correlations in DNA sequences

Recent success in DNA sequencing provide a wide range of investigation for statistical analysis of genomic sequences [189–195]. The availability of fully sequenced genomes offers the possibility to study scale-invariance properties of DNA sequences over a wide range of scales
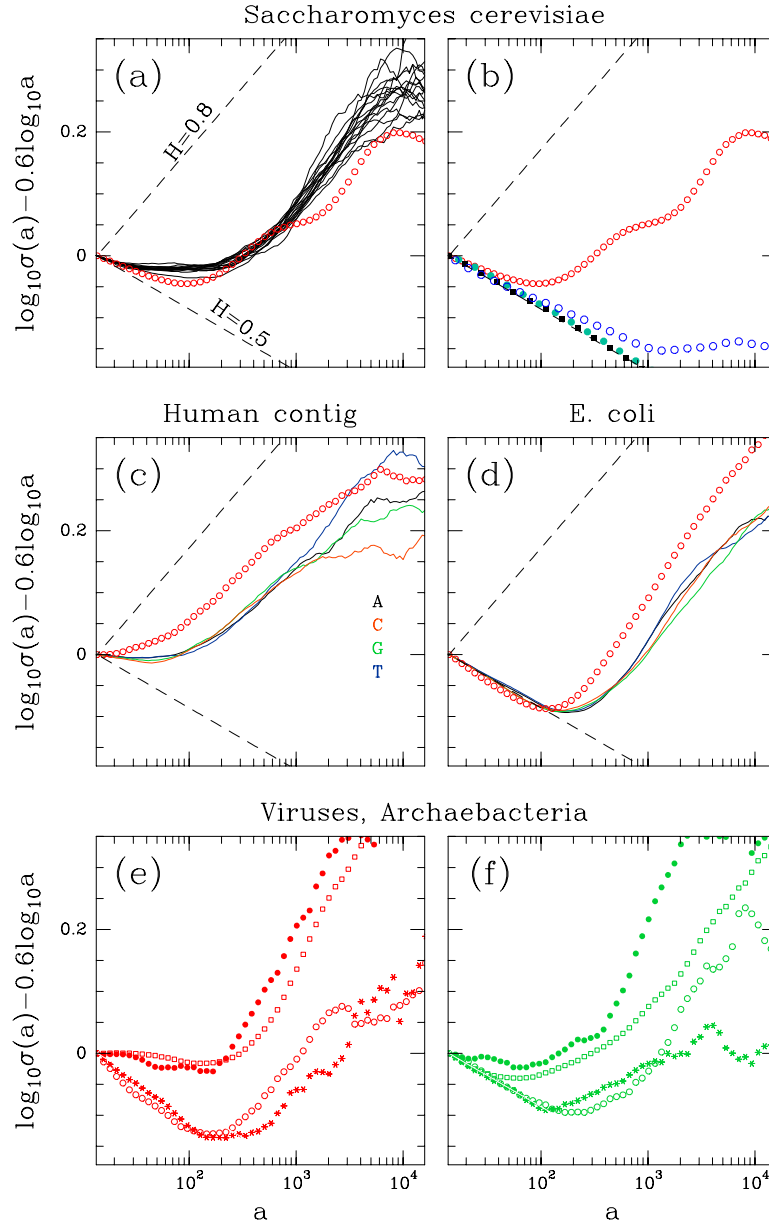
Fig. 8. Global estimate of the r.m.s. of WT coefficients of DNA walk landscapes. The analyzing wavelet is $g^{(2)}$ (20). $\log_{10} \sigma(a) - 0.6 \log_{10} a$ is plotted versus $\log_{10} a$; the dashed lines corresponding to uncorrelated ($H = 1/2$) and strongly correlated ($H = 0.80$) regimes are drawn to guide the eyes. *S.cerevisiae*: (a) Global estimate of the r.m.s of WT coefficients of the A DNA walks of the 16 *S. cerevisiae* chromosomes (solid lines) and of the corresponding bending profiles when averaged over the 16 chromosomes (red circles). (b) Comparative analysis for the true bending profile (red circles) and for a synthetic bending profile obtained by randomly changing the roll angle values as explained in the text (blue circles). The results are averaged over the 16 yeast chromosomes. Similar computations after randomly shuffling the original DNA sequences yield no correlations for both the A DNA walks (black squares) and the bending profiles (green dots). *Human contig*: (c) Comparative analysis of the A (black curve), C (orange curve), G (green curve) and T (blue curve) DNA walks and of the corresponding bending profiles (red circles). *Escherichia coli*: (d) Same representation as in (c). *Viruses, Archaebacteria : Archaeglobus fulgidus* (squares), *Epstein-barr virus* (dots), *Melanoplus sanguinipes entomapoxvirus* (circles) and *T4 bacteriophage* (stars): (e) "G" DNA walks; (f) bending profiles.

extending from tens to thousands of nucleotides. The first completely sequenced eucaryotic genome *Saccharomyces cerevisiae* [193] (*S.c*) provides an opportunity to perform a comparative wavelet analysis of the scaling properties displayed by each chromosome [161, 162] (Fig. 7a). When looking at the scale dependence of the root-mean square $\sigma(a)$ of the wavelet coefficient pdf computed with $g^{(2)}$ (20), over the DNA walks corresponding to "A" in each of the 16 yeast chromosomes, one sees, in Fig. 8a, that they all present superimposable behavior. We notably observe the same characteristic scale that separates two different scaling regimes. Let us note that common behavior to the 16 yeast chromosomes has already been pointed out in Refs. [196, 197]. At small scales, $20 \lesssim a \lesssim 200$, weak power-law correlations (PLC) are observed as characterized by $H = 0.59 \pm 0.02$, a mean value which is significantly larger than 1/2. At large scales, $200 \lesssim a \lesssim 5000$, strong PLC with $H = 0.82 \pm 0.01$ become dominant with a cutoff around 10000bp (a number which is by no means accurate) where uncorrelated behaviour is observed. (In this section the scale parameter is expressed in nucleotide units). The existence of these two scaling regimes is confirmed in Figs 9a, 9c and 9e [162], where the WT pdfs computed at different scales (Fig. 9a) are shown to collapse on a single curve, as predicted by the self-similarity relationship (34), provided one uses the scaling exponent value $H = 0.59$ in the scale range $10 \lesssim a \lesssim 100$ (Fig. 9c) and $H = 0.75$ in the scale range $200 \lesssim a \lesssim 1000$ (Fig. 9e). In the small scale regime, the pdfs are very well approximated by Gaussian distributions (Fig. 9c) which reminds the results of the WTMM analysis of noncoding eucaryotic sequences in section 3.2. In the large scale regime, the pdfs have stretched exponential-like tails (Fig. 9e). In both regimes, the fact that (34) is verified, corroborates the monofractal nature of the roughness fluctuations of the yeast DNA walks [162]. We have also examined other eucaryotic contigs from different organisms (human, rodent, avian, plant and insect) and we have observed the same characteristic features as those obtained with *S.c.*. In Fig. 8c, a similar characteristic scale $a^* \simeq 100$bp is clearly seen on a human contig. Moreover, the cross-over from a $H = 0.62 \pm 0.01$ to a $H = 0.75 \pm 0.02$ PLC regime is remarkly robust since the data for the four A, C, G and T DNA walks fall almost on the same curve in the range $20 \lesssim a \lesssim 2000$ [161, 162]. The striking overall similarity of the results obtained with these different eucaryotic genomes prompted us to also examine the scale invariance properties of bacterial genomes. In Figs. 8d, 9b, 9d and 9f, are reported the results obtained for *Escherichia coli* [198] which are typical of what we have observed with fifteen other bacterial genomes (data not shown) [161, 162]. Again, there exists a well defined characteristic scale $a^* \simeq 100 - 200$bp that delimits the transition to very strong PLC with $H = 0.85 \pm 0.02$ at large scales. In order to examine if these properties actually extend homogeneously over the whole genomes, $\sigma(a)$ was calculated over a window of width $l = 2000$, sliding along the DNA walk profiles. The results reported in Fig. 10 clearly reveal the existence of a characteristic scale $a^* \simeq 100 - 200$bp which seems to be robust all along the corresponding DNA molecules and this for all investigated genomes [161, 162]. There exists however an important difference between eucaryotic and bacterial genomes: no PLC are observed in the small-scale regime where uncorrelated $H = 1/2$ Brownian motion-like behaviour with is observed (Fig. 9d). At this point, it may seem that PLC are inherent to mostly non coding genomes, but that is not the case. As shown in Fig. 8e for *Archaeoglobus fulgidus*,

the wavelet investigation of five archaeal genomes (which are mostly coding) also reveals the presence of small-scale PLC as observed in eucaryotic genomes, although somewhat less pronounced [161, 162]. But the striking feature of these data is that the strong large-scale PLC are present in all bacterial, archaeabacterial and eucaryotic genomes [169, 170].

What mechanism or phenomenon might explain the small-scale PLC in eucaryotic genomes ? Their total absence in bacterial genomes raises the possibility that they could be related to certain nucleotide arrangements in the 150bp long DNA regions which are wrapped around histone proteins to form the eucaryotic nucleosomes [199–201]. Indeed, eubacterial genomic DNA is associated with histone-like proteins (e.g. Hu), but no nucleosome-type structure has been detected in these organisms [202]. Following this hypothesis, we have extended the application of the WT microscope to the investigation of the multi-scale properties of DNA bending signals that are likely to reflect the hierarchical organization of nucleoprotein complexes. To construct a bending profile that accounts for the fluctuations of the local DNA curvature, we use the trinucleotide (PNUC) model proposed in Ref. [188]. The results of the WTMM analysis of the bending profiles of the yeast chromosomes (Fig. 7b) are reported in Figs 8a and 8b [161, 162]. This analysis reveals striking similarities with the curves resulting from the DNA walk analysis, in both the small-scale and the large-scale regimes. To ensure that these observations are not simply due to a "recoding" of the DNA sequences, but due to the proper values of roll angles used to determine the bending profile, we have randomly changed the table that maps trinucleotides to roll-angle values. The new table is obtained using a Gaussian distribution of same mean, variance and symmetries as the original table [188]. As shown in Fig. 8b, this results in the vanishing of these PLC (now $H = 0.51 \pm 0.01$ at small scales), establishing that these PLC do indeed reflect persistent scale-invariant structural properties. We have also examined a number of eucaryotic and eubacterial genomes with similar conclusions [161, 162]. As shown in Figs 8c and 8d for a human contig and E. Coli, the structural information that is contained in the scaling properties of bending profiles can be directly extracted from the WTMM reading of the DNA texts [161, 162].

Following the nucleosomal interpretation of PLC in the small-scale regime, the observation of such correlations in archaeal genomes in Figs. 8e and 8f [161, 162] is consistent with the presence in archaebacteria of structures similar to the eucaryotic nucleosomes [203–207]. This analysis has also been extended to viral genomes. Small-scale PLC are clearly detected in organelle genomes and in most viral double-stranded DNA genomes (*Herpes-, Adeno-, Papova-, Parvo-* and *Hepadna- viruses*) as shown for *Epstein-barr virus* in Figs. 8e and 8f. This further supports the hypothesis of nucleosome-based PLC since nucleosomes have been observed on several classes of double-stranded DNA viruses [208, 209]. The Poxviridae, which are the only animal DNA viruses replicating in the cytoplasm of their host cells, code for a bacterial-type of histone-like protein [210], and no PLC are found in this scale range as shown in Figs. 8e and 8f for *Melanoplus sanguinipes* virus. This observation is consistent with our hypothesis and suggests that the genomic DNA of these viruses is submitted to packaging process different from other animal viruses. Finally, bacteriophage genomes do not present any small-scale PLC (Figs. 8e and 8f for *T4 bacteriophage* and data not shown) as already observed for their eubacterial hosts. Other classes of virus genomes
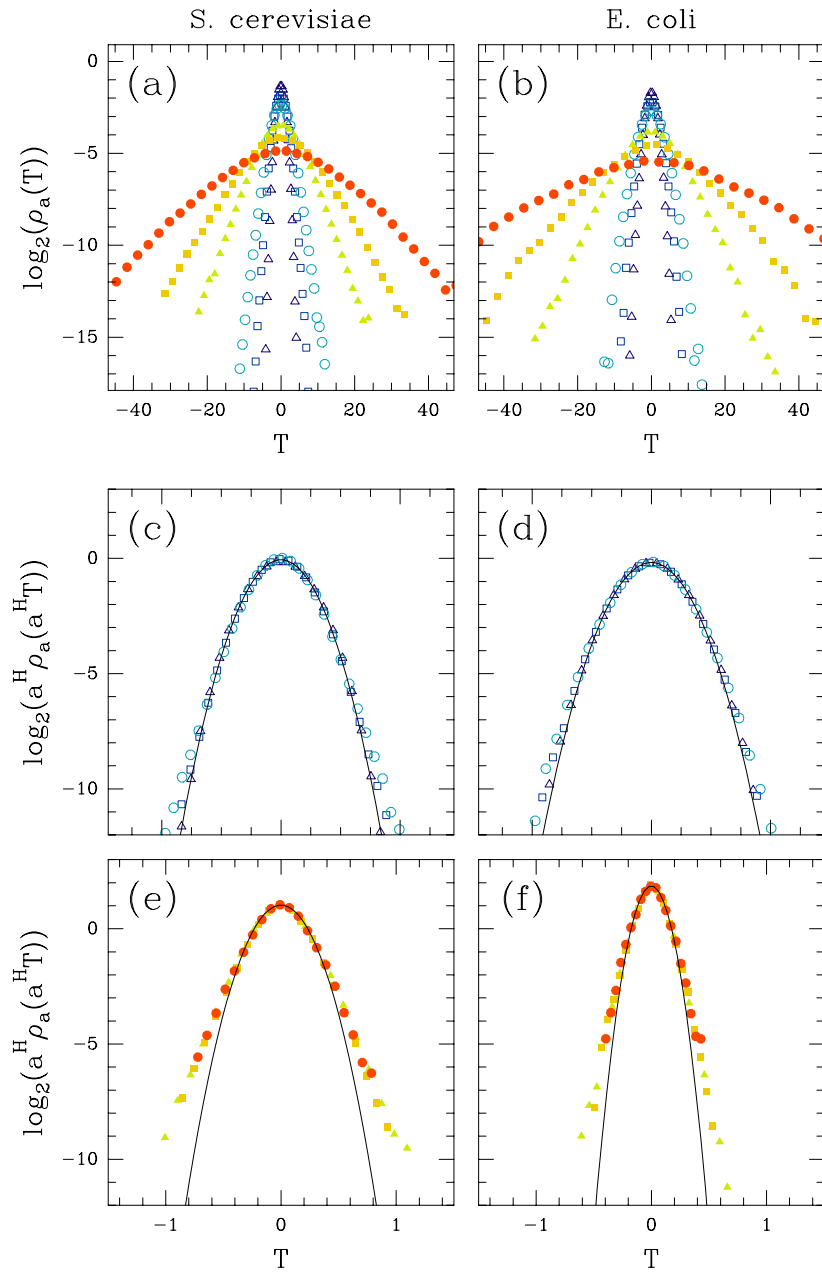
Fig. 9. Probability distribution functions of wavelet coefficient values of "A" DNA walks The analyzing wavelet is the Mexican hat $g^{(2)}$ (20). *S.cerevisiae*: (a) $\log_2(\rho_a)$ vs $T_{g^{(2)}}$ for the set of scales $a = 12$ ($\triangle$), 24 ($\square$), 48 ($\circ$), 192 ($\blacktriangle$), 384 ($\blacksquare$), and 768 ($\bullet$); (c) small-scale regime: $\log_2(a^H \rho_a(a^H T_{g^{(2)}}))$ vs $T_{g^{(2)}}$ with $H = 0.59$; (e) large-scale regime: $\log_2(a^H \rho_a(a^H T_{g^{(2)}}))$ vs $T_{g^{(2)}}$ with $H = 0.75$. *Escherichia coli*: (b) $\log_2(\rho_a)$ vs $T_{g^{(2)}}$ for the set of scales $a = 24$ ($\triangle$), 48 ($\square$), 96 ($\circ$), 384 ($\blacktriangle$), 768 ($\blacksquare$), and 1536 ($\bullet$); (d) small-scale regime: $\log_2(a^H \rho_a(a^H T_{g^{(2)}}))$ vs $T_{g^{(2)}}$ with $H = 0.50$; (f) large-scale regime: $\log_2(a^H \rho_a(a^H T_{g^{(2)}}))$ vs $T_{g^{(2)}}$ with $H = 0.80$.
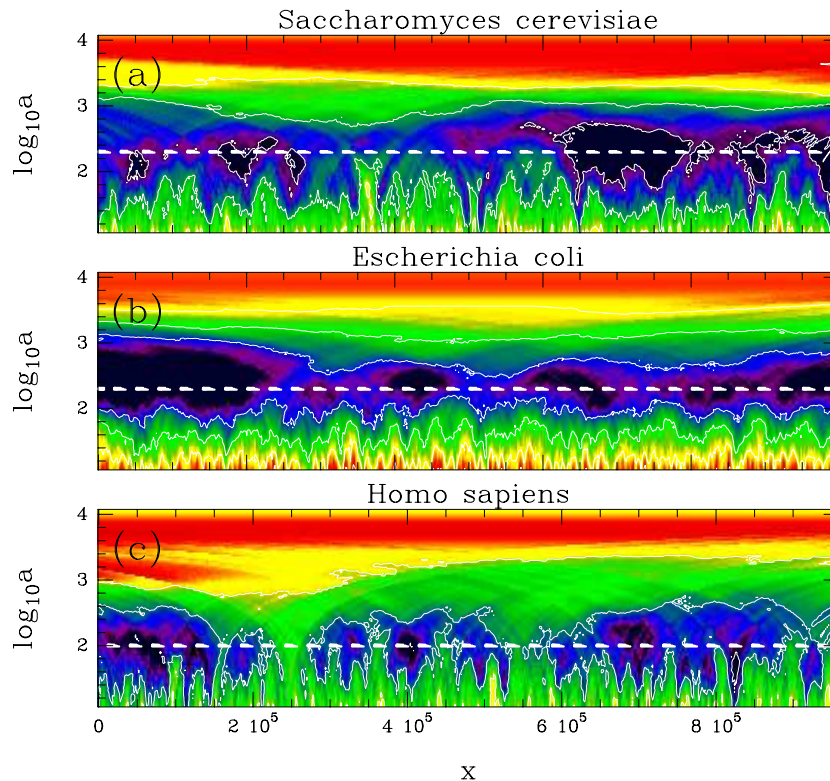
Fig. 10. Local estimate of the r.m.s $\sigma(a, x)$ of the WT coefficients of the A DNA walk, computed with the mexican hat analyzing wavelet $g^{(2)}$. $\sigma(a)$ is computed over a window of width $l = 2000$, sliding along the first 10^6bp of the *yeast* chromosome IV (a), *Escherichia coli* (b) and a human contig (c). $\log_{10} \sigma(a) - 2/3 \log_{10} a$ is coded using 128 colors from black (min) to red (max). In this space-scale wavelet like representation, x and a are expressed in nucleotide units. The horizontal white dashed lines mark the scale a^* where some minimum is observed consistenly along the entire genomes : $a^* = 200$bp for *S.cerevisiae*, $a^* = 200$bp for *E.coli* and $a^* = 100$bp for the human contig.

like the single and double-strand RNA viruses (to the exception of the retroviruses) are very unlikely associated to nucleosomes. In all cases except retroviruses, we observe a total absence of small-scale PLC. In the case of retroviruses, it is known that the integrated viral DNA is associated to nucleosomes in the cell nucleus [211]; we clearly confirm the presence of small-scale PLC ($H \simeq 0.57 \pm 0.02$). These wavelet based fractal analysis of viral and cellular genomes of all three kingdoms sustain without failure the fact that small-scale PLC provide a reliable diagnostic of the existence of eucaryotic nucleosomes.

Several studies have established the presence in genomic sequences of repetitive DNA motifs related to bending properties [212, 213]. It is noteworthy that a 10.2 base periodic modulation of correlation functions (not to be misunderstood with strict periodicity) is observed in eucaryotic genomes, where it has been interpreted in relation to nucleosomal structures. However there is a fundamental difference between this nucleosome diagnostic based on periodicity (*i.e.* invariance with respect to discrete translations) and our analysis based on scale invariance properties (*i.e.* invariance with respect to continuous dilations) which show up as a power law behaviour of the envelop of the correlation function. The

main conclusion of our WT analysis is that the mechanisms underlying the nucleosomal structure of eucaryotic genomes are likely to be multi-scale phenomena that involve the whole set of scales in the 1-200bp range. In other words, the bending sites are not positioned in a regular sequential manner, as suggested by the periodic-pattern picture, but are fractally distributed. A number of experimental observations help us interpreting our results. Nucleosomes can be regarded as mobile (nucleosome sliding [214]) and with inherently statistical positioning [215]. They also can be viewed as dynamical structures transiently exposing stretches of their DNA allowing access to regulatory proteins [216]. 'In that context, the understanding of small-scale PLC should provide further insight into the nucleosome structure and dynamics.

What mechanisms might explain the strongly correlated patterns observed on the DNA walks as well as on the corresponding bending profiles in all genomes, in the 200-5000bp range? As already suggested in Ref. [215], the signals involved in nucleosome binding and positioning may act collectively over large distances to the packing of nucleosomal arrays into high-order chromatin structures [199–201, 217]. Since DNA bending sites are key elements for nucleosomal structures, the detailed investigation of large-scale PLC observed in eucaryotic bending profiles should shed light on the compaction mechanisms at work in the hierarchical formation and dynamics of chromatin. An important clue provided by our studies is that similar long distance correlations in bending profiles are also observed in eubacteria and archaebacteria. It is then tempting to conjecture that the compaction of the eubacterial nucleoid in rosette-shaped chromosomal structures [218] is submitted to similar multi-scale structural constraints. Indeed, it is well established that architectural proteins interacting with DNA bending sites participate to the stabilisation of large nucleoprotein arrays, as for example, the eucaryotic HMG and the eubacterial HU histone-like proteins [219]. Moreover, the individual domains constituting the bacterial nucleoid are variable in size and position [220]. Actually eucaryotic, eubacterial and archaebacterial chromosomes are submitted to dynamical constraints that might result in scale invariant properties of the DNA text. For instance, large-scale PLC may result from DNA structural features related to the modulation of transcription, replication and recombination events [221–223]. A deep understanding of the large-scale PLC observed in DNA bending profiles as well as in DNA walks for all three kingdoms and their interpretation in terms of structural and dynamical properties remain challenging questions requiring further investigations.

4   The 2D wavelet transform modulus maxima method for the multifractal analysis of rough surfaces

Ever since the explosive propagation of fractal ideas [1] throughout the scientific community in the late 70's and early 80's, there have been numerous applications to surface science [5–8, 10–13, 16–18]. Both real space imaging techniques (including all kinds of microscopy and optical imaging techniques) and diffraction techniques have been extensively used to study rough surfaces [18]. The characterization of surface roughness is an important problem

from a fundamental point of view as well as for the wealth of potential applications in applied sciences. Indeed, a wide variety of natural and technological processes lead to the formation of complex interfaces [1–20]. Assigning a fractal dimension to those irregular surfaces is now become routine in various fields including topography, defect and fracture studies, growth phenomena, erosion and corrosion processes, catalysis and many other areas in physics, chemistry, biology, geology, meteorology and material sciences [1–20]. For rough surfaces which are well described by self-affine fractals with anisotropic scale-invariance [1, 5, 10, 22, 27, 28] various methods (e.g., divider, box, triangle, slit-island, power spectral, variogram and distribution methods) of computing D_F were shown to be very sensitive to limited resolution as well as finite-size effects [28, 29, 107, 108, 111, 224]. An alternative strategy consists in computing the so-called roughness exponent H [1, 5, 10] that describes the scaling of the width (or thickness) of the rough interface with respect to measurement scale. As for 1D signals (see sections 1 and 2.6), different methods [29, 30, 107, 108, 111, 113, 114] are available to estimate this exponent which is supposed to be related to the fractal dimension $D_F = d - H$ of self-affine surfaces embedded in a d-dimensional space. Again a number of artefacts may pollute the estimate of the roughness exponent. Since sensitivity and accuracy are method dependent, it is usually recommended to simultaneously use different tools in order to appreciate in a quantitative way, the level of confidence in the measured exponent.

The purpose of this section is to generalize the WTMM method described in section 2 [32, 35, 36, 42] from 1D to 2D, with the specific goal to achieve multifractal analysis of rough surfaces with fractal dimension D_F anywhere between 2 and 3. In recent years, increasing interest has been paid to the application of the WT to image processing [65, 77, 80, 85, 225–227]. In this context, Mallat and collaborators [40, 41] have extended the WTMM representation in 2D in a manner inspired from Canny's multiscale edge detectors commonly used in computer vision [228]. Our strategy will thus consists in using this representation to define a (3D) WT skeleton from which one can compute partition functions and ultimately extract multifractal spectra. A detailed description of this approach can be found in Refs. [229–233].

4.1   2D continuous wavelet transform for multi-scale edge detection

The edges of the different structures that appear in an image are often the most important features for pattern recognition. Hence, in computer vision [234, 235], a large class of edge detectors look for points where the gradient of the image intensity has a modulus which is locally maximum in its direction. As originally noticed by Mallat and collaborators [40, 41], with an appropriate choice of the analyzing wavelet, one can recast the Canny's multi-scale edge detector [228] in terms of a 2D WT. The general idea is to start smoothing the discrete image data by convolving it with a filter and then to compute the gradient on the smoothed signal.

Let us consider two wavelets that are, respectively, the partial derivatives with respect to x and y of a 2D smoothing function $\phi(x, y)$:

$$\psi_1(x, y) = \frac{\partial \phi(x, y)}{\partial x} \quad \text{and} \quad \psi_2(x, y) = \frac{\partial \phi(x, y)}{\partial y} . \tag{35}$$

We will assume that ϕ is a well localized (around $x = y = 0$) isotropic function that depends on $|\mathbf{x}|$ only. In this study, we will mainly use the gaussian function:

$$\phi(x, y) = e^{-(x^2 + y^2)/2} = e^{-|\mathbf{x}|^2/2} , \tag{36}$$

as well as the isotropic mexican hat:

$$\phi(\mathbf{x}) = (2 - \mathbf{x}^2) e^{-|\mathbf{x}|^2/2} . \tag{37}$$

The corresponding analyzing wavelets ψ_1 and ψ_2 are illustrated in Fig. 11. They have one and three vanishing moments when using respectively the gaussian function (36) and the mexican hat (37) as smoothing function.

For any function $f(x, y) \in L^2(\mathbb{R})$, the WT with respect to ψ_1 and ψ_2 has two components and therefore can be expressed in a vectorial form:

$$\mathbf{T}_{\boldsymbol{\psi}}[f](\mathbf{b}, a) = \begin{pmatrix} T_{\psi_1}[f] = a^{-2} \int d^2\mathbf{x}\, \psi_1\big(a^{-1}(\mathbf{x} - \mathbf{b})\big) f(\mathbf{x}) \\ T_{\psi_2}[f] = a^{-2} \int d^2\mathbf{x}\, \psi_2\big(a^{-1}(\mathbf{x} - \mathbf{b})\big) f(\mathbf{x}) \end{pmatrix} . \tag{38}$$

Then, after a straightforward integration by parts, one gets:

$$\begin{aligned} \mathbf{T}_{\boldsymbol{\psi}}[f](\mathbf{b}, a) &= a^{-2} \boldsymbol{\nabla} \left\{ \int d^2\mathbf{x}\, \phi\big(a^{-1}(\mathbf{x} - \mathbf{b})\big) f(\mathbf{x}) \right\} , \\ &= \boldsymbol{\nabla} \big\{ T_\phi[f](\mathbf{b}, a) \big\} , \\ &= \boldsymbol{\nabla} \big\{ \phi_{\mathbf{b}, a} * f \big\} . \end{aligned} \tag{39}$$

If $\phi(\mathbf{x})$ is simply a smoothing filter like the gaussian function (36), then (39) amounts to define the 2D wavelet transform as the gradient vector of $f(\mathbf{x})$ smoothed by dilated versions $\phi(a^{-1}\mathbf{x})$ of this filter. If $\phi(\mathbf{x})$ has some vanishing moments, then $T_\phi[f](\mathbf{b}, a)$ in (39) is nothing but the continuous 2D WT of $f(\mathbf{x})$ as defined by Murenzi [236, 237], provided $\phi(\mathbf{x})$ be an isotropic analyzing wavelet so that the integration over the angle θ becomes trivial.

As far as notations are concerned, we will mainly use the representation involving the modulus and the argument of the WT:

$$\mathbf{T}_{\boldsymbol{\psi}}[f](\mathbf{b}, a) = \big(\mathcal{M}_{\boldsymbol{\psi}}[f](\mathbf{b}, a), \mathcal{A}_{\boldsymbol{\psi}}[f](\mathbf{b}, a) \big) , \tag{40}$$

with

$$\mathcal{M}_{\boldsymbol{\psi}}[f](\mathbf{b}, a) = \left[\big(T_{\psi_1}[f](\mathbf{b}, a) \big)^2 + \big(T_{\psi_2}[f](\mathbf{b}, a) \big)^2 \right]^{1/2} , \tag{41}$$

and

$$\mathcal{A}_{\boldsymbol{\psi}}[f](\mathbf{b}, a) = \mathrm{Arg}\big(T_{\psi_1}[f](\mathbf{b}, a) + i T_{\psi_2}[f](\mathbf{b}, a) \big) . \tag{42}$$
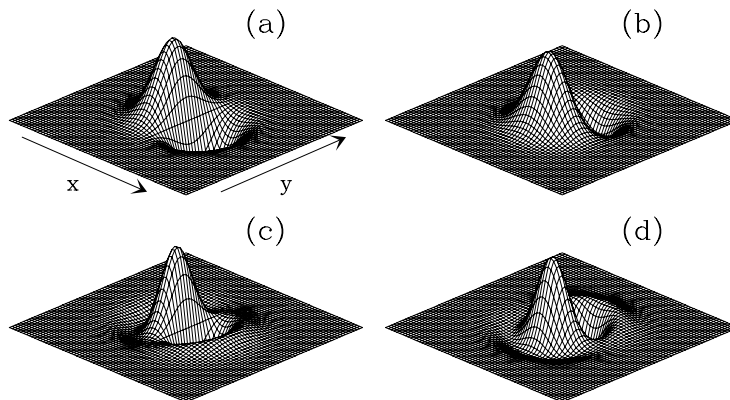
Fig. 11. The analyzing wavelet ψ_1 **and** ψ_2 defined in (35). First-order analyzing wavelets obtained from a gaussian smoothing function ϕ (36): (a) ψ_1; (b) ψ_2. Third-order analyzing wavelets obtained from the isotropic mexican hat smoothing function ϕ (37): (c) ψ_1; (d) ψ_2.

4.2 Characterizing the local regularity properties of rough surfaces with the wavelet transform modulus maxima

In the present study, we will use the term *rough surface* for an irregular surface on which there are no overhanging regions. This means that the surface can be correctly described by a function $z = f(\mathbf{x})$, which specifies the height of the surface at the point $\mathbf{x} = (x, y)$. Of particular interest are the rough surfaces corresponding to self-affine fractals in $\mathbb{R}^3$ [1, 5, 10, 22, 27, 28]. Moreover, we will assume that the considered functions possess only cusp-like singularities [231]. Under these assumptions, the situation is nevertheless trickier than in 1D [229–232]. Indeed, one has to distinguish two main cases depending on whether scale invariance is under isotropic or anisotropic dilations [1, 29, 135, 143, 144, 238].

Isotropic dilations: Local scale invariance under isotropic dilations means that locally, around the point $\mathbf{x}_0$, the function f behaves as:

$$f(\mathbf{x}_0 + \lambda\mathbf{u}) - f(\mathbf{x}_0) \simeq \lambda^{h(\mathbf{x}_0)}\big(f(\mathbf{x}_0 + \mathbf{u}) - f(\mathbf{x}_0)\big) , \qquad (43)$$

where $\lambda > 0$ and $\mathbf{u}$ is a unit vector. If the scaling exponent $h(\mathbf{x}_0)$ does not depend upon the direction of $\mathbf{u}$, then f displays isotropic local scale-invariance around $\mathbf{x}_0$ and the corresponding singularity is of Hölder exponent $h(\mathbf{x}_0)$. If, on the contrary, the scaling exponent depends upon the direction of $\mathbf{u}$, then the Hölder exponent is the minimum value of h over all the possible orientations of $\mathbf{u}$. Thus f displays anisotropic scale-invariance around $\mathbf{x}_0$ with one, several or a continuum of privileged directions along which the variation of f defines the Hölder exponent of the singularity located at $\mathbf{x}_0$.

Anisotropic dilations: Local scale invariance under anisotropic dilations means that locally around the point $\mathbf{x}_0$, the function f behaves as [133, 135, 143, 144, 238]:

$$f\big(\mathbf{x}_0 + \Lambda_\alpha(\lambda)r_\theta\mathbf{u}\big) - f(\mathbf{x}_0) \simeq \lambda^{h(\mathbf{x}_0)}\big(f(\mathbf{x}_0 + \mathbf{u}) - f(\mathbf{x}_0)\big) , \qquad (44)$$

where $\lambda > 0$ and $\mathbf{u}$ is a unit vector. r_θ is a rotation matrix and $\Lambda_\alpha(\lambda)$ is a positive diagonal 2×2 matrix that accounts for anisotropic self-affine scale transformation in the θ-rotated referential with origin $\mathbf{x}_0$:

$$\Lambda_\alpha(\lambda) = \begin{pmatrix} \lambda & 0 \\ 0 & \lambda^\alpha \end{pmatrix} . \tag{45}$$

The function f thus displays anisotropic scale-invariance around $\mathbf{x}_0$ and the Hölder exponent is given by the behavior of f in the direction θ ($\alpha < 1$) or $\theta + \pi/2$ ($\alpha > 1$).

Very much like the WT analysis of cusp singularities in 1D (section 2.2), in order to recover the Hölder exponent $h(\mathbf{x}_0)$ of a function f from $\mathbb{R}^2$ to $\mathbb{R}$, one needs to study the behavior of the WT modulus inside a cone $|\mathbf{x} - \mathbf{x}_0| < Ca$ in the space-scale half space [229, 230, 238]. As originally proposed by Mallat and collaborators [40, 41], a very efficient way to perform point-wise regularity analysis is to use the wavelet transform modulus maxima (WTMM). In the spirit of Canny edge detection [228], at a given scale a, the WTMM are defined as the points $\mathbf{b}$ where the WT modulus $\mathcal{M}_\psi[f](\mathbf{b}, a)$ (41) is locally maximum along the gradient direction given by the argument $\mathcal{A}_\psi[f](\mathbf{b}, a)$ (42). These modulus maxima are inflection points of $f * \phi_a(\mathbf{x})$. As illustrated in the example just below, these WTMM lie on connected chains hereafter called *maxima chains* [229–232]. In theory, one only needs to record the position of the local maxima of $\mathcal{M}_\psi$ along the maxima chains together with the value of $\mathcal{M}_\psi[f]$ and $\mathcal{A}_\psi[f]$ at the corresponding locations. At each scale a, our wavelet analysis thus reduces to store those WTMM maxima (WTMMM) only. They indicate locally the direction where the signal has the sharpest variation. This orientation component is the main difference between 1D and 2D WT analysis. These WTMMM are disposed along connected curves across scales called *maxima lines* [230, 231]. We will define the WT skeleton as the set of maxima lines that converge to the (x, y)-plane in the limit $a \to 0^+$. This WT skeleton is likely to contain all the information concerning the local Hölder regularity properties of the function f under consideration.

Let us first illustrate the above definitions on the function f shown in Fig. 12a:

$$f(\mathbf{x}) = A e^{-(\mathbf{x}-\mathbf{x}_1)^2/2\sigma^2} + B|\mathbf{x} - \mathbf{x}_0|^{0.3} . \tag{46}$$

This function is C^∞ everywhere except at $\mathbf{x} = \mathbf{x}_0$ where f is isotropically singular with a Hölder exponent $h(\mathbf{x}_0) = 0.3$. Its 2D WT (38) with a first-order analyzing wavelet (the smoothing function $\phi(\mathbf{x})$ is the isotropic gaussian function) is shown in Fig. 12b for a given scale $a = 2^3 \sigma_W$, where $\sigma_W = 13$ is the width (in pixel units) of the analyzing wavelet at the smallest scale where it is still well enough resolved. Actually, Fig. 12b illustrates the behavior of $\mathcal{M}_\psi[f]$. From a visual inspection of this figure, on can convince oneself that the modulus is radially symmetric around $\mathbf{x}_0$ where is located the singularity S. This is confirmed by the behavior of $\mathcal{A}_\psi[f]$ which rotates uniformly from 0 to 2π around $\mathbf{x}_0$. The WTMM as well as the WTMMM are shown in Fig. 12c for a discrete set of scales which allows us to reconstruct a three-dimensional representation in the space-scale half-space. At small scale, there exist mainly two maxima chains. One is a closed curve around $\mathbf{x}_0$ where is located the singularity S. The other one is an open curve which partially surrounds

the localized smooth structure G. On each of these maxima chains, one finds only one WTMMM (●) whose corresponding argument is such that the gradient vector points to S and G respectively. As far as the singularity S is concerned, this means that the direction of largest variation of f around S is given by $\theta_{\mathbf{x}_0} = \mathcal{A}_\psi[f] + \pi$, where $\mathcal{A}_\psi[f]$ is the argument of the corresponding WTMMM. When increasing the scale parameter, the maxima chains evolve; in particular the closed maxima chain around S swells (it characteristic size behaves like a) until it connects with the maxima chain associated with G to form a single closed curve surrounding both S and G. The topological evolution of the maxima chains in the space-scale half-space in Fig. 12c enlightens the existence of two maxima lines obtained by linking the WTMMM step by step (i.e. as continuously as possible) from small to large scales. One of these maxima lines points to the singularity S in the limit $a \to 0^+$. (To understand the bubble structure of $\mathcal{L}_{\mathbf{x}_0}(a)$ in Fig. 12c, we refer the reader to Refs. [231, 233] where a detailed description of the algorithm to construct the whole 3D skeleton in general situations is provided). As shown in Fig. 12d, along this maxima line $(\mathcal{L}_{\mathbf{x}_0}(a))$, the WT modulus behaves as [40, 41]

$$\mathcal{M}_\psi[f]\big(\mathcal{L}_{\mathbf{x}_0}(a)\big) \sim a^{h(\mathbf{x}_0)} , \ a \to 0^+ \tag{47}$$

where $h(\mathbf{x}_0) = 0.3 < n_\psi$ is the Hölder exponent of S. Moreover, along this maxima line, the WT argument evolves towards the value [231]:

$$\mathcal{A}_\psi[f]\big(\mathcal{L}_{\mathbf{x}_0}(a)\big) = \pi + \theta_{\mathbf{x}_0} , \tag{48}$$

in the limit $a \to 0^+$, where $\theta_{\mathbf{x}_0}$ is nothing but the direction of the largest variation of f around $\mathbf{x}_0$, i.e. the direction to follow from $\mathbf{x}_0$ to cross the maxima line at a given (small) scale. From the maxima line $\mathcal{L}_{\mathbf{x}_0}(a)$, one thus gets the required amplitude and directional informations to characterize the local Hölder regularity of f at $\mathbf{x}_0$. Note that along the other maxima line $\mathcal{L}_{\mathbf{x}_1}(a)$ which points to $\mathbf{x}_1$ where is located the smooth localized structure G, the WT modulus behaves as (Fig. 12e):

$$\mathcal{M}_\psi[f]\big(\mathcal{L}_{\mathbf{x}_1}(a)\big) \sim a^{n_\psi} , \ a \to 0^+ \tag{49}$$

where $n_\psi = 1$ is the order of the analyzing wavelet. Equations (47) and (49) can thus be seen as the analogs of (14) and (15) in 1D. We refer the reader to Ref. [231] where a similar WTMMM treatment is also shown to apply to anisotropic as well as self-affine singularities.

4.3   The 2D wavelet transform modulus maxima method

Methodology

Our strategy will consist in mapping the methodology developed in section 2.3 for multifractal analysis of irregular 1D landscapes, to the statistical characterization of roughness fluctuations of 2D surfaces [229–233]. The 2D WTMM method relies upon the space-scale
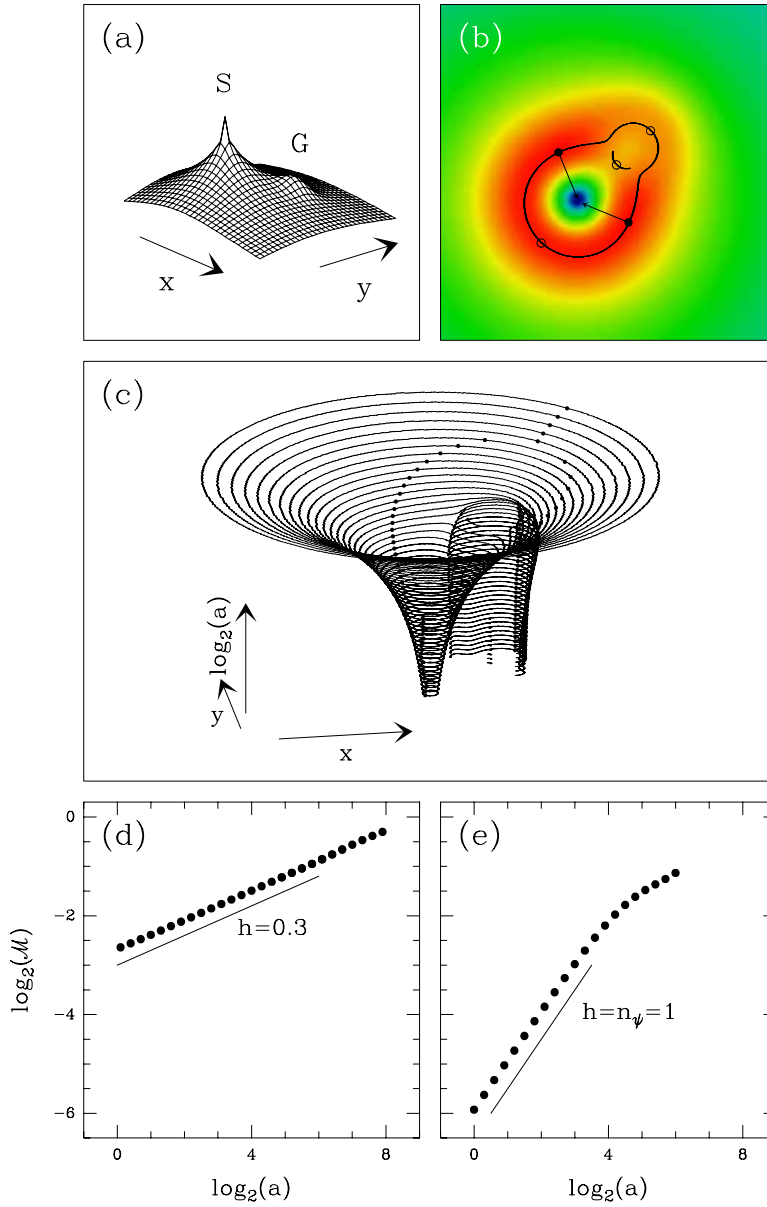
Fig. 12. Estimating the Hölder exponent from the behavior of the WT modulus along the maxima lines. (a) Graph of the function $f(\mathbf{x})$ defined in (46): the isotropic singularity S is located at $\mathbf{x}_0 = (-256, -256)$; the Gaussian localized structure G of width $\sigma = 128$ is located at $\mathbf{x}_1 = (256, 256)$; the parameters are $A = 1$ and $B = -1$. (b) $\mathcal{M}_\psi[f]$ coded from black ($\mathcal{M}_\psi = 0$) to red (max $\mathcal{M}_\psi$) with 256 colors as computed at scale $a = 2^3 \sigma_W$ where $\sigma_W = 13$ (pixels) is the characteristic size the first-order analyzing wavelet ψ (see Fig. 11) at the smallest resolved scale; the solid lines correspond to the maxima chains defined by the WTMM; the local maxima (resp. minima) along these chains are indicated by ($\bullet$) (resp. ($\circ$)) from which originates an arrow whose length is proportional to $\mathcal{M}_\psi[f]$ and its direction (with respect to the x-axis) is given by the WTMM argument $\mathcal{A}_\psi[f]$. (c) Three-dimensional representation of the topological evolution of the WTMM chains of f in the space-scale half-hyperplane. The WTMMM ($\bullet$) are disposed on connected curves called maxima lines. These maxima lines are obtained by linking each WTMMM computed at a given scale to the nearest WTMMM computed at the scale just above. There exist two maxima lines, $\mathcal{L}_{\mathbf{x}_0}$ and $\mathcal{L}_{\mathbf{x}_1}$, pointing respectively to the singularity S and to the smooth localized structure G in the limit $a \mapsto 0^+$. (d) Evolution of $\mathcal{M}_\psi[f]$ along $\mathcal{L}_{\mathbf{x}_0}$. (e) Evolution of $\mathcal{M}_\psi[f]$ along $\mathcal{L}_{\mathbf{x}_1}$.

partitioning given by the WT skeleton. As discussed in section 4.2, this skeleton (see Fig. 13e) is defined by the set of maxima lines which point to the singularities of the considered function and therefore is likely to contain all the information concerning the fluctuations of point-wise Hölder regularity. Let us define $\mathcal{L}(a)$ as the set of all maxima lines that exist at the scale a and which contain maxima at any scale $a' \leq a$. As discussed in section 4.2, the important feature is that each time the analyzed image has a Hölder exponent $h(\mathbf{x}_0) < n_{\boldsymbol{\psi}}$, there is at least one maxima line pointing towards $\mathbf{x}_0$ along which (47) is expected to hold. In the case of fractal functions, we thus expect that the number of maxima lines will diverge in the limit $a \to 0^+$, as the signature of the hierarchical organization of the singularities. The WTMM method consists in defining the following partition function directly from the WTMMM that belong to the WT skeleton:

$$Z(q, a) = \sum_{\mathcal{L} \in \mathcal{L}(a)} (\mathcal{M}_{\boldsymbol{\psi}}[f](\mathbf{x}, a))^q \,, \tag{50}$$

where $q \in \mathbb{R}$. As in 1D (section 2.3), from the scaling behavior of this partition function:

$$Z(q, a) \sim a^{\tau(q)} \,, \ a \to 0^+ \tag{51}$$

one can extract the $D(h)$ singularity spectrum (as defined as the Hausdorff dimension of the set of points such that the Hölder exponent of f is h) from a simple Legendre transform:

$$D(h) = \min_q \left(qh - \tau(q) \right) \,. \tag{52}$$

Probability density functions

From the definition of the partition function in (50), one can transform the discrete sum over the WTMMM into a continuous integral over $\mathcal{M}_{\boldsymbol{\psi}}[f]$:

$$Z(q, a)/Z(0, a) = < \mathcal{M}^q > (a) = \int d\mathcal{M} \, \mathcal{M}^q P_a(\mathcal{M}) \,. \tag{53}$$

The multifractal description thus consists in characterizing how the moments of the pdf $P_a(\mathcal{M})$ of $\mathcal{M}$ behave as a function of the scale parameter a. The power-law exponents $\tau(q)$ in (51), therefore quantify the evolution of the shape of the $\mathcal{M}$ pdf across scales. At this point, let us remark that one of the main advantage of using the WT skeleton is the fact that, by definition, $\mathcal{M}$ is different from zero and consequently that $P_a(\mathcal{M})$ generally decreases exponentially fast to zero at zero. This observation is at the heart of the WTMM method since, for this reason, one can not only compute the $\tau(q)$ spectrum for $q > 0$ but also for $q < 0$ [229–232]. From the Legendre transform of $\tau(q)$ (52), one is thus able to compute the whole $D(h)$ singularity spectrum, i.e., its increasing left part ($q > 0$) as well as its decreasing right part ($q < 0$).

But, although we have decided to mainly use isotropic analyzing wavelets, we have seen in section 4.2 that from the analysis of the WT skeleton, one is able to also extract directional informations via the computation of $\mathcal{A}_\psi[f](\mathbf{x}, a)$. It is thus very instructive to extend our statistical analysis to the investigation of the joint pdf $P_a(\mathcal{M}, \mathcal{A})$ [230, 231]. Two main situations have to be distinguished:

(i) $\mathcal{M}$ and $\mathcal{A}$ are independent. This means that, whatever the scale a, the joint pdf factorizes:

$$P_a(\mathcal{M}, \mathcal{A}) = P_a(\mathcal{M})P_a(\mathcal{A}) . \tag{54}$$

In other words, the Hölder exponent h is statistically independent of the direction $\theta = \mathcal{A} + \pi$ to which it is associated. This implies that the $D(h)$ singularity spectrum is decoupled from the angular information contained in $P_a(\mathcal{A})$. If this angle pdf is flat, this means that the rough surface under study displays isotropic scale invariance properties. If, on the contrary, this pdf is a non uniform distribution on $[0, 2\pi]$, this suggests that some anisotropy is present in the analyzed image. The possible existence of privilegied directions can then be revealed by investigating the correlations between the values of $\mathcal{A}$ for different maxima lines. Furthermore, $P_a(\mathcal{A})$ may evolve when varying the scale parameter a. The way its shape changes indicates whether (and how) anisotropy is enhanced (or weakened) when going from large scales to small scales. Even though we are mainly interested in the scaling properties in the limit $a \to 0^+$, the evolution of the shape of $P_a(\mathcal{A})$ across scales is likely to enlighten possible deep structural changes.

(ii) $\mathcal{M}$ and $\mathcal{A}$ are dependent. If equation (54) definitely does not apply, this means that the rough surface under consideration is likely to display anisotropic scale invariance properties. By conditioning the statistical analysis of $\mathcal{M}$ to a given value of $\mathcal{A}$, one can then investigate the scaling properties of the conditioned partition function:

$$\begin{aligned} Z_\mathcal{A}(q, a) &= Z_\mathcal{A}(0, a) \int d\mathcal{M} \, \mathcal{M}^q P_a(\mathcal{M}|\mathcal{A}), \\ &\sim a^{\tau_\mathcal{A}(q)} . \end{aligned} \tag{55}$$

Then by Legendre transforming $\tau_\mathcal{A}(q)$, one gets the singularity spectrum $D_\mathcal{A}(h)$ conditioned to the value of the angle $\mathcal{A}$ $(= \theta - \pi)$. The investigation of the $\mathcal{A}$-dependence of the singularity spectrum $D_\mathcal{A}(h)$ can be rich of information concerning anisotropic multifractal scaling properties.

Remark 3: There have been previous attempts in the literature to carry out anisotropic multifractal analysis. In the context of geophysical (fracture and faulting) data analysis, Ouillon *et al.* [239–241] have used an optimized anisotropic wavelet coefficient method to detect and characterize the different levels of mineral organization via the changes of statistical scale invariance. From a mathematical point of view, Ben Slimane [238] has recently proposed a way to generalize the multifractal formalism to anisotropic self-similar functions. His strategy consists in modifying the definition of the 2D WT so that anisotropic zooming is operationally integrated in the optics of this mathematical microscope.

4.4   Application of the 2D WTMM method to synthetic isotropic monofractal and multifractal rough surfaces

Fractional Brownian surfaces

The generalization of Brownian motion to more than one dimension was first considered by Levy [242]. The generalization of fBm follows along similar lines. A 2D fBm $B_H(\mathbf{x})$ indexed by $H \in]0, 1[$, is a process with stationary zero-mean Gaussian increments and whose correlation function is given by [1, 22, 242]:

$$< B_H(\mathbf{x})B_H(\mathbf{y}) >= \frac{\sigma^2}{2} \left(|\mathbf{x}|^{2H} + |\mathbf{y}|^{2H} - |\mathbf{x} - \mathbf{y}|^{2H}\right) \ , \tag{56}$$

where $< \ldots >$ represents the ensemble mean value. The variance of such a process is

$$\mathrm{var}\big(B_H(\mathbf{x})\big) = \sigma^2|\mathbf{x}|^{2H} \ , \tag{57}$$

from which one recovers the classical behavior $\mathrm{var}(B_{1/2}(\mathbf{x})) = \sigma^2|\mathbf{x}|$ for Brownian motion with $H = 1/2$. 2D fBm's are self-affine processes that are statistically invariant under isotropic dilations:

$$B_H(\mathbf{x}_0 + \lambda\mathbf{u}) - B_H(\mathbf{x}_0) \backsimeq \lambda^H[B_H(\mathbf{x}_0 + \mathbf{u}) - B_H(\mathbf{x}_0)] \ , \tag{58}$$

where $\mathbf{u}$ is a unitary vector and $\backsimeq$ stands for the equality in law. The index H corresponds to the Hurst exponent; the higher the exponent H, the more regular the fBm surface. But since (58) holds for any $\mathbf{x}_0$ and any direction $\mathbf{u}$, this means that almost all realizations of the fBm process are continuous, everywhere non-differentiable, isotropically scale-invariant as characterized by a unique Hölder exponent $h(\mathbf{x}) = H$ [1, 22, 125], $\forall\mathbf{x}$. Thus fBm surfaces are the representation of homogeneous stochastic fractal functions characterized by a singularity spectrum which reduces to a single point

$$\begin{aligned} D(h) &= 2 && \text{if } h = H \ , \\ &= -\infty && \text{if } h \neq H \ . \end{aligned} \tag{59}$$

By Legendre transforming $D(h)$ according to (52), one gets the following expression for the partition function exponent (51):

$$\tau(q) = qH - 2 \ . \tag{60}$$

$\tau(q)$ is a linear function of q, the signature of monofractal scaling, with a slope given by the index H of the fBm.

We have tested the 2D WTMM method described in section 4.3 [231] on fBm surfaces generated by the so-called fast Fourier transform filtering method [22, 27]. We have used this particular synthesis method because of its implementation simplicity. Indeed it amounts to a fractional integration of a 2D "white noise" and therefore it is expected to reproduce quite faithfully the expected isotropic scaling invariance properties (58). We have investigated

fBm's for various values of the index H. Here we report, for illustration, the results obtained on 32 realizations of a 2D fBm process with $H = 1/3$. Along the lines of the numerical implementation procedure described in section 4.2 [231], we have wavelet transformed 32 (1024×1024) images of $B_{H=1/3}$ with an isotropic first-order analyzing wavelet. To master edge effects, we then restrain our analysis to the 512×512 central part of the WT of each image. In Fig. 13c is illustrated the computation of the maxima chains and the WTMMM for an individual image at a given scale. In this figure is also shown the convolution of the original image (Fig. 13a) with the isotropic gaussian smoothing filter ϕ (39). According to the definition of the WTMM, the maxima chains correspond to well defined edge curves of the smoothed image. The local maxima of $\mathcal{M}_\psi$ along these curves are located at the points where the sharpest intensity variation is observed. The corresponding arrows clearly indicate that locally, the gradient vector points to the direction (as given by $\mathcal{A}_\psi$) of maximum change of the intensity surface. When going from large to small scale, the average distance between two nearest neighbour WTMMM decreases like a. This means that the number of WTMMM and in turns, the number of maxima lines, proliferates across scales like a^{-2}. The corresponding WT skeleton is shown in Fig. 13e. As confirmed just below, when extrapolating the arborescent structure of this skeleton to the limit $a \to 0^+$, one recovers the theoretical result that the support of the singularities of a 2D fBm has a dimension $D_F = 2$, i.e., $B_{H=1/3}(\mathbf{x})$ is nowhere differentiable [1, 22, 242].

In Fig. 14 are reported the results of the computation of the $\tau(q)$ and $D(h)$ spectra using the 2D WTMM method described in section 4.3. As shown in Fig. 14a, for $q \in [-4, 6]$, the annealed average partition function $Z(q, a)$ (over 32 images of $B_{1/3}(\mathbf{x})$) display a well defined scaling behavior over more than 3 octaves. When proceeding to a linear regression fit of the data over the first two octaves, one gets the $\tau(q)$ spectrum (51) shown in Fig. 14c. The data systematically fall on a straight line which is in remarkable agreement with the theoretical $\tau(q)$ spectrum (60) with $H = 1/3$. As shown in Fig. 14d, it is therefore not surprising that the $D(h)$ spectrum obtained by Legendre transforming the $\tau(q)$ data reduce to a single point $D(h = H = 1/3) = 2.00 \pm 0.02$ (59).

In Fig. 15 are shown the pdfs $P_a(\mathcal{M}) = \int d\mathcal{A} P_a(\mathcal{M}, \mathcal{A})$ and $P_a(\mathcal{A}) = \int d\mathcal{M} P_a(\mathcal{M}, \mathcal{A})$, for four different values of the scale parameter. As seen in Fig. 15a, $P_a(\mathcal{M})$ is not a Gaussian (in contrast to the pdf of the continuous 2D wavelet coefficients), but decreases very fast to zero at zero as expected when using the WTMM method. The corresponding pdf's $P_a(\mathcal{A})$ are represented in Fig. 15c. $P_a(\mathcal{A})$ clearly does not evolve across scales. Moreover, except some small amplitude fluctuations observed at the largest scale, $P_a(\mathcal{A}) = 1/2\pi$ is a flat distribution as expected for statistically isotropic scale-invariant rough surfaces. The results reported in Fig. 15e, not only corroborate statistical isotropy but they bring unambiguous evidence for the independence of $\mathcal{M}$ and $\mathcal{A}$ (54). For two different scales, the pdf of $\mathcal{M}$, when conditionned by the argument $\mathcal{A}$, is shown to be shape invariant.
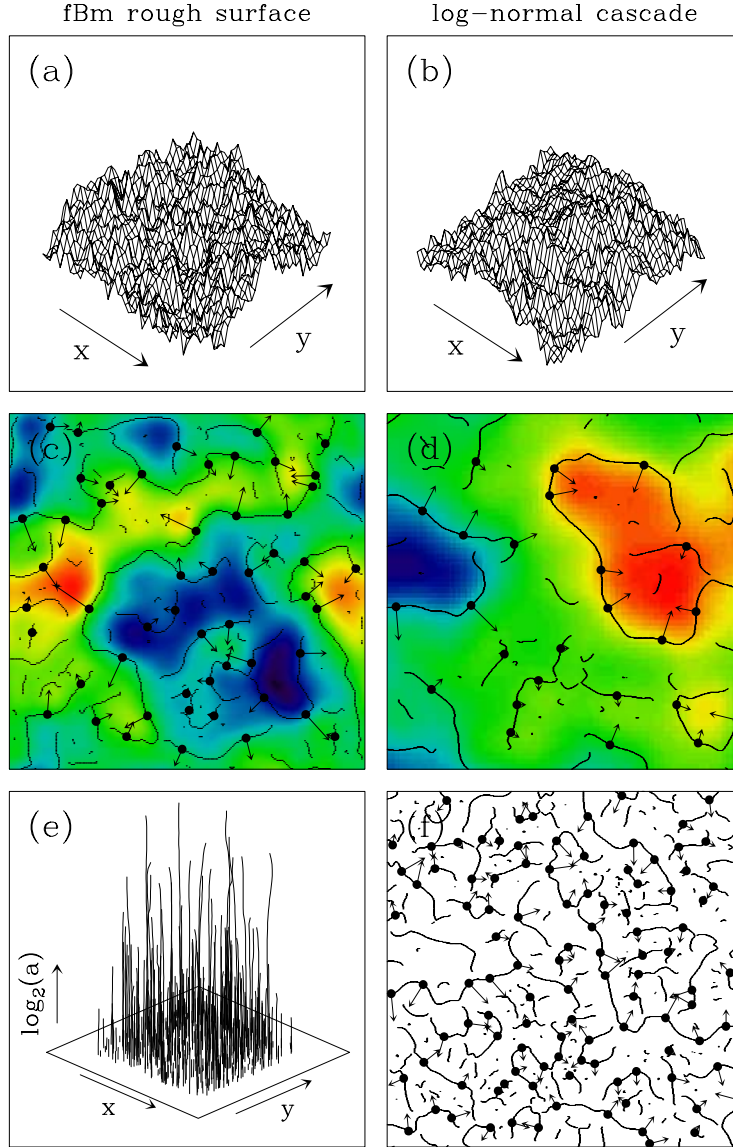
fBm rough surface   log−normal cascade

Fig. 13. Continuous WT of monofractal and multifractal synthetic rough surfaces. *Fractional Brownian rough surfaces:* (a) A (1024×1024) realization of a $H = 1/3$ fBm rough surface; (c) maxima chains defined by the WTMM as computed at the scale $a = 2^2 \sigma_W$; the WTMMM (•) are defined by the local maxima of $\mathcal{M}_\psi$ along the chains; (e) the WT skeleton defined by the maxima lines obtained after linking the WTMMM detected at different scales. *Log-normal random 2D $\mathcal{W}$-cascades:* (b) A (1024×1024) rough surface generated using the log-normal $\mathcal{W}$-cascade model with the parameter values $m = -0.35 \ln 2$ and $\sigma^2 = 0.03 \ln 2$; (d) maxima chains and WTMMM as computed at the scale $a = 2^3 \sigma_W$; (f) same as in (d) but at the scale $a = 2\sigma_W$. In (c) and (d), the smoothed image $\phi_{\mathbf{b},a} \star f$ is shown as a color coded background from black (min) to red (max). ψ is the first-order radially symmetric wavelet shown in Fig. 11.
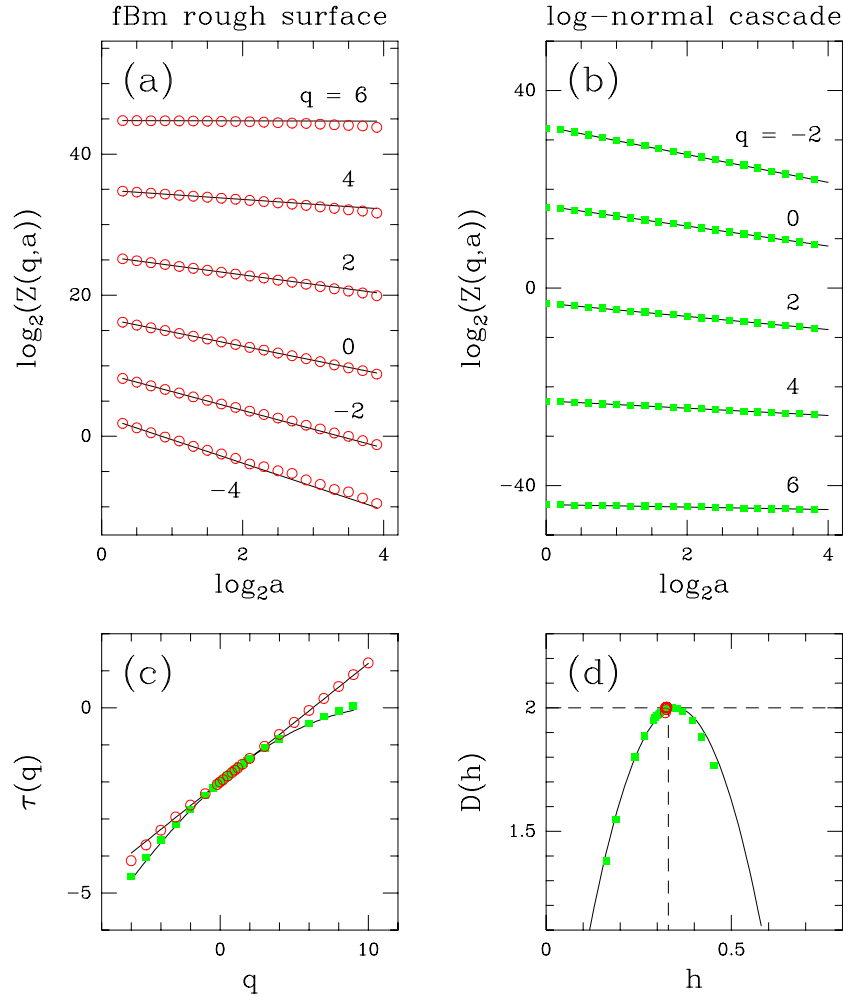
Fig. 14. Determination of the $\tau(q)$ **and** $D(h)$ **multifractal spectra** of fractional Brownian rough surfaces with $H = 1/3$ (red circles) and log-normal random 2D $\mathcal{W}$-cascades (green squares) using the 2D WTMM method. (a) $\log_2 Z(q,a)$ vs $\log_2 a$: $B_{1/3}(\mathbf{x})$. (b) $\log_2 Z(q,a)$ vs $\log_2 a$: log-normal $\mathcal{W}$-cascade with the same parameters as in Fig. 13b. (c) $\tau(q)$ vs q; the solid lines correspond respectively to the theoretical spectra given by (60) and (61). (d) $D(h)$ vs h; the solid lines correspond respectively to the theoretical predictions given by (59) and (62). The analyzing wavelet is the same as in Fig. 13. The reported results correspond to annealed averaging over 32 (1024×1024) realizations.

2D random $\mathcal{W}$-cascades

As originally introduced in Ref. [232], the concept of $\mathcal{W}$-cascade [102–106] (section 2.6) can be generalized in 2D in order to generate synthetic multifractal functions of two variables. A 2D random $\mathcal{W}$-cascade is built recursively on the two-dimensional square grid of separable wavelet orthogonal basis, involving only scales that range between a given large scale L and the scale 0 (excluded). Thus the corresponding fractal function $f(\mathbf{x})$ will not involve scales greater than L. For that purpose, we will use compactly supported wavelets defined by Daubechies [73]. In Fig. 13b is shown a rough surface generated with the log-normal $\mathcal{W}$-
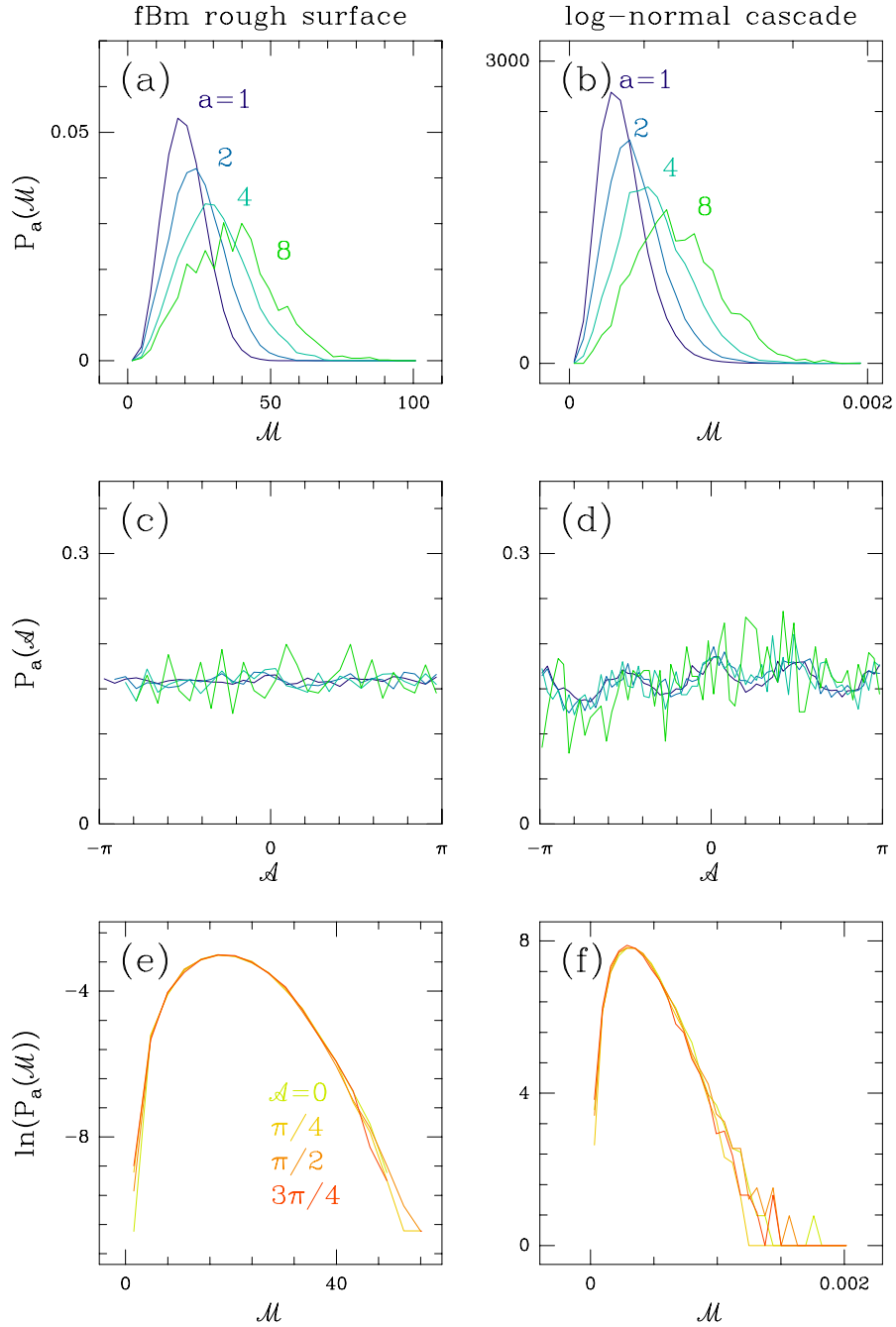
Fig. 15. Pdf's of the WTMMM coefficients as computed at the scales $a = 1$, 2, 4 and 8 (in σ_W units). *Fractional Brownian rough surfaces:* (a) $P_a(\mathcal{M})$ vs $\mathcal{M}$; (c) $P_a(\mathcal{A})$ vs $\mathcal{A}$; (e) pdf's of $\mathcal{M}$ when conditioned by $\mathcal{A}$, at the scale $a = \sigma_W$. *Log-normal random 2D $\mathcal{W}$-cascades:* (b) $P_a(\mathcal{M})$ vs $\mathcal{M}$; (d) $P_a(\mathcal{A})$ vs $\mathcal{A}$; (f) pdf's of $\mathcal{M}$ when conditioned by $\mathcal{A}$, at the scale $a = 2^{0.1}\sigma_W$. In (e) and (f) the different curves correspond to fixing $\mathcal{A}$ (mod π) to $0 \pm \pi/8$, $\pi/4 \pm \pi/8$, $\pi/2 \pm \pi/8$ and $3\pi/4 \pm \pi/8$. Same 2D WTMM computations as in Fig. 14.

cascade model proposed in Ref. [232]. The multifractal spectra have the following analytical expression:

$$
\begin{aligned}
\tau(q) &= -\log_2 < W^q > -2 \ , \ \forall q \in \mathbb{R} \\
&= -\frac{\sigma^2}{2\ln 2}q^2 - \frac{m}{\ln 2}q - 2 \ ,
\end{aligned}
\tag{61}
$$

and

$$
D(h) = -\frac{(h + m/\ln 2)^2}{2\sigma^2/\ln 2} + 2 \ ,
\tag{62}
$$

which are reminiscent of (29) and (30) derived for 1D log-normal $\mathcal{W}$-cascades. Let us mention that (31) and (32) are slightly modified in 2D (indeed one has simply to replace σ^2 by $2\sigma^2$ in these formula).

In Figs. 13, 14 and 15, we mainly report results obtained with the first-order radially symmetric analyzing wavelets shown in Fig. 11. Let us point out that quite robust results are obtained with the third-order analyzing wavelet. In Figs. 13d and 13f is illustrated the computation of the maxima chains and the WTMMM for an individual image (Fig. 13b) of a multifractal rough surface generated with the log-normal $\mathcal{W}$-cascade model described in Ref. [232]. The model parameters are $m = -0.35\ln 2$ and $\sigma^2 = 0.03\ln 2$. From the WTMMM defined on these maxima chains, one constructs the WT skeleton according to the procedure described in sections 4.2 and 4.3. From the WT skeletons of 32 (1024×1024) images like the one in Fig. 13b, one computes the annealed average of the partition functions $Z(q, a)$. As shown in Fig. 14b, when plotted versus the scale parameter a in a logarithmic representation, these annealed average partition functions display a well defined linear behavior over a range of scales of about 4 octaves (i.e., $\sigma_W \lesssim a \lesssim 16\sigma_W$, where $\sigma_W = 13$ pixels). Let us point out that scaling of quite good quality is found for a rather wide range of values of q: $-6 \lesssim q \lesssim 8$. When processing to a linear regression fit of the data over the first four octaves, one gets the $\tau(q)$ spectrum ($\blacksquare$) shown in Fig. 14c. For the range of investigated q values, the numerical data are in remarkable agreement with the theoretical nonlinear $\tau(q)$ spectrum given by (61). Similar quantitative agreement is observed on the $D(h)$ singularity spectrum in Fig. 14d. This is the quantitative demonstration that the 2D WTMM method is able to resolve mulifractality. From the theoretical spectra, the multifractal rough surfaces under study, display intermittent fluctuations corresponding to Hölder exponent values ranging from $h_{\min} = 0.005$ to $h_{\max} = 0.700$. Unfortunately, to capture the strongest and weakest singularities, one needs to compute the $\tau(q)$ spectrum for very large values of $|q|$. This requires the processing of many more images of much larger size, which is out of our current computer capabilities. Note that with the statistical sample studied here, one has $D(h(q = 0) = 0.35) = 2.00 \pm 0.02$, which allows us to conclude that the rough surfaces under consideration are singular everywhere.

Remark 4: Note that we have chosen on purpose the parameters m and σ^2 so that the spectral exponent $\beta = 4 - \tau(2) = 2.66$ be the same for the $B_{1/3}$ monofractal rough surfaces and the log-normal $\mathcal{W}$ rough surfaces. The results reported in this section show that the 2D WTMM method succeeds in distinguishing monofractal and multifractal surfaces that exhibit exactly the same density spectrum power law decay.

From the construction rule of these synthetic log-normal rough surfaces [232, 233], the multifractal nature of these random functions is expected to be contained in the way the shape of the WT modulus pdf $P_a(\mathcal{M})$ evolves when varying the scale parameter a, as shown in Fig. 15b. Indeed the joint pdf $P_a(\mathcal{M}, \mathcal{A})$ is expected to factorize, as the signature of the implicit decoupling of $\mathcal{M}$ and $\mathcal{A}$ in the construction process. This decoupling is numerically retrieved in Fig. 15f, where, for two different scales, the pdf of $\mathcal{M}$, when conditioned by the argument $\mathcal{A}$, is shown to be shape invariant. Moreover, as seen in Fig. 15d, $P_a(\mathcal{A})$ does not exhibit any significant change when increasing a, except some loss in statistical convergence at large scales due to the rarefaction of the maxima lines. Let us point out that, even though $P_a(\mathcal{A})$ looks globally rather flat, one can notice some small amplitude almost periodic oscillations at the smallest scales which reflects the existence of privileged directions in the wavelet cascading process. These oscillations are maximum for $\mathcal{A} = 0$, $\pi/2$, π and $3\pi/2$, as the witness to the square lattice anisotropy underlying the 2D wavelet tree decomposition.

5   Application of the 2D WTMM method to high-resolution satellite images of cloud structure

The problematic of nonlinear variability over a wide range of scales has been considered for a long time with respect to the highly intermittent nature of turbulent flows in fluid dynamics [15, 67]. Special attention has been paid to their asymptotic and possibly universal behavior when the dissipation length goes to zero, *i.e.*, when the Reynolds number goes to infinity. Besides wind-tunnel and laboratory (grid, jet, ...) experiments, the atmosphere is a huge natural laboratory where high Reynolds number (fully developed) turbulent dynamics can be studied. Clouds, which are at the source of the hydrological cycle, are the most obvious manifestation of the earth's turbulent atmospheric dynamics [16, 243–245]. By modulating the input of solar radiation, they play a critical role in the maintenance of the earth's climate [246]. They are also one of the main sources of uncertainty in current climate modeling [247], where clouds are assumed to be homogeneous media lying parallel to the earth's surface; at best, a linear combination of cloudy and clear portions according to cloud fraction is used to account for horizontal inhomogeneity when predicting radiative properties. During many years, the lack of data hindered our understanding of cloud microphysics and cloud-radiation interactions. Nowadays, it is well-recognized that clouds are variable in all directions and that fractal [243, 244, 248–253] and multifractal [16, 245, 254–256] concepts are likely to be relevant to the description of their complex

3D geometry. Until quite recently, the internal structure of clouds was probed by balloons or aircrafts that penetrated the cloud layer, revealing an extreme variability of 1D cuts of some cloud fields [256–264]. In particular, *in situ* measurements of cloud liquid water content (LWC) were performed during many intensive field programs (FIRE [265], ASTEX [266], SOCEX [267] ...). Indeed, during the past fifteen years, vast amounts of data on the distribution of atmospheric liquid water from a variety of sources were collected and analyzed in many different ways. All these data contain information on spatial and/or temporal correlations in cloudiness, enabling the investigation of scale invariance over a range from a few centimeters to hundred of kilometers. An attractive alternative to *in situ* probing is to use *high-resolution satellite imagery* that now provides direct information about the fluctuations in liquid water concentration in the depth of clouds [244, 249, 251, 253, 268–273]. These rather sophisticated remote sensing systems called "millimeter radars" are actually sensitive not only to precipitating rain drops but also to suspended cloud droplets. Spectral analysis of the recorded 2D radiance field [268–273] confirms previous 1D findings that make it likely that cloud scenes display structures over a wide range of scales.

One has to give credit to Lovejoy and co-workers [131, 133, 135, 143, 144, 254, 255, 274, 275], for applying the multifractal description to atmospheric phenomena. Using the trace moment and double trace moment techniques [133, 135, 274, 275] they have brought experimental evidence for multiple scaling (or in other words, the existence of a continuum of scaling exponent values) in various geophysical fields. More recently, Davis and co-workers [245, 256, 264] have used the structure function method to study LWC data recorded during ASTEX and FIRE programs. Both these analyses lead to the conclusion that the internal marine stratocumulus (Sc) structure is multifractal over at least three decades in scales. Similar multifractal behavior has been reported by Wiscombe *et al* [273] when analyzing liquid water path (LWP) data (i.e., column integrated LWC), from the Atmosperic Radiation Measurement (ARM) archive. Even though all these studies seem to agree, at least as far as their common diagnostic of multifractal scaling of the cloud structure is concerned, they all address 1D data. To our knowledge, the stucture function method has been also applied to 1D cuts of high-resolution satelitte images [269, 276], but we are not aware of any results coming out from a specific 2D analysis. Our goal here is to take advantage of the 2D WTMM method to carry out a multifractal analysis of high-resolution satellite images of cloudy scenes [229, 230, 233, 277]. Beyond the issue of improving statistical characterization of *in situ* and remotly sensed data, there is a most challenging aspect which consists in extracting structural information to constraint stochastic cloud models which in turn will be used for radiative transfer simulations [245, 252, 254, 269, 278–284]. Then by comparing the multifractal properties of the numerically generated artificial radiation fields with those of actual measurements, one can hope to achieve some degree of closure.

5.1   Landsat data of marine stratocumulus cloud scenes

Over the past fifteen years, Landsat imagery has provided the remote sensing community at large with a very attractive and reliable tool for studying the Earth's environment [245,

249, 251–253, 268–272, 285, 286]. One of the main advantages of high-resolution satellite imagery is its rather low effective cost as compared to outfitting and flying research aircraft. Moreover this instrument is well calibrated and it offers the possibility to reach unusual high spatial, spectral and radiometric resolutions [269, 286]. Mainly two types of statistical analysis have been applied so far to Landsat imagery: spectral analysis of the 2D radiance field [268–272, 286] and joint area and perimeter distributions for ensembles of individual clouds [249, 251–253] defined by some threshold in radiance. One of the most remarkable properties of Landsat cloud scenes is their statistical "scale-invariance" over a rather large range of scales, which justifies why fractal and multifractal concepts have progressively gained more acceptance in the atmospheric scientist community [16, 245].

Off all cloud types, *marine stratocumulus* (Sc) are without any doubt the ones which have attracted the most attention, mainly because of their first-order effect on the Earth's energy balance [16, 244, 245, 286, 287]. Being at once very persistent and horizontally extented, marine Sc layers carry considerable weight in the overall reflectance (albedo) of the planet and, from there, command a strong effect on its global climate [246]. Furthermore, with respect to climate modeling [247] and the major problem of cloud-radiation interaction [245, 254, 268, 269, 278–280, 282, 288], they are presumably at their simplest in marine Sc which are relatively thin ($\sim$ 300-500 m), with well-defined (quasi-planar) top and bottom, thus approximating the plane-parallel geometry where radiative transfer theory is well developed [244, 254, 269, 279, 280, 282]. However, because of its internal homogeneity assumption, plane-parallel theory shows systematic biases in large-scale average reflectance [280, 289] relevant to Global Circulation Model (CGM) energetics and large random errors in small-scale values [282, 290] relevant to remote-sensing applications. Indeed, marine Sc have huge internal variability [256, 264], not necessarily apparent to the remote observer (see Fig. 16a).

In the next section, we challenge previous analysis [249, 251–253, 268–272, 285, 286] of Landsat imagery using the 2D WTMM methodology [229, 230, 277] described in section 4. Our specific goal will be to improve statistical characterization of the highly intermittent radiance fluctuations of marine Sc, a prerequisite for developing better models of cloud structure. For that purpose, we analyze a ($\simeq 196 \times 168$ km^2) original cloudy Landsat 5 scene captured with the TM camera (1 pixel = 30 m) in the 0.6-0.7 μm channel (i.e. reflected solar photons as opposed to their counterparts emitted in the thermal infrared) during the first ISCCP (International Satellite Cloud Climatology Project) Research Experiment (FIRE) field program, which took place over the Pacific Ocean off San Diego in summer 1987. For computational convenience, we actually select 32 overlapping 1024×1024 pixels^2 subscenes in this cloudy region. The overall extend of the explored area is about 7840 km^2 [277]. Fig. 16a shows a typical (1024×1024) portion of the original image where the eight-bit grey scale coding of the quasi-nadir viewing radiance clearly reveals the presence of some anisotropic texture induced by convective structures which are generally aligned to the wind direction.
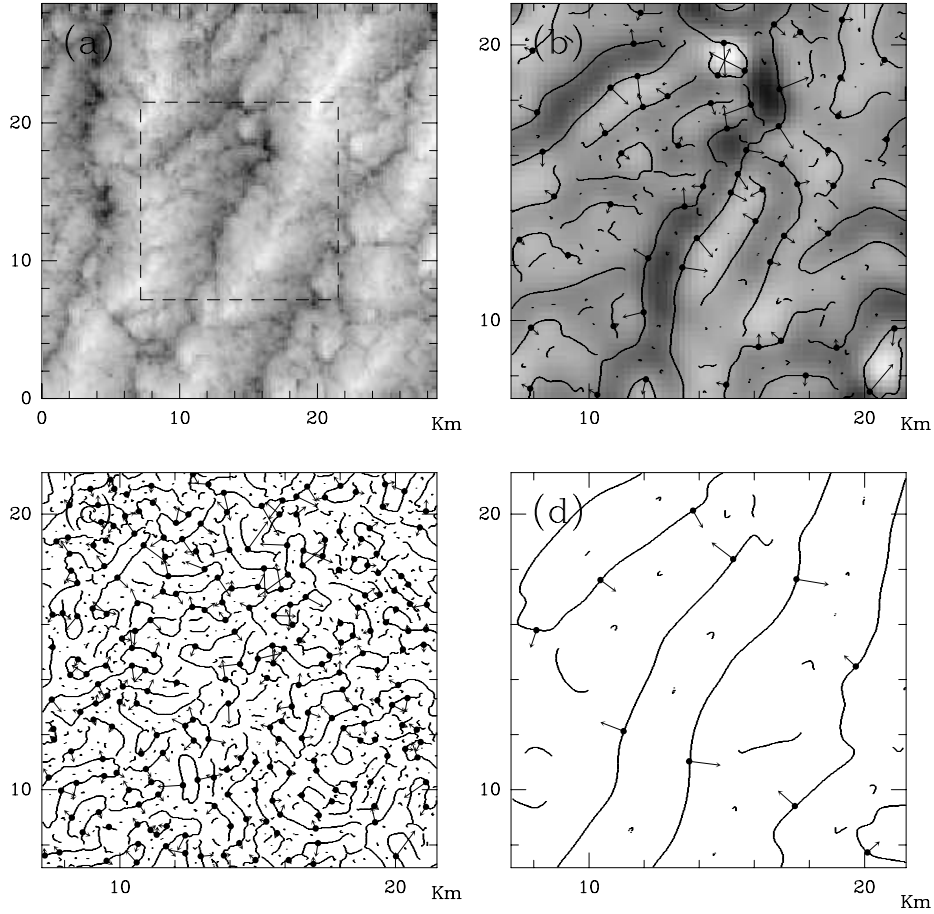

Fig. 16. 2D WT analysis of a Landsat image of marine Sc clouds captured at $l = 30m$ resolution on July 7 1987, off the coast of San Diego (CA) [265]. (a) 256 grey-scale coding of a (1024×1024) portion of the original radiance image. In (b) $a = 2^{2.9}\sigma_W$, (c) $a = 2^{1.9}\sigma_W$ and (d) $a = 2^{3.9}\sigma_W$ where $(\sigma_W = 13$ pixels $\simeq 390m)$, are shown the maxima chains; the local maxima of $\mathcal{M}_\psi$ along these chains are indicated by ($\bullet$) from which originates an arrow whose length is proportional to $\mathcal{M}_\psi$ and its direction (with respect to the x-axis) is given by $\mathcal{A}_\psi$; only the central (512×512) part delimited by a dashed square in (a) is taken into account to define the WT skeleton. In (b), the smoothed image $\phi_{\mathbf{b},a} \star I$ is shown as a grey-scale coded background from white (min) to black (max). $\psi(\mathbf{x})$ is the first-order radially symmetric analyzing wavelet shown in Fig. 11.

5.2   WTMM multifractal analysis of Landsat images of stratocumulus

We systematically follow the numerical implementation procedure previously used in section 4.4 for synthetic rough surfaces. We first wavelet transform the 32 overlapping (1024×1024) images, cut out of the original image, with the first-order $(n_\psi = 1)$ radially symmetric analyzing wavelet defined in Fig. 11. From the WT skeleton defined by the WTMMM, we compute the partition functions from which we extract the $\tau(q)$ and $D(h)$ multifractal spectra as explained in section 4.3. We systematically test the robustness of our estimates with respect to some change in the shape of the analyzing wavelet, in particular when increasing the number of zero moments.

Numerical computation of the multifractal $\tau(q)$ and $D(h)$ spectra

In Fig. 16 is illustrated the computation of the maxima chains and the WTMMM for the marine Sc sub-scene. After linking these WTMMM across scales, one constructs the WT skeleton from which one computes the partition functions $Z(q, a)$ (50). As reported in Fig. 17a, the annealed average partition functions ($\bullet$) display some well-defined scaling behavior over the first three octaves, i.e. over the range of scales 390 m $\lesssim a \lesssim$ 3120 m, when plotted versus a. Indeed the scaling deteriorates progressively from the large scale side when one goes to large values of $|q| \gtrsim 3$. As discussed in Ref. [277], besides the fact that we are suffering from insufficient sampling, the presence of localized Dirac like structures is likely to explain the fact that the observed cross-over to a steeper power-law decay occurs at a smaller and a smaller scale when one increases $q > 0$. Actually for $q \gtrsim 3$, the cross-over scale $a^* \lesssim$ 1200 m becomes significantly smaller than the so-called integral scale which is approximately given by the characteristic width $\lambda \simeq$ 5-6 km of the convective rolls (Fig. 16a). When processing to a linear regression fit of the data in Fig. 17a over the first octave and a half (in order to avoid any bias induced by the presence of the observed cross-over at large scales), one gets the $\tau(q)$ spectrum ($\bullet$) shown in Fig. 17b. In contrast to the fBm rough surfaces studied in section 4.4, this $\tau(q)$ spectrum unambiguously deviates from a straight line. When Legendre transforming this nonlinear $\tau(q)$ curve, one gets the $D(h)$ singularity spectrum reported in Fig. 17c. Its characteristic single humped shape over a finite range of Hölder exponents is a clear signature of the multifractal nature of the marine Sc radiance fluctuations.

In Fig. 17 are also shown for comparison the results ($\circ$) obtained when applying the 2D WTMM method with a third-order ($n_\psi = 3$) radially symmetric analyzing wavelet (the smoothing function ϕ being the isotropic 2D mexican hat). As seen in Fig. 17a, the use of a wavelet which has more zero moments seems to somehow improve scaling. For the range of q-values investigated, the cross-over scale turns out to be rejected at a larger scale, enlarging by some amount the range of scales over which scaling properties can be measured, especially for the largest values of $|q|$. The fact that one improves scaling when increasing the order of the analyzing wavelet suggests that perhaps some smooth behavior unfortunately deteriorates our statistical estimate of the multifractal spectra of the original Landsat radiance image. Let us recall that, as explained in section 4.2, smooth C^∞ behavior may give rise to maxima lines along which $\mathcal{M}_\psi \sim a^{n_\psi}$ (see Fig. 12); hence larger n_ψ, smaller is the overall contribution of those "spurious" maxima lines in the partition function summation over the WT skeleton. As seen in Fig. 16a, the anisotropic texture induced by the convective streets or rolls might well be at the origin of the relative lack of well defined scale invariance. When looking at the corresponding $\tau(q)$ spectrum ($\circ$) extracted from the data in Fig. 17b, one gets quantitatively the same estimates for $q \gtrsim -1$. For more negative values of q, the data obtained with the third-order analyzing wavelet clearly depart from the previous estimates with the first-order wavelet. The slope of the new $\tau(q)$ spectrum
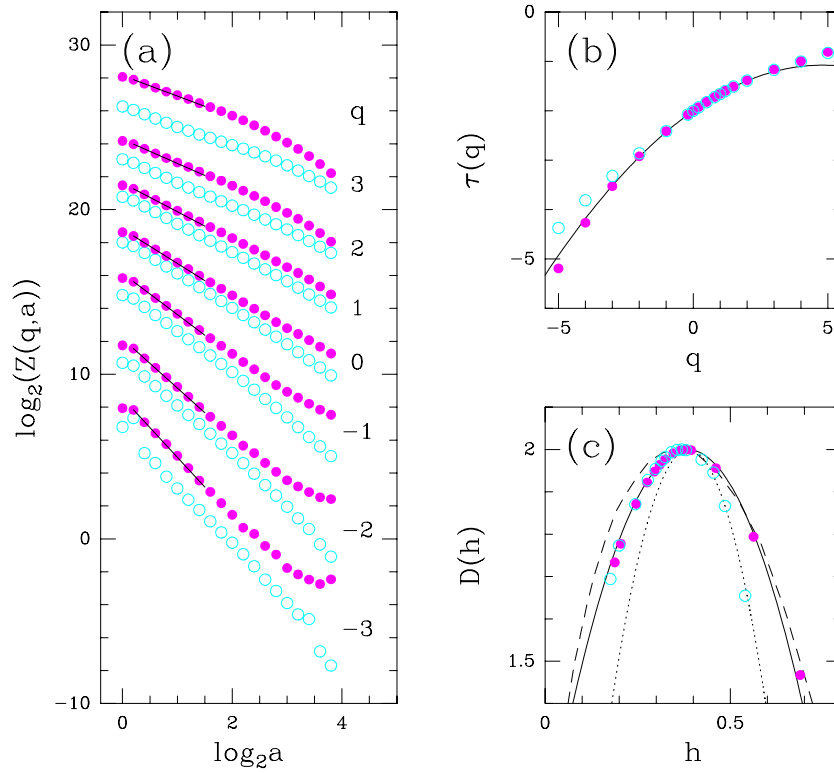
Fig. 17. Determination of the $\tau(q)$ and $D(h)$ spectra of radiance Lansat images of marine Sc. The 2D WTMM method is used with either a first-order ($\bullet$) or a third-order ($\circ$) radially symmetric analyzing wavelet (see Fig. 11). (a) $\log_2 Z(q,a)$ vs $\log_2 a$; the solid lines correspond to linear regression fits of the data over the first and a half octave. (b) $\tau(q)$ vs q obtained from a linear regression fit of the data in (a). (c) $D(h)$ vs h, after Legendre transforming the $\tau(q)$ curve in (b). In (b) and (c), the solid lines correspond to the theoretical multifractal spectra for the log-normal $\mathcal{W}$-cascades with parameter values $m = -0.38 \ln 2$ and $\sigma^2 = 0.07 \ln 2$ ((61) and (62)). The $D(h)$ singularity spectrum of velocity (dotted line) and temperature (dashed line) fluctuations in fully developed turbulence are shown for comparaison in (c).

is somehow weakened which implies, from the Legendre transform properties, that the corresponding values of $h(q) = \partial \tau / \partial q$ are reduced. The computation of the $D(h)$ singularity spectrum ($\circ$) in Fig. 17c enlightens this phenomenom: while the increasing left-hand branch (which corresponds to the strongest singularities) of the $D(h)$ curve appears to be quite robust with respect to the choise of $\boldsymbol{\psi}$, the decreasing right-hand branch (associated to the weakest singularities) is modified when increasing the number of zero moments of $\boldsymbol{\psi}$. As shown in Figs. 17b and 17c, the $\tau(q)$ spectrum as well as the $D(h)$ spectrum data, are very well fitted by the theoretical quadratic spectra of log-normal random $\mathcal{W}$-cascades (Eqs (61) and (62)). However, with the first-order analyzing wavelet, the best fit is obtained with the parameter values $m = -0.38 \ln 2 = -0.263$ and $\sigma^2 = 0.07 \ln 2 = 0.049$, while for the third-order wavelet these parameters take slightly different values, namely $m = -0.366 \ln 2 = -0.254$ and $\sigma^2 = 0.06 \ln 2 = 0.042$. The variance parameter σ^2 which characterizes the intermittent nature of marine Sc radiance fluctuations is therefore somehow reduced when going from $n_{\boldsymbol{\psi}} = 1$ to $n_{\boldsymbol{\psi}} = 3$. Actually, it is the lack of statistical convergence because

of insufficient sampling which is the main reason for this uncertainty in the estimate of σ^2 [277]. As previously experienced in Ref. [232] for synthetic multifractal rough surfaces, an accurate estimate of the exponents $\tau(q)$ for $q \lesssim -3$ requires more than 32 (1024×1024) images. With the statistical sample of Landsat images we have at our disposal, one gets $D(h(q = 0) = 0.37 \pm 0.02) = 2.00 \pm 0.01$, which is a strong indication that the radiance field is singular everywhere. From the estimate of $\tau(q = 2) = -1.38 \pm 0.02$; one gets the following estimate of the spectral exponent: $\beta = \tau(2) + 4 = 2.62 \pm 0.02$, i.e., a value which is in good agreement with previous estimates [257–261, 263, 268–272, 286].

WTMMM probability density functions

This sub-section is mainly devoted to the analysis of the joint probability distribution function $P_a(\mathcal{M}, \mathcal{A})$ (see section 4.3) as computed from the WT skeletons of the 32 (1024×1024) radiance images with the first-order radially symmetric analyzing wavelet $(n_\psi = 1)$. In Figs. 18a and 18b are respectively shown the pdf's $P_a(\mathcal{M}) = \int d\mathcal{A} \, P_a(\mathcal{M}, \mathcal{A})$ and $P_a(\mathcal{A}) = \int d\mathcal{M} \, P_a(\mathcal{M}, \mathcal{A})$, for three different values of the scale parameter $a = 2^{0.3}\sigma_W$ (480 m), $2^{1.3}\sigma_W$ (960 m) and $2^{2.3}\sigma_W$ (1920 m). First let us focus on the results shown in Fig. 18b for $P_a(\mathcal{A})$. This distribution is clearly scale dependent with some evidence of anisotropy enhancement when going from small to large scales, in particular when one reaches scales which become comparable to the characteristic width of the convective structures (i.e., a few kilometers wide). Two peaks around the values $\mathcal{A} \simeq -\pi/6$ and $5\pi/6$ become more and more pronounced as the signature of a privilegied direction in the analyzed images. As one can check from a visual inspection of Fig. 16a, this direction is nothing but the perpendicular to the mean direction of the convective rolls that are generally aligned to the wind direction. This is another clear indication that, at large scales, the WT microscope is sensitive to the convective roll texture, a rather regular modulation superimposed to the background radiance fluctuations [230, 277]. Another important message which comes out from our analysis is illustrated in Figs. 18c and 18d. When conditioning the pdf of $\mathcal{M}$ by the argument $\mathcal{A}$, the shape of this pdf is shown to be independent of the considered value of $\mathcal{A}$, as long as the value of the scale parameter a remains small as compared to the characteristic width of the convective structures. The observation that the joint probability distribution actually factorizes, i.e., satisfies (54), is the signature that $\mathcal{M}$ and $\mathcal{A}$ are likely to be independent [230, 277]. This implies that all the multifractal properties of the marine Sc radiance fluctuations are contained in the way the shape of the pdf of $\mathcal{M}$ evolves when one decreases the scale parameter a. As shown in Fig. 18a, for any scale significantly smaller than the integral scale ($\sim$ 5-6 km, as given by the characteristic width of the convective structures) all the data points fall, within a good approximation, on a log-normal curve [230, 277].
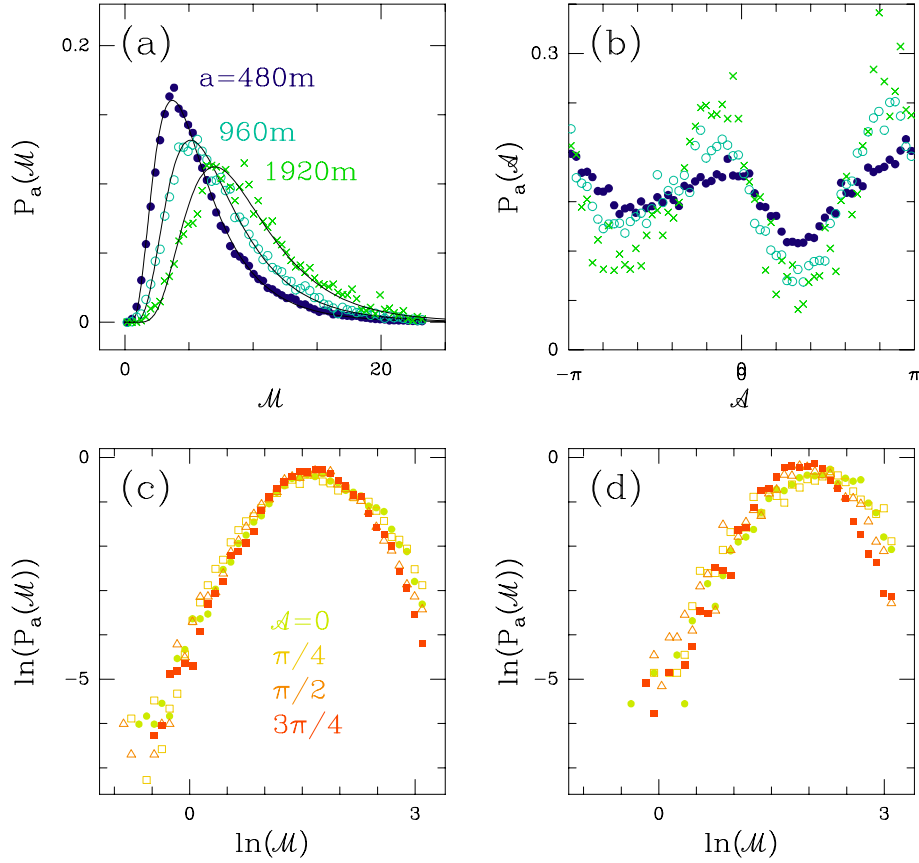
Fig. 18. Pdf's of the WTMMM coefficients of 32 (1024×1024) radiance Landsat images as computed with the first-order radially symmetric analyzing wavelet. (a) $P_a(\mathcal{M})$ vs $\mathcal{M}$; (b) $P_a(\mathcal{A})$ vs $\mathcal{A}$; the symbols correspond to the following scales $a = 2^{0.3}\sigma_W = 480$m (●), $2^{1.3}\sigma_W = 960$m (○) and $2^{2.3}\sigma_W = 1920$m (×). Pdf's of $\mathcal{M}$ when conditioned by $\mathcal{A}$ at the scales (c) $a = 2^{0.3}\sigma_W = 480$m and (d) $a = 2^{1.3}\sigma_W = 960$m. The different symbols in (c) and (d) correspond to fixing $\mathcal{A}$ (mod π) to $0 \pm \pi/8$ (○), $\pi/4 \pm \pi/8$ (□), $\pi/2 \pm \pi/8$ (△) and $3\pi/4 \pm \pi/8$ (■).

5.3   Comparative WTMM multifractal analysis of Landsat radiance field and velocity and temperature fields in fully developed turbulence

Let us point out that a similar 1D WTMM analysis of the velocity fluctuations in high Reynolds number turbulence has come to conclusions very close to those of the present study [87, 102–104, 291]. Besides the presence of rare localized Dirac like structures that witness to the probing of vorticity filaments [77, 94, 96, 102], the multifractal nature of turbulent velocity is likely to be understood in terms of a log-normal cascading process which is expected to be scale-invariant in the limit of very high Reynolds numbers [87, 291]. In Fig. 17c are shown for comparison the results obtained for the $D(h)$ singularity spectrum of the radiance Landsat images together with the $D(h)$ data extracted from the 1D analysis of a turbulent velocity signal recorded at the Modane wind tunnel ($R_\lambda \simeq 2000$) [87, 104] (indeed $D(h) + 1$ is represented for the latter in order to compare 1D to 2D data). The turbulent velocity $D(h)$ spectrum significantly differs from the results obtained for the marine Sc cloud. They have a common feature, i.e., the Hölder exponent the most frequently

encountered in the radiance field $h = m/\ln 2 = h(q = 0) = \partial\tau/\partial q|_{q=0} = 0.38 \pm 0.01$ is undistinguishable from the corresponding exponent $h = h(q = 0) = 0.39 \pm 0.01$ found for the turbulent velocity field. Note that these values are significantly larger than the theoretical value $h = 1/3$ predicted by Kolmogorov in 1941 [128] to account for the observed $k^{-5/3}$ power-spectrum behavior. The main difference comes from the intermittency parameter which is much stronger for the cloud, $\sigma^2/\ln 2 = 0.07\pm0.01$ ($n_\psi = 1$) or $\sigma^2/\ln 2 = 0.06\pm0.01$ ($n_\psi = 3$) than for the turbulent velocity, $\sigma^2/\ln 2 = 0.036\pm0.004$. This is the signature that the radiance field is much more intermittent than the velocity field: the $D(h)$ singularity spectrum for the former is unambiguously wider than the corresponding spectrum for the later. For the sake of comparison, we have also reported in Fig. 17c, the multifractal $D(h)$ spectrum of the temperature fluctuations recorded in a $R_\lambda = 400$ turbulent flow [292]. The corresponding single humped curve is definitely much wider than the velocity $D(h)$ spectrum and it is rather close to the data corresponding to the marine Sc radiance field. It is well recognized however that liquid water is not really passive and that its identification with a passive component in atmospheric dynamics offers limited insight into cloud structure since, by definition, near-saturation conditions prevail and latent heat production affects buoyancy [293]. So cloud microphysical processes are expected to interact with the circulation at some, if not all, scales [294]. Nevertheless, our results in Fig. 17c tell us that from a multifractal point of view, the intermittency captured by the Landsat satellite looks statistically equivalent to the intermittency of a passive scalar in fully-developed 3D turbulence. The fact that the internal structure of Sc cloud somehow reflects some statistical properties of atmospheric turbulence is not such a surprise in this highly turbulent environment. The investigation of different sets of Landsat data is urgently required in order to test the degree of generality of the results reported in this first WTMM analysis of high-resolution satellite images. In particular, one may wonder up to which extend the marine Sc Landsat data collected off the coast of San Diego on July 7, 1987 under specific observation conditions, actually reflect the specific internal structure of Sc clouds. Work in this direction is currently in progress.

Finally, with respect to the issue of cloud modeling, it comes out quite naturally from the WTMM analysis of marine Sc Landsat data, that the 2D random $\mathcal{W}$-cascade models introduced in Refs. [232, 233], are much more realistic hierarchical models than commonly used multifractal models like the fractionally integrated singular cascade [133, 135, 274] or the bounded cascade [287, 295] models. We are quite optimistic in view of using the log-normal $\mathcal{W}$-cascade models with realistic parameter values for radiation transfer simulations. To our opinion, random $\mathcal{W}$-cascade models are a real breakthrough, not only for the general purpose of image synthesis, but more specifically for cloud modeling. It is likely that better cloud modeling will make further progress in our understanding of cloud-radiation interaction possible.

6   Beyond multifractal analysis with wavelet-based space-scale correlations functions: revealing a causal information cascade in stock market data

6.1   Space-scale correlation functions from wavelet analysis

Correlations in multifractals have already been experienced in the literature [296–298]. However, all these studies rely upon the computation of the scaling behavior of some partition functions involving different points; they thus mainly concentrate on spatial correlations of the local singularity exponents. The approach developed in Ref. [86] is different since it does not focus on (nor suppose) any scaling property but rather consists in studying the correlations of the *logarithms* of the amplitude of a space-scale decomposition of the signal. For that purpose, the WT is a natural tool to perform space-scale analysis. More specifically, if $\chi(x)$ is a bump function such that $||\chi||_1 = 1$, then by taking

$$\varepsilon(x,a) = a^{-2} \int \chi((x-y)/a)|T_\psi[f](y,a)|^2 dy, \tag{63}$$

one has:

$$||f||_2^2 = \int\int \varepsilon(x,a)dx\,da , \tag{64}$$

and thus $\varepsilon(x,a)$ can be interpreted as the *local space-scale energy density* of the considered signal f [299]. Since $\varepsilon(x,a)$ is a positive quantity, we can define the *magnitude* of the field f at point x and scale a as:

$$\omega(x,a) = \frac{1}{2}\ln\varepsilon(x,a) . \tag{65}$$

Our aim in this section, is to show that a cascade process can be studied through the correlations of its space-scale magnitudes [86]:

$$C(x_1,x_2,a_1,a_2) = \overline{\tilde{\omega}(x_1,a_1)\tilde{\omega}(x_2,a_2)} , \tag{66}$$

where the overline stands for ensemble average and $\tilde{\omega}$ for the centered process $\omega - \overline{\omega}$.

6.2   Analysis of random $\mathcal{W}$-cascades using space-scale correlation functions

As discussed in section 2.6, cascade processes can be defined in various ways. Periodic wavelet orthogonal bases [70, 73] provide a general framework in which $\mathcal{W}$-cascades can be constructed easily [102–106]. Let us consider the following wavelet series:

$$f(x) = \sum_{j=0}^{+\infty}\sum_{k=0}^{2^j-1} c_{j,k}\psi_{j,k}(x) , \tag{67}$$

where the set $\{\psi_{j,k}(x) = 2^{j/2}\psi(2^j x - k)\}$ is an orthonormal basis of $L^2([0, L])$ and the coefficients $c_{j,k}$ correspond to the WT of f at scale $a = L2^{-j}$ (L is the "integral" scale that corresponds to the size of the support of $\psi(x)$) and position $x = ka$. The above sampling of the space-scale half-plane defines a dyadic tree [70, 73]. If one indexes by a dyadic sequence $\{\epsilon_1....\epsilon_j\}$ ($\epsilon_k = 0$ or 1) each of the 2^j nodes at depth j of this tree, the cascade is defined by the multiplicative rule: $c_{j,k} = c_{\epsilon_1...\epsilon_j} = c_0 \prod_{i=1}^{j} W_{\epsilon_i}$. The law chosen for the weights W determines the nature of the cascade and the multifractal (regularity) properties of f [105, 106]. From the above multiplicative structure (Fig. 19), if one assumes that there is no correlation between the weights at a given cascade step, then it is easy to show that for $a_p = L2^{-j_p}$ and $x_p = k_p a_p$ ($p = 1$ or 2), the correlation function (66) is nothing but the variance $V(j)$ of $\ln c_{j,k} = \sum \ln W_{\epsilon_i}$, where (j, k) is the deepest common ancestor to the nodes (j_1, k_1) and (j_2, k_2) on the dyadic tree [86, 105]. This *ultrametric* structure of the correlation function shows that such a process is not stationary. However, we will generally consider uncorrelated consecutive realizations of length L of the same cascade process, so that, in good approximation, C depends only on the space lag $\Delta x = x_2 - x_1$ and one can replace ensemble average by space average. In that case, $C(\Delta k, j_1, j_2) = \langle C(k_1, k_1 + \Delta k, j_1, j_2)\rangle$ can be expressed as [86, 105]:

$$C(\Delta k, j_1, j_2) = 2^{-(j-n)} \sum_{p=1}^{j-n} 2^{j-n-p} V(j - n - p) , \qquad (68)$$

where $j = \sup(j_1, j_2)$ and $n = \log_2 \Delta k$.

Let us illustrate these features on some simple case of random $\mathcal{W}$-cascades (*e.g.* log-normal cascades) [102–106]. As in classical cascades, at each step of the cascade, on chooses i.i.d. random variables $\ln W_{\epsilon_i}$ of variance σ^2. Then $V(j) = \sigma^2 j$ and it can be established [86, 105] that, for $\sup(a_1, a_2) \leq \Delta x < L$,

$$C(\Delta x, a_1, a_2) = \sigma^2 \left(\log_2(\frac{L}{\Delta x}) - 2 + 2\frac{\Delta x}{L} \right) . \qquad (69)$$

Thus, the correlation function decreases very slowly, independently of a_1 and a_2, as a *logarithm function* of Δx. This behavior is illustrated in Figs 21a and 21b where a log-normal cascade (Fig. 20a) has been constructed using Daubechies compactly supported wavelet basis (D-5) [73]. The correlation functions of the magnitudes of $f(x)$ have been computed as described above (66) using a simple box function for $\chi(x)$. Let us note that all the results reported in this section concern the increments (we use $\psi_{(0)}^{(1)}$) of the considered signal and that we have checked that they are actually independent of the specific choice of the analyzing wavelet $\psi_{(m)}^{(n)}$ (Fig. 2). In Fig. 21a are plotted the "one-scale" ($a_1 = a_2 = a$) correlation functions for three different scales $a = 4$, 8 and 32. One can see that, for $\Delta x > a$, all the curves collapse to a single one, which is in perfect agreement with the expression (69): in semi-log-coordinates, the correlation functions decrease almost linearly (with slope σ^2) up to the integral scale L that is of order 2^{16} points. In Fig. 21b are displayed these correlation functions when the two scales a_1 and a_2 are different. One can
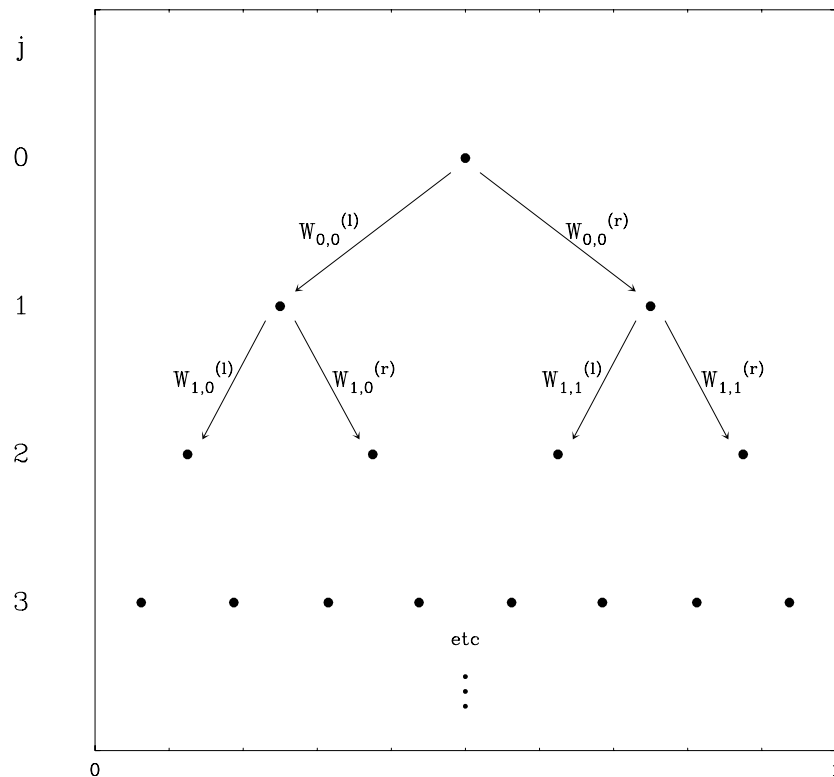
Fig. 19. Sketch of the construction rule of a $\mathcal{W}$-cascade. The wavelet coefficients $\{c_{j,k}\}_{j,k}$ lie on a dyadic grid. At each scale $a_j = 2^{-j}$, the grid displays 2^j coefficients with abscissa $x_{j,k} = 2^{-j}k$. The value of the wavelet coefficient $c_{j,2k}$ (resp. $c_{j,2k+1}$) is obtained from the value of the wavelet coefficient $c_{j-1,k}$ by multiplying it by $W_{j-1,k}^{(l)}$ (resp. $W_{j-1,k}^{(r)}$) where $W_{j-1,k}^{(\epsilon)}$ are i.i.d. real valued random variables.

check that, as expected, they still do not depend on the scales provided $\Delta x \geq \sup(a_1, a_2)$; moreover they are again very well fitted by the above theoretical curve (except at very large Δx where finite size effects show up). The linear behavior of $C(\Delta x, a_1, a_2)$ vs $\ln(\Delta x)$ is characteristic for "classical" scale-invariant cascades for which the random weights are uncorrelated [86, 87, 105].

6.3   Distinguishing "multiplicative" from "additive" processes

The two previous examples illustrate the fact that magnitudes in random cascades are correlated over very long distances. Moreover, the slow decay of the correlation functions is independent of scales for large enough space lags ($\Delta x > a$). This is reminiscent of the multiplicative structure along a space-scale tree. These features are not observed in "additive" models like fBm's (section 2.6) whose long-range correlations originate from the sign of their variations rather than from the amplitudes. In Figs 21a and 21b are plotted the correlation functions of an "uncorrelated" log-normal model constructed using the same parameters as in the first example but without any multiplicative structure (the coefficients $c_{j,k}$ have, at each scale j, the same log-normal law as before but are independent). Let us
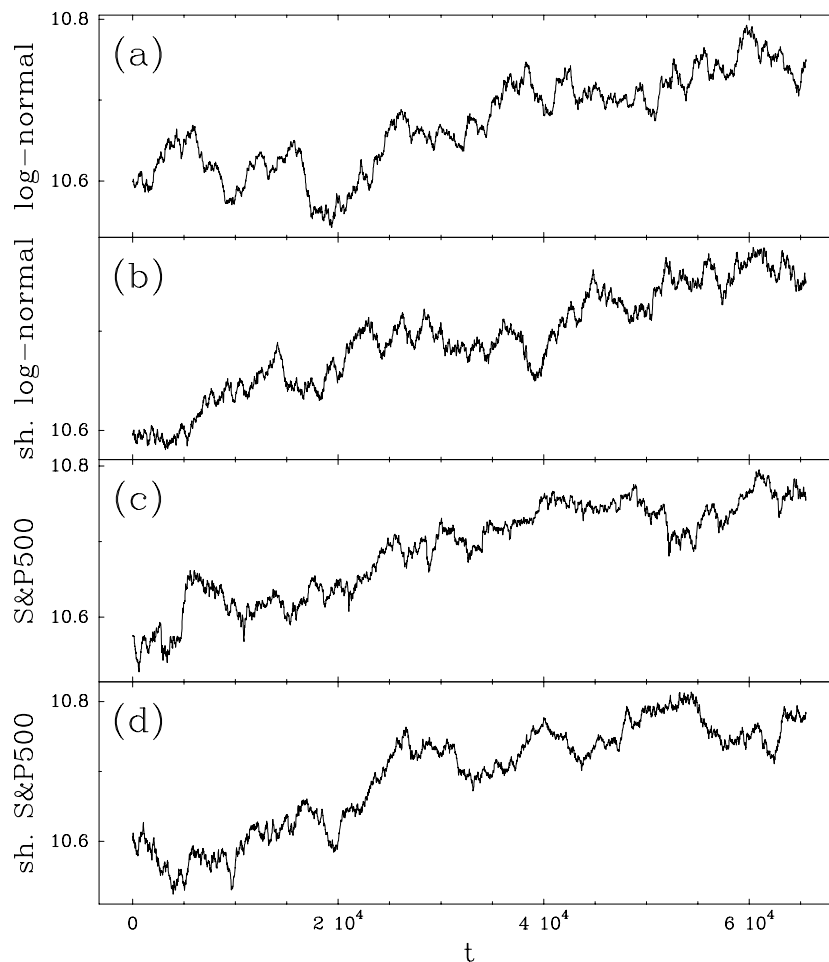
Fig. 20. Financial time-series as compared to synthetic multifractal signals: (a) Realization of a random function generated by a log-normal $\mathcal{W}$-cascade using the "Daubechies 5" compactly supported orthogonal wavelet basis. The law of $\ln|W|$ is Gaussian with mean $m = -H\ln 2 = -0.6\ln 2$ and variance $\sigma^2 = 0.02\ln 2 = 0.0077$. (b) "White noise" version of the log-normal $\mathcal{W}$-cascade realization shown in (a) after randomly shuffling the wavelet coefficients at each scale j. (c) Time evolution of $\ln P(t)$, where $P(t)$ is the S&P 500 index, sampled with a time resolution $\delta t = 5$ min in the period October 1991 – February 1995. The data have been preprocessed in order to remove "parasitic" daily oscillatory effects. (d) Same as in (c) but after having randomly shuffled the increments of the signal in (c).

note that from the point of view of both the multifractal formalism and the increment pdf scale properties, the "uncorrelated" (Fig. 20b) and "multiplicative" (Fig. 20a) log-normal models are undistinguishable since their one-point statistics at a given scale are identical. As far as the magnitude space-scale correlations are concerned, the difference between the cascade and the other models is striking: for $\Delta x > a$, the magnitudes of the "white noise" log-normal model are found to be uncorrelated. Let us emphasize that similar uncorrelated behavior is observed for fBm's and Levy processes [86, 105]. For their ability to reveal the existence of a multiplicative hierarchical structure underlying fractal landscapes or
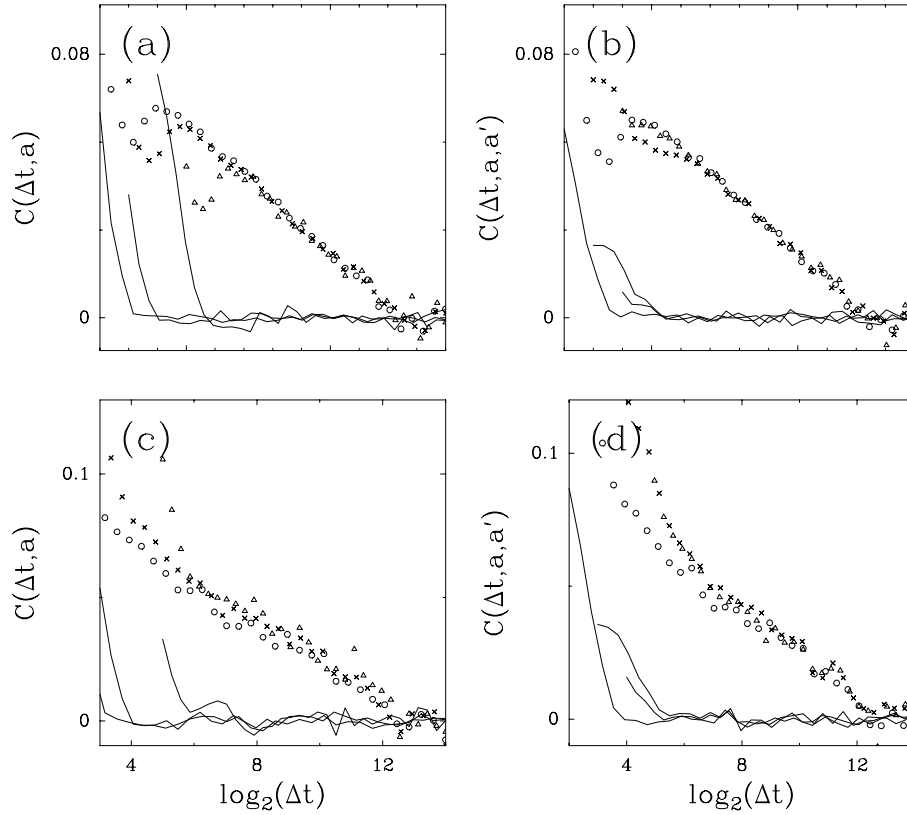
Fig. 21. Space-scale correlation functions $C(t, t + \Delta t, a, a')$. *Log-normal random $\mathcal{W}$-cascade:* (a) "one-scale" correlation functions ($a = a'$) for $a = 4$ (○), 8 (×) and 32 (△); (b) "two-scale" correlation functions for $a = 4$, $a' = 8$ (○), $a = 8$, $a' = 32$ (×) and $a = 4$, $a' = 32$ (△); the solid curves correspond to similar computations performed on the "white noise" log-normal $\mathcal{W}$-cascade realizations. *S&P 500 index:* (c) "one-scale" correlation functions of the log-volatility for various scales a corresponding to $a = 30$ (○), 120 (×) and 480 (△) minutes; (d) "two-scale" correlation functions for various pairs of scales corresponding to $a = 30$, $a' = 120$ (○), $a = 120$, $a' = 480$ (×) and $a = 30$, $a' = 480$ (△) in mn units; the solid curves correspond to similar computations performed on the randomly shuffled increment version of the S&P 500 index.

turbulent signals, the wavelet-based space-scale correlation functions are a definite step beyond statistical multifractal analysis [86, 105].

6.4   Analysis of stock market data using space-scale correlations

Modelling accurately financial price variations is an essential step underlying portfolio allocation optimization, derivative pricing and hedging, fund management and trading [19, 20, 300–302]. The observed complex price fluctuations guide and constraint our theoretical understanding of agent interactions and of the organization of the market. The gaussian paradigm of independent normally distributed price increments [303, 304] has long been known to be incorrect with many attempts to improve it. Mandelbrot first proposed to use Lévy distributions [23, 305], which are characterized by a fat tail decaying as a power law with index between 0 and 2. His suggestion arrived at an epoch when Markovitz famous mean-variance portfolio and Black-Scholes option pricing theories were being developed

and widely applied. For main stream economists, the econometric nonlinear autoregressive models with conditional heteroskedasticity (ARCH) [306] and their generalizations [307] are more natural because they keep the volatility (standard deviation of price variations) as the main descriptor. Recall that heteroskedasticity refers to the fact that the variance (or volatility) is itself a stochastic variable (The exact definition is the following: when the errors for different dates (or points) have different variances but are unrelated with each other, then the errors are said to exhibit heteroskedasticity. If the variances are related, the heteroskedasticity is said to be correlated). These models address volatility clustering and partly the observed "fat tails" of distributions. The problem however is that these GARCH models capture only imperfectly the volatility correlations and the fat tails of the probability density function (pdf) of price variations. Moreover, as far as changes in time scales are concerned, the so-called "aggregation" properties of these models are not easy to control.

Recently, physicists have characterized more precisely the distribution of market price variations [19, 20] and found that a power law truncated by an exponential provides a reasonable fit at short time scales (less than one day), while at larger time scales the distributions may cross over progressively to the Gaussian distribution which becomes approximately correct for monthly and larger scale price variations [19, 20, 152, 308]. Alternatively, Ghashghaie et $al.$ [309] proposed a "multiplicative" cascade model based on an analogy between price dynamics and hydrodynamic turbulence. According to this model, the return r at a given time scale $a < T$, is given by:

$$r_a(t) \equiv \ln P(t+a) - \ln P(t) = \varepsilon(t,a)^{1/2} u(t) \ , \tag{70}$$

where $u(t)$ is some scale independent random variable, T is some coarse "integral" time scale and $\varepsilon(t,a)^{1/2}$ is the local r.m.s. of the return that can be multiplicatively decomposed, for any decreasing sequence of scales $\{a_i\}_{i=0,..,n}$ with $a_0 = T$ and $a_n = a$, as [87, 102–105, 139, 310–312]

$$\varepsilon(t,a)^{1/2} = \prod_{i=0}^{n-1} W_{a_{i+1},a_i} \varepsilon(t,T)^{1/2} \ . \tag{71}$$

Equation (70) together with (71) show that the logarithm of the price is a multiplicative process. But, this is different from the classical multiplicative processes studied in finance literature, due to the tree-like structure of the correlations that are added by the hierarchical construction of the multiplicands as discussed in section 6.2.

In turbulence the field ε is related to the energy while in finance ε is called the $volatility$. Recall that the volatility has fundamental importance in finance since it provides a measure of the amplitude of price fluctuations, hence of the market risk. Using $\omega(t,a) = \frac{1}{2}\ln \varepsilon(t,a)$ as a natural variable, if one supposes that W_{a_{i+1},a_i} depends only on the scale ratio a_{i+1}/a_i, one can easily show, by choosing the a_i as a geometric series Ts^i $(s < 1)$, that (71) implies that the pdf of ω at scale $a = Ts^n$ can be written as:

$$P_a(\omega) = (G_s^{\otimes n} \otimes P_T)(\omega) \ , \tag{72}$$

where $\otimes$ means the convolution product, G_s is the pdf of $\ln W_{sa,a}$ and P_T is the pdf of $\omega(t,T)$. The symbol $G_s^{\otimes n} \otimes P_T$ means that G_s has been convoluted with itself n times before being convoluted with P_T. Equation (72) is the exact reformulation (in log variables) of the paradigm that Ghashghaie *et al.* [309] used to fit foreign exchange (FX) rate data at different scales. Recall that it simply means that the distributions of the logarithm of the *absolute value* of the price variations can be represented by a superposition of elementary laws G_s. In this formalism, G can be proven to be the pdf of an infinitely divisible random variable [102–105, 139, 310] (hence ε is called "log-infinitely divisible"). In Ref. [309], G is assumed to be normal (the cascade is called "log-normal") of variance $-\sigma^2 \ln s$.

Note that a cascade model does not necessarily imply the existence of correlations between returns. As pointed out in Remark 1, if the exponent $\tau(2) = 0$, then the power spectral density behaves as $1/k^2$, *i.e.* as the power spectral density of Brownian motions. This is why the $1/k^2$ shape of the power spectrum of financial time series cannot be invoked as an argument against a cascade model [152, 313]. Moreover, as far as scaling properties of price fluctuations are concerned, it is easy to deduce from (72) that, if $H \ln s$ is the mean of G_s and $-\sigma^2 \ln s$ its variance, then the maximum of the pdf of $\varepsilon(t,a)^{1/2}$ varies as $a^{H-\sigma^2/2}$ (H plays the same role as the Lévy index in TLF models [19, 20, 308] with $H = 1/\mu$), while its standard deviation behaves as $a^{(H-\sigma^2)/2}$. These features are observed in both turbulence ($H \simeq 0.38$ and $\sigma^2 \simeq 0.03$) [87, 102–105, 310–312] and finance ($H \simeq 0.6$ and $\sigma^2 \simeq 0.02$) [309]. Therefore, as advocated in Ref. [309], (72) accounts reasonably well for one-point statistical properties of financial times series. However, because of the relatively small statistics available in finance, it is very difficult to demonstrate that (72) is more pertinent to fit the data than a "truncated Lévy" distribution [19, 20, 152, 308, 313].

At this point, let us emphasize that (71) imposes much more constraints on the statistics than (72) that only refers to one point statistics. The main difference between the *multiplicative* cascade model and the truncated Lévy *additive* model is that the former predicts strong correlations in the volatility while the latter assumes no correlation. It is then tempting to compute the correlations of the log-volatility $\omega(t,a)$ at different time scales a [314]. In Fig. 20 are shown time series for which we study increment time correlations (i.e. the WT coefficient correlation as computed with the analyzing wavelet $\psi_{(0)}^{(1)}$ shown in Fig. 2). Figure 20c represents the logarithm of the S&P 500 index. Figure 20d is the same as Fig. 20c but after having randomly shuffled the increments $\ln P(i+1) - \ln P(i)$. In Figs 21c and 21d are reported the one-scale and two-scale correlation functions $C^\omega(\Delta t, a_1, a_2) = \overline{\tilde{\omega}(t,a_1)\tilde{\omega}(t+\Delta t, a_2)}$ of the log-volatility as functions of $\ln \Delta t$. As compared to the absence of correlation found for the randomly shuffled S&P 500 signal, the S&P 500 index log-volatility clearly displays correlations that are well fitted by an equation analogous to (69):

$$C^\omega(\Delta t, a_1, a_2) = \sigma^2 \left(\log_2(\frac{T}{\Delta t}) - 2 + 2\frac{\Delta t}{T} \right) + \sigma_T^2 , \tag{73}$$

provided $\sup(a_1, a_2) \leq \Delta t < T$, where σ_T^2 is the variance of $\omega(t,T)$. One actually observes in Fig. 21c a slow linear decay of the one-scale correlation coefficient with a slope $\sigma^2 \simeq$

0.0077 (a value which can be obtained independently from the fit of the pdf's), with only one adjustable parameter $T \simeq 3$ months. Similar results are obtained on the two-scale correlation functions in Fig. 21d. As expected from (73), all the data collapse on a single curve which is nearly linear up to some integral time T of order 3 months, provided $\Delta t > \sup(a_1, a_2)$.

Let us point out that volatility at large time intervals that cascades to smaller scales cannot do so instantaneously. From causality properties of financial signals, the "infrared" towards "ultraviolet" cascade must manifest itself in a time asymmetry of the cross-correlation coefficients $\rho_a^\omega(\Delta t, \Delta a) = C^\omega(\Delta t, a, a + \Delta a)/\sqrt{C^\omega(0, a)C^\omega(0, a + \Delta a)}$. In particular, one expects that $\rho_a^\omega(\Delta t, \Delta a) \leq \rho_a^\omega(-\Delta t, \Delta a)$ if $\Delta t > 0$ and $\Delta a > 0$. From the observed nearly Gaussian properties of $\omega(t, a)$ [314], one can derive the following expression for the mean mutual information of the variables $\omega(t, a)$ and $\omega(t + \Delta t, a + \Delta a)$:

$$I_a(\Delta t, \Delta a) = -0.5 \log_2 \left(1 - (\rho_a^\omega(\Delta t, \Delta a))^2 \right) \ . \tag{74}$$

Since the process is causal, this quantity can be interpreted as the information contained in $\omega(t, a)$ that "propagates" to $\omega(t + \Delta t, a + \Delta a)$. In Fig. 22, we have computed $I_a(\Delta t, \Delta a)$ for the S&P500 index (Fig. 22c) and its randomly shuffled version (Fig. 22d) [314]. One can see on the bottom right picture that there is no well defined structure that emerges from the noisy background. Except in a small domain at small scales around $\Delta t = 0$, the mutual information is in the noise level as expected for uncorrelated variables. In contrast, two features are clearly visible on the bottom left representation. First, the mutual information at different scales is mostly important for equal times. This is not so surprising since there are strong localized structures in the signal that are "coherent" over a wide range of scales. The extraordinary new fact is the appearance of a non symmetric propagation cone of information showing that the volatility a large scales influences causally (in the future) the volatility at shorter scales. Although one can also detect some information that propagates from past fine to future coarse scales, it is clear that this phenomenon is weaker than past coarse/future fine flux. As compared to the symetric cone structure observed in Fig. 22a for log-normal random $\mathcal{W}$-cascades, the dissymetry observed in Fig. 22c in the mutual information of the S&P 500 index is thus a clear demonstration of the pertinence of the notion of causal cascade in market dynamics. Let us point out that similar feature are found on FX rates and other stock market data.

There are several mechanisms that can be invoked to rationalize our observations, such as the heterogeneity of traders and their different time horizon [315] leading to an "information" cascade from large time scales to short time scales, the lag between stock market fluctuations and long-run movements in dividends [316], the effect of the regular release (monthly, quarterly) of major economic indicators which cascades to fine time scale. Correlations of the volatility have been known for a while and have been partially modelled by mixtures of distributions [317], ARCH/GARCH models [306] and their extensions [307]. However, as previously pointed out, because they are constructed to fit the fluctuations at a given time interval, these models are not adapted to account for the above described multi-scale properties of financial time series. We have performed the same correlation
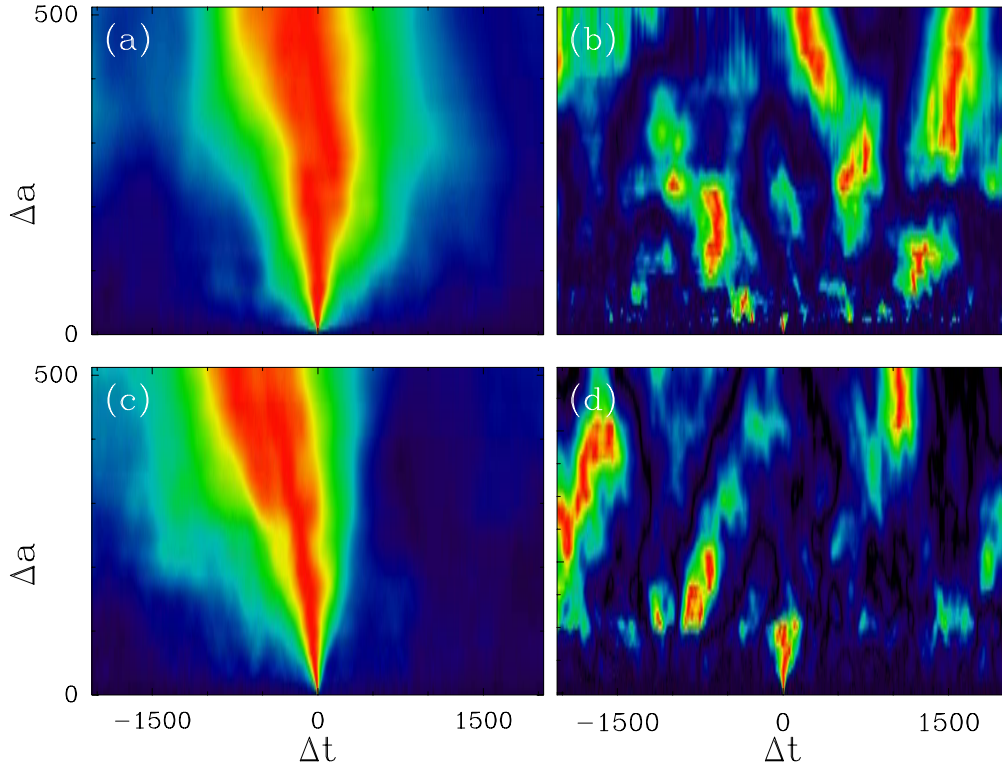
Fig. 22. *The mutual information $I_a(\Delta t, \Delta a)$ of the variables $\omega(t,a)$ and $\omega(t + \Delta t, a + \Delta a)$ is represented in the $(\Delta t, \Delta a)$ half-plane. The small scale $a = 4$ is fixed. The amplitude of $I_a(\Delta t, \Delta a)$ is coded from black for zero values to red for maximum positive values ("heat code"), independently at each scale lag Δa. (a) Log-normal random $\mathcal{W}$-cascade; same parameters values as in Fig. 20a; (b) "white noise" version of the log-normal $\mathcal{W}$-cascade; (c) S&P 500 index; (d) randomly shuffled increment version of the S&P 500. Note that, for middle scale lag values the maxima (red spots) of the mutual information in (a) and (c) are 2 orders of magnitude larger than the corresponding maxima in (b) and (d) respectively. For the S&P 500, $\Delta a = 1$ correspond to 5 minutes.*

analysis for simulated GARCH(1,1) processes and obtained structureless pictures similar to the one corresponding to the shuffled S&P500 in Fig. 22d. More recently, Muller *et al.* [315] have proposed the HARCH model in which the variance at time t is a function of the realized variances at different scales. By construction, this model captures the lagged correlation of the volatility from the large to the small time scales. However, it does not contain the notion of cascade and involves only a few time scales. Moreover, it suffers from the same defficiencies as ARCH-type models concerning the difficulties to control and interpret parameters at different scales. Let us also mention some recent work by Mandelbrot *et al.* [318] that introduces and tests a multifractal model of asset prices. Their key idea is to construct a subordinated Brownian motion using a multifractal trading time. From simple arguments, one can show that there are strong similarities with the cascade model approach advocated in this section.

Putting together the evidence provided by the logarithmic decay of the log-volatility correlations and the volatility cascade from the infrared to the ultraviolet, we have revisited the analogy with turbulence, albeit on the *volatility* and not on the price variations. Our

main finding is the exhibition of this information cascading process: the fact that variations of prices over a few month scale influence in the future the daily price variations is extraordinarily rich of consequences. This is not so only for the fundamental understanding of the nature of financial markets but also, and maybe more important, for practical applications. Indeed, the nature of the correlations that are implied by this cascade across scales, has profound implications on the market risk, a problem of upmost concern for all financial institutions as well as individuals. In particular, these correlations are likely to have strong consequences on derivative pricing and hedging.

7   Conclusion

To summarize, we have presented a first step towards a statistical theory of multifractal 1D and 2D signals based on wavelet analysis. Indeed we believe that the WTMM method (and its generalization to 2D), for determining the $D(h)$ singularity spectrum of a fractal landscape, a turbulent signal or the image of a fractal object, is likely to become as useful as the well-known phase portrait reconstruction, Poincaré section and first return map techniques for the analysis of chaotic time series [319, 320]. The reported results of previous analysis of DNA walks (section 3) and satellite images of fractal clouds (section 5), together with former wavelet-based statistical studies of fully developed turbulent velocity signals [32, 35, 36, 94, 102–104, 150, 291] as well as stock market data [151, 152], show that this method is readily applicable to experimental situations. We have also shown that one can further use the WT to go beyond this thermodynamic description of fractal objects and eventually to reveal from the branching structure of the WT skeleton, the existence of an underlying multiplicative hierarchical structure. As explained in Refs. [32, 36, 156, 321], in some situations, one can hope solving the "inverse fractal problem" by extracting from the data some dynamical system which accounts for its internal self-similar structure. The application of a wavelet-based tree matching algorithm to characterize the fractal properties of DLA azimutal Cantor sets in Refs. [154–157] has revealed the existence of a predominant Fibonacci multiplicative process in the apparently disordered arborescent morphology of diffusion-limited aggregates. This discovery is a spectacular manifestation of the statistical relevance of the golden mean arithmetic to Laplacian growth phenomena. As shown in section 6, in some situations, the use of the space-scale correlation functions computed from the WT representation can provide deep insight on the underlying random cascade structure [86]. Recent applications of this methodology in the context of fully developed turbulence have revealed the existence of a (non scale-invariant) log-normal cascading process underlying the turbulent velocity fluctuations [86, 87, 102–104, 150, 291]. More surprising are the results reported in section 6, of a similar investigation of financial time series [314]. Underlying the fluctuations of the volatility of the price variations, there exists a causal information cascade from large to small time scales that can be visualized with the WT representation. We are convinced that further applications of this wavelet based methodology (WTMM method, wavelet based tree matching algorithm for solving the inverse fractal problem, space-scale correlation functions) will lead to similar major

breakthroughs in various fields where multi-scale phenomena are ubiquitous.

Acknowledgments

References

1. B. B. Mandelbrot, *The Fractal Geometry of Nature* (Freeman, San Francisco, 1982).
2. *On Growth and Form : Fractal and Non-Fractal Patterns in Physics*, edited by H. E. Stanley and N. Ostrowski (Martinus Nijhof, Dordrecht, 1986).
3. *Fractals in Physics*, edited by L. Pietronero and E. Tosatti (North-Holland, Amsterdam, 1986).
4. *Random Fluctuations and Pattern Growth*, edited by H. E. Stanley and N. Ostrowski (Kluwer Academic, Dordrecht, 1988).
5. J. Feder, *Fractals* (Pergamon, New York, 1988).
6. T. Vicsek, *Fractal Growth Phenomena* (World Scientific, Singapore, 1989).
7. *The Fractal Approach to Heterogeneous Chemistry : Surfaces, Colloids, Polymers*, edited by D. Avnir (John Wiley and Sons, New York, 1989).
8. *Fractals in Physics, Essays in honour of B.B. Mandelbrot, Physica D, Vol. 38*, edited by A. Aharony and J. Feder (North-Holland, Amsterdam, 1989).
9. B. J. West, *Fractal Physiology and Chaos in Medecine* (World Scientific, Singapore, 1990).
10. F. Family and T. Vicsek, *Dynamics of Fractal Surfaces* (World Scientific, Singapore, 1991).
11. *Fractals and Disordered Systems*, edited by A. Bunde and S. Havlin (Springer Verlag, Berlin, 1991).
12. *Fractal in Natural Science*, edited by T. Vicsek, M. Schlesinger, and M. Matsushita (World Scientific, Singapore, 1994).
13. *Fractals in Science*, edited by A. Bunde and S. Havlin (Springer Verlag, Berlin, 1994).
14. B. J. West and W. Deering, Phys. Rep. **254**, 1 (1994).
15. U. Frisch, *Turbulence* (Cambridge Univ. Press, Cambridge, 1995).
16. *Fractals in Geoscience and Remote Sensing, Image Understanding Research Series, vol.1, ECSC-EC-EAEC*, edited by G. G. Wilkinson, J. Kanellopoulos, and J. Megier (Brussels, Luxemburg, 1995).
17. A. L. Barabási and H. E. Stanley, *Fractal Concepts in Surface Growth* (Cambridge Univ. Press, Cambridge, 1995).
18. *Fractal Aspects of Materials, Material Research Society Symposium Proceeding, Vol. 367*, edited by F. Family, P. Meakin, B. Sapoval, and R. Wool (MRS, Pittsburg, 1995).
19. J.-P. Bouchaud and M. Potters, *Théorie des Risques Financiers* (Eyrolles, Aléa-Saclay, 1997).
20. R. N. Mantegna and H. E. Stanley, *An Introduction to Econophysics* (Cambridge Univ. Press, Cambridge, 2000).
21. B. B. Mandelbrot and J. W. Van Ness, S.I.A.M. Rev. **10**, 422 (1968).
22. *The Science of Fractal Images*, edited by H. O. Peitgen and D. Saupe (Springer Verlag, New York, 1987).
23. B. B. Mandelbrot, J. Bus. Univ. Chicago **40**, 393 (1967).
24. C.-K. Peng, S. V. Buldyrev, A. L. Goldberger, S. Havlin, F. Sciortino, M. Simons, and H. E. Stanley, Nature **356**, 168 (1992).
25. H. E. Stanley, S. V. Buldyrev, A. L. Goldberger, S. Havlin, S. M. Ossadnik, C.-K. Peng, and M. Simons, Fractals **1**, 283 (1993).
26. W. Li, T. G. Marr, and K. Kaneko, Physica D **75**, 392 (1994).
27. R. F. Voss, Physica D **38**, 362 (1989).

28. B. Dubuc, J. F. Quiniou, C. Roques-Carmes, C. Tricot, and S. W. Zucker, Phys. Rev. A **39**, 1500 (1989).
29. J. Schmittbuhl, J. P. Violette, and S. Roux, Phys. Rev. E **51**, 131 (1995).
30. M. S. Taqqu, V. Teverovsky, and W. Willinger, Fractals **3**, 785 (1995).
31. J.-F. Muzy, Ph.D. thesis, University of Nice, 1993.
32. J.-F. Muzy, E. Bacry, and A. Arneodo, Int. J. of Bifurcation and Chaos **4**, 245 (1994).
33. G. Parisi and U. Frisch, in *Turbulence and Predictability in Geophysical Fluid Dynamics and Climate Dynamics*, *Proc. of Int. School*, edited by M. Ghil, R. Benzi, and G. Parisi (North-Holland, Amsterdam, 1985), p. 84.
34. A. L. Barabási and T. Vicsek, Phys. Rev. A **44**, 2730 (1991).
35. J.-F. Muzy, E. Bacry, and A. Arneodo, Phys. Rev. Lett. **67**, 3515 (1991).
36. A. Arneodo, E. Bacry, and J.-F. Muzy, Physica A **213**, 232 (1995).
37. S. Jaffard, C. R. Acad. Sci. Paris Sér. I **308**, 79 (1989).
38. S. Jaffard, Publicacions Matemàtiques **35**, 155 (1991).
39. M. Holschneider and P. Tchamitchian, in Ref. [71], p. 102.
40. S. Mallat and S. Zhong, IEEE Trans. on Pattern Analysis and Machine Intelligence **14**, 710 (1992).
41. S. Mallat and W. L. Hwang, IEEE Trans. on Information Theory **38**, 617 (1992).
42. E. Bacry, J.-F. Muzy, and A. Arneodo, J. Stat. Phys. **70**, 635 (1993).
43. R. Benzi, G. Paladin, G. Parisi, and A. Vulpiani, J. Phys. A **17**, 3521 (1984).
44. E. B. Vul, Y. G. Sinai, and K. M. Khanin, J. Russ. Math Surveys **39**, 1 (1984).
45. T. C. Halsey, M. H. Jensen, L. P. Kadanoff, I. Procaccia, and B. I. Shraiman, Phys. Rev. A **33**, 1141 (1986).
46. P. Collet, J. Lebowitz, and A. Porzio, J. Stat. Phys. **47**, 609 (1987).
47. R. Badii, Ph.D. thesis, University of Zurich, 1987.
48. G. Paladin and A. Vulpiani, Phys. Rep. **156**, 148 (1987).
49. P. Grassberger, R. Badii, and A. Politi, J. Stat. Phys. **51**, 135 (1988).
50. T. Bohr and T. Tèl, in *Direction in Chaos, Vol. 2*, edited by B. L. Hao (World Scientific, Singapore, 1988), Chap. The thermodynamics of fractals, pp. 194–237.
51. D. Rand, Ergod. Th. Dyn. Sys. **9**, 527 (1989).
52. P. Meakin, in *Phase Transition and Critical Phenomena*, edited by C. Domb and J. L. Lebowitz (Academic Press, Orlando, 1988), Vol. 12, p. 355.
53. B. B. Mandelbrot, J. Fluid Mech. **62**, 331 (1974).
54. C. Meneveau and K. R. Sreenivasan, J. Fluid. Mech. **224**, 429 (1991).
55. Y. G. Sinai, J. Russ. Math Surveys **27**, 21 (1972).
56. R. Bowen, in *Lect. Notes in Maths Vol. 470, No 1* (Springer Verlag, New York, 1975).
57. D. Ruelle, *Thermodynamic Formalism* (Addison Wesley, Reading, 1978).
58. P. Grassberger and I. Procaccia, Physica D **13**, 34 (1984).
59. J. P. Kahane and J. Peyrière, Advances in Mathematics **22**, 131 (1976).
60. G. M. Molchan, Comm. Math. Phys. **179**, 681 (1996).
61. J. D. Farmer, E. Ott, and J. A. Yorke, Physica D **7**, 153 (1983).
62. P. Grassberger and I. Procaccia, Physica D **9**, 189 (1983).
63. R. Badii and A. Politi, J. Stat. Phys. **40**, 725 (1985).
64. G. Grasseau, Ph.D. thesis, University of Bordeaux I, 1989.
65. F. Argoul, A. Arneodo, J. Elezgaray, G. Grasseau, and R. Murenzi, Phys. Rev. A **41**, 5537 (1990).
66. L. V. Meisel, M. Jonhson, and P. J. Cote, Phys. Rev. A **45**, 6989 (1992).
67. A. S. Monin and A. M. Yaglom, *Statistical Fluid Mechanics: Mechanics of Turbulence, Vol II* (MIT Press, Cambridge, MA, 1975).
68. J.-F. Muzy, E. Bacry, and A. Arneodo, Phys. Rev. E **47**, 875 (1993).
69. *Wavelets*, edited by J. M. Combes, A. Grossmann, and P. Tchamitchian (Springer Verlag, Berlin, 1989).
70. Y. Meyer, *Ondelettes* (Herman, Paris, 1990).
71. *Les Ondelettes en 1989*, edited by P. G. Lemarié (Springer Verlag, Berlin, 1990).
72. *Wavelets and Applications*, edited by Y. Meyer (Springer, Berlin, 1992).
73. I. Daubechies, *Ten Lectures on Wavelets* (S.I.A.M., Philadelphia, 1992).
74. *Wavelets and Their Applications*, edited by M. B. Ruskai, G. Beylkin, R. Coifman, I. Daubechies, S. Mallat, Y. Meyer, and L. Raphael (Jones and Barlett, Boston, 1992).
75. C. K. Chui, *An Introduction to Wavelets* (Academic Press, Boston, 1992).
76. *Progress in Wavelets Analysis and Applications*, edited by Y. Meyer and S. Roques (Editions frontières, Gif-sur-Yvette, 1993).

77. A. Arneodo, F. Argoul, E. Bacry, J. Elezgaray, and J.-F. Muzy, *Ondelettes, Multifractales et Turbulences : de l'ADN aux croissances cristallines* (Diderot Editeur, Art et Sciences, Paris, 1995).

78. *Wavelets : Theory and Applications*, edited by G. Erlebacher, M. Y. Hussaini, and L. M. Jameson (Oxford Univ. Press, Oxford, 1996).

79. M. Holschneider, *Wavelets : An Analysis Tool* (Oxford Univ. Press, Oxford, 1996).

80. S. Mallat, *A Wavelet Tour in Signal Processing* (Academic Press, New York, 1998).

81. B. Torresani, *Analyse Continue par Ondelettes* (Editions de Physique, Les Ulis, 1998).

82. M. Holschneider, J. Stat. Phys. **50**, 963 (1988), PhD thesis, University of Aix-Marseilles II, 1988.

83. A. Arneodo, G. Grasseau, and M. Holschneider, Phys. Rev. Lett. **61**, 2281 (1988), in Ref [69], p. 182.

84. A. Arneodo, F. Argoul, J. Elezgaray, and G. Grasseau, in *Nonlinear Dynamics*, edited by G. Turchetti (World Scientific, Singapore, 1989), p. 130.

85. A. Arneodo, F. Argoul, E. Bacry, J. Elezgaray, E. Freysz, G. Grasseau, J.-F. Muzy, and B. Pouligny, in Ref. [72], p. 286.

86. A. Arneodo, E. Bacry, S. Manneville, and J.-F. Muzy, Phys. Rev. Lett. **80**, 708 (1998).

87. A. Arneodo, S. Manneville, J.-F. Muzy, and S. G. Roux, Phil. Trans. R. Soc. London A **357**, 2415 (1999).

88. P. Goupillaud, A. Grossmann, and J. Morlet, Geoexploration **23**, 85 (1984).

89. A. Grossmann and J. Morlet, S.I.A.M. J. Math. Anal **15**, 723 (1984).

90. A. Grossmann and J. Morlet, in *Mathematics and Physics, Lectures on Recent Results*, edited by L. Streit (World Scientific, Singapore, 1985), p. 135.

91. A. Arneodo, E. Bacry, and J.-F. Muzy, Phys. Rev. Lett. **74**, 4823 (1995).

92. A. Arneodo, E. Bacry, S. Jaffard, and J.-F. Muzy, J. Stat. Phys. **87**, 179 (1997).

93. S. Jaffard and Y. Meyer, J. Math. Pures. et Appl. **68**, 95 (1989).

94. S. G. Roux, J.-F. Muzy, and A. Arneodo, Eur. Phys. J. B **8**, 301 (1999).

95. D. Sornette, in *Scale Invariance and Beyond*, edited by B. Dubrulle, F. Graner, and D. Sornette (EDP Sciences and Springer Verlag, Les Ulis and Berlin, 1997), p. 235.

96. E. Bacry, A. Arneodo, U. Frisch, Y. Gagne, and E. Hopfinger, in *Turbulence and Coherent Structures*, edited by M. Lesieur and O. Metais (Kluwer, Dordrecht, 1991), p. 203.

97. M. Vergassola and U. Frisch, Physica D **54**, 58 (1991).

98. M. Vergassola, R. Benzi, L. Biferale, and D. Pisarenko, J. Phys. A **26**, 6093 (1993).

99. S. Jaffard, SIAM J. Math. Anal. **28**, 944 (1997).

100. H. G. E. Hentschel, Phys. Rev. E **50**, 243 (1994).

101. S. F. Edwards and P. W. Anderson, J. Phys. F **5**, 965 (1975).

102. S. G. Roux, Ph.D. thesis, University of Aix-Marseille II, 1996.

103. A. Arneodo, J.-F. Muzy, and S. G. Roux, J. Phys. II France **7**, 363 (1997).

104. A. Arneodo, S. Manneville, J.-F. Muzy, and S. G. Roux, Eur. Phys. J. B **1**, 129 (1998).

105. A. Arneodo, E. Bacry, and J.-F. Muzy, J. Math. Phys **39**, 4142 (1998).

106. R. Benzi, L. Biferale, A. Crisanti, G. Paladin, M. Vergassola, and A. Vulpiani, Physica D **65**, 352 (1993).

107. T. Higuchi, Physica D **46**, 254 (1990).

108. N. P. Greis and H. P. Greenside, Phys. Rev. A **44**, 2324 (1991).

109. G. Wornell and A. V. Oppenheim, IEEE Trans. on Signal Proc. **40**, 611 (1992).

110. J. Beran, *Statistics for Long-Memory Process* (Chapman & Hall, New York, 1994).

111. C.-K. Peng, S. V. Buldyrev, S. Havlin, M. Simons, H. E. Stanley, and A. L. Goldberger, Phys. Rev. E **49**, 1685 (1994).

112. A. Scotti, C. Meneveau, and S. G. Saddoughi, Phys. Rev. E **51**, 5594 (1995).

113. A. R. Mehrabi, H. Rassamdana, and M. Sahimi, Phys. Rev. E **56**, 712 (1997).

114. B. Pilgram and D. T. Kaplan, Physica D **114**, 108 (1998).

115. P. Flandrin, IEEE Trans. on Info. Theory **35**, 197 (1989).

116. P. Flandrin, IEEE Trans. on Info. Theory **38**, 910 (1992).

117. E. Masry, IEEE Trans. on Info. Theory **39**, 260 (1993).

118. P. Abry, P. Goncalvès, and P. Flandrin, Lectures Note in Statistics **105**, 15 (1995).

119. L. Delbeke and P. Abry, Applied and Computational Harmonic Analysis (1998), to appear.

120. P. Abry, P. Flandrin, M. S. Taqqu, and D. Veitch, in *Self-Similarity in Network Traffic*, edited by Parks and W. Willinger (John Wiley and Sons, New York, 1998).

121. A. H. Tewfik and M. Kim, IEEE Trans. on Info. Theory **38**, 904 (1992).

122. J. Pando and L. Z. Fang, Phys. Rev. E **57**, 3593 (1998).

123. I. Simonsen, A. Hansen, and O. M. Nes, Phys. Rev. E **58**, 2779 (1998).

124. C. L. Jones, G. T. Lonergan, and D. E. Mainwaring, J. Phys. A : Math. Gen. **29**, 2509 (1996).

125. B. Audit, E. Bacry, J.-F. Muzy, and A. Arneodo, to be published, 1999.
126. G. Samorodnisky and M. S. Taqqu, *Stable Non-Gaussian Random Processes* (Chapman & Hall, New York, 1994).
127. L. Richardson, Proc. R. Soc. London, Ser A **110**, 709 (1926).
128. A. N. Kolmogorov, C. R. Acad. Sc. USSR **30**, 301 (1941).
129. A. N. Kolmogorov, J. Fluid Mech. **13**, 82 (1962).
130. A. M. Obukhov, J. Fluid Mech. **13**, 77 (1962).
131. D. Schertzer and S. Lovejoy, in *Turbulence and Chaotic Phenomena in Fluids*, edited by T. Tatsumi (North-Holland, Amsterdam, 1984), p. 505.
132. C. Meneveau and K. R. Sreenivasan, Phys. Rev. Lett. **59**, 1424 (1987).
133. D. Schertzer and S. Lovejoy, J. Geophys. Res. **92**, 9693 (1987).
134. S. Kida, J. Phys. Soc. Jpn. **60**, 5 (1990).
135. D. Schertzer, S. Lovejoy, F. Schmitt, Y. Ghigirinskaya, and D. Marsan, Fractals **5**, 427 (1997).
136. E. A. Novikov, Phys. Fluids A **2**, 814 (1990).
137. B. Dubrulle, Phys. Rev. Lett. **73**, 959 (1994).
138. Z.-S. She and E. C. Waymire, Phys. Rev. Lett. **74**, 262 (1995).
139. B. Castaing and B. Dubrulle, J. Phys. II France **5**, 895 (1995).
140. B. Dubrulle, J. Phys. II France **6**, 1825 (1996).
141. B. B. Mandelbrot, C. R. Acad. Sci. Paris Ser A **278**, 289 (1974).
142. B. B. Mandelbrot, C. R. Acad. sci. Paris Ser A **278**, 355 (1974).
143. D. Schertzer and S. Lovejoy, Phys. Chem. Hyd. J. **6**, 623 (1985).
144. S. Lovejoy and D. Schertzer, in Ref. [16], p. 102.
145. T. Vicsek and A. L. Barabási, J. Phys. A: Math. Gen. **24**, L845 (1991).
146. J. Eggers and S. Grossmann, Phys. Rev. A **45**, 2360 (1992).
147. J. A. C. Humphrey, C. A. Schuler, and B. Rubinski, Fluid Dyn. Res. **9**, 81 (1992).
148. A. Juneja, D. P. Lathrop, K. R. Sreenivasan, and G. Stolovitzky, Phys. Rev. E **49**, 5179 (1994).
149. L. Biferale, G. Boffetta, A. Celani, A. Crisanti, and A. Vulpiani, Phys. Rev. E **57**, R6261 (1998).
150. A. Arneodo, B. Audit, E. Bacry, S. Manneville, J.-F. Muzy, and S. G. Roux, Physica A **254**, 24 (1998).
151. A. Arneodo and J.-F. Muzy, Technical report, Science & Finance (unpublished).
152. A. Arneodo, J. P. Bouchaud, R. Cont, J.-F. Muzy, M. Potters, and D. Sornette, preprint cond-mat/9607120 at http://xxx.lanl.gov .
153. P. C. Ivanov, L. A. Nines Amaral, A. L. Goldberger, S. Havlin, M. G. Rosenblum, Z. K. Struzik, and H. E. Stanley, Nature **399**, 461 (1999).
154. A. Arneodo, F. Argoul, E. Bacry, J.-F. Muzy, and M. Tabard, Phys. Rev. Lett. **68**, 3456 (1992).
155. A. Arneodo, F. Argoul, J.-F. Muzy, and M. Tabard, Physica A **188**, 217 (1992).
156. A. Arneodo, F. Argoul, E. Bacry, J.-F. Muzy, and M. Tabard, Fractals **1**, 629 (1993).
157. A. Khun, F. Argoul, J.-F. Muzy, and A. Arneodo, Phys. Rev. Lett. **73**, 2998 (1994).
158. A. Arneodo, E. Bacry, P. V. Graves, and J.-F. Muzy, Phys. Rev. Lett. **74**, 3293 (1995).
159. A. Arneodo, Y. d'Aubenton-Carafa, E. Bacry, P. V. Graves, J.-F. Muzy, and C. Thermes, Physica D **96**, 291 (1996).
160. A. Arneodo, Y. d'Aubenton-Carafa, B. Audit, E. Bacry, J.-F. Muzy, and C. Thermes, Eur. Phys. J. B **1**, 259 (1998).
161. C. Thermes, Y. d'Aubenton-Carafa, B. Audit, C. Vaillant, J.-F. Muzy, and A. Arneodo, Universal multi-scale structural properties of genomic DNA revealed by wavelet analysis, submitted to Nature, 1999.
162. B. Audit, Ph.D. thesis, University of Paris VI, 1999.
163. S. V. Buldyrev, A. L. Goldberger, S. Havlin, C.-K. Peng, and H. E. Stanley, in Ref. [13], p. 49.
164. W. Li and K. Kaneko, Europhys. Lett. **17**, 655 (1992).
165. W. Li, Int. J. of Bifurcations and Chaos **2**, 137 (1992).
166. B. Borštnik, Int. J. of Quantum Chemistry **52**, 457 (1994).
167. M. Y. Azbel', Phys. Rev. Lett. **75**, 168 (1995).
168. H. Herzel and I. Große, Physica A **216**, 518 (1995).
169. R. F. Voss, Phys. Rev. Lett. **68**, 3805 (1992).
170. R. F. Voss, Fractals **2**, 1 (1994).
171. B. Borštnik, D. Pumpernik, and D. Lukman, Europhys. Lett. **23**, 389 (1993).
172. S. Nee, Nature **357**, 450 (1992).
173. V. V. Prabhu and J.-M. Claverie, Nature **357**, 782 (1992).
174. P. J. Munson, R. C. Taylor, and G. S. Michaels, Nature **360**, 635 (1992).

175. S. Karlin and V. Brendel, Science **259**, 677 (1993).
176. C. A. Chatzidimitriou-Dreismann and D. Larhammar, Nature **361**, 212 (1993).
177. D. Larhammar and C. A. Chatzidimitriou-Dreismann, Nucl. Acids Res. **21**, 5167 (1993).
178. R. N. Mantegna, S. V. Buldyrev, A. L. Goldberger, S. Havlin, C.-K. Peng, M. Simons, and H. E. Stanley, Phys. Rev. Lett. **73**, 3169 (1994).
179. A. Czirók, R. N. Mantegna, S. Havlin, and H. E. Stanley, Phys. Rev. E **52**, 446 (1995).
180. R. N. Mantegna, S. V. Buldyrev, A. L. Goldberger, S. Havlin, C.-K. Peng, M. Simons, and H. E. Stanley, Phys. Rev. E **52**, 2939 (1995).
181. A. Czirók, H. E. Stanley, and T. Vicsek, Phys. Rev. E **53**, 6371 (1996).
182. W. Li and K. Kaneko, Nature **360**, 635 (1992).
183. C. L. Berthelsen, J. A. Glazier, and M. H. Skolnick, Phys. Rev. A **45**, 8902 (1992).
184. G. A. Dietler and Y. C. Zhang, Fractals **2**, 473 (1994).
185. J. A. Glazier, S. Raghavachari, C. L. Berthelsen, and M. H. Skolnick, Phys. Rev. E **51**, 2665 (1995).
186. S. V. Buldyrev, A. L. Goldberger, S. Havlin, R. N. Mantegna, M. E. Matsa, C.-K. Peng, M. Simons, and H. E. Stanley, Phys. Rev. E **51**, 5084 (1995).
187. P. Allegrini, M. Barbi, P. Grigolini, and B. J. West, Phys. Rev. E **52**, 5281 (1995).
188. D. S. Goodsell and R. E. Dickerson, Nucl. Acids Res. **22**, 5497 (1994).
189. J. D. Watson, M. Gilman, J. Witkowski, and M. Zoller, *Recombinant DNA* (Freeman, New York, 1992).
190. A. Danchin, La Recherche **24**, 222 (1993).
191. A. Bernot, *L'Analyse des Génomes* (Nathan, Paris, 1996).
192. R. D. Fleischmanm *et al.*, Science **269**, 496 (1995).
193. B. Dujon, Trends Genet. **12**, 263 (1996).
194. J. Carol *et al.*, Science **273**, 1058 (1996).
195. T. Gaasterland, S. Andersson, and C. Sensen, Magpie genome sequencing project list, http://www-fp.mcs.anl.gov/~gaasterland/genomes.html.
196. W. Li, G. Stolovitzky, P. Bernaola-Galván, and J. L. Oliver, Genome Research **8**, 916 (1998).
197. G. M. Viswanathan, S. V. Buldyrev, S. Havlin, and H. E. Stanley, Physica A **249**, 581 (1998).
198. F. R. Blattner *et al.*, Science **277**, 1453 (1997).
199. T. J. Richmond, J. T. Finch, B. Rushton, D. Rhodes, and A. Klug, Nature **311**, 532 (1984).
200. J. Widom and A. Klug, Cell **43**, 207 (1985).
201. Y. Saitoh and U. K. Laemmli, Cold Spring Harb. Symp. Quant. Biol. **58**, 755 (1993).
202. L. D. Murphy and S. B. Zimmerman, J. Struct. Biol. **119**, 336 (1997).
203. J. N. Reeve, K. Sandman, and C. J. Daniels, Cell **89**, 999 (1997).
204. M. R. Starich, K. Sandman, J. N. Reeve, and M. F. Summers, J. Mol. Biol. **255**, 187 (1996).
205. S. L. Pereira, R. A. Grayling, R. Lurz, and J. N. Reeve, Proc. Natl. Acad. Sci. USA **94**, 12633 (1997).
206. K. Luger, A. W. Mader, R. K. Richmond, D. F. Sargent, and T. J. Richmond, Nature **389**, 251 (1997).
207. J. R. Brown and W. F. Doolittle, Microbiol. Mol. Biol. Rev. **61**, 456 (1997).
208. G. J. Olsen and C. R. Woese, Cell **89**, 991 (1997).
209. M. Coca-Prados, H. Y. Yu, and M. T. Hsu, J. Virol. **44**, 603 (1982).
210. M. V. Borca, P. M. Irusta, G. F. Kutish, C. Carillo, C. L. Afonso, A. T. Burrage, J. G. Neilan, and D. L. Rock, Arch. Virol. **141**, 301 (1996).
211. S. A. Stanfield-Oakley and J. D. Griffith, J. Mol. Biol. **256**, 503 (1996).
212. E. N. Trifonov, Physica A **249**, 511 (1998).
213. H. Herzel, O. Weiss, and E. N. Trifonov, Bioinformatics **15**, 187 (1999).
214. G. Meersseman, S. Pennings, and E. M. Bradbury, The EMBO Journal **11**, 2951 (1992).
215. P. T. Lowary and J. Widom, Proc. Natl. Acad. Sci. USA **94**, 1183 (1997).
216. K. J. Polach and J. Widom, J. Mol. Biol. **254**, 130 (1995).
217. A. Grosberg, Y. Rabin, S. Havlin, and A. Neer, Europhys. Lett. **23**, 373 (1993).
218. D. E. Pettijohn, in *Escherichia coli and Salmonella*, edited by F. Neidhardt *et al.* (AMS Press, Washington DC, 1996), p. 158.
219. A. M. Segall, S. D. Goodman, and H. A. Nash, The EMBO Journal **13**, 4536 (1994).
220. N. P. Higgins, X. Yang, Q. Fu, and J. R. Roth, J. Bacteriol. **178**, 2825 (1996).
221. G. Pruss and K. Drlica, Cell **56**, 521 (1989).
222. H. A. Nash, Trends Biochem. Sci. **15**, 222 (1990).
223. R. Kanaar, A. Klippel, E. Shekhtman, J. M. Dungan, R. Khamann, and N. R. Cozzarelli, Cell **27**, 353 (1990).
224. B. Lea-Cox and J. S. Y. Wang, Fractals **1**, 87 (1993).
225. E. Freysz, B. Pouligny, F. Argoul, and A. Arneodo, Phys. Rev. Lett. **64**, 745 (1990).

226. A. Arneodo, F. Argoul, J.-F. Muzy, B. Pouligny, and E. Freysz, in Ref. [74], p. 241.
227. J. P. Antoine, P. Carette, R. Murenzi, and B. Piette, Signal Processing **31**, 241 (1993).
228. J. Canny, IEEE Trans. Patt. Anal. Machine Intell. **8**, 679 (1986).
229. J. Arrault, A. Arneodo, A. Davis, and A. Marshak, Phys. Rev. Lett. **79**, 75 (1997).
230. A. Arneodo, N. Decoster, and S. G. Roux, Phys. Rev. Lett. **83**, 1255 (1999).
231. A. Arneodo, N. Decoster, and S. G. Roux, Eur. Phys. J. B (2000), to appear.
232. N. Decoster, S. G. Roux, and A. Arneodo, Eur. Phys. J. B (2000), to appear.
233. N. Decoster, Ph.D. thesis, University of Bordeaux I, 1999.
234. D. Marr, *Vision* (W. H. Freemann and Co, San-Francisco, 1982).
235. A. Rosenfeld and M. Thurston, IEEE Trans. Comput. C 29 (1971).
236. R. Murenzi, Ph.D. thesis, University of Louvain la Neuve, 1990.
237. R. Murenzi, in Ref. [69], p. 239.
238. M. Ben Slimane, Ph.D. thesis, E.N.P.C., France, 1996.
239. G. Ouillon, D. Sornette, and C. Castaing, Nonlin. Proc. Geophys. **2**, 158 (1995).
240. G. Ouillon, C. Castaing, and D. Sornette, J. Geophys Res. **101**, 5477 (1996).
241. P. Gaillot, J. Darrozes, M. de Saint Blanquat, and G. Ouillon, Geophys. Res. Lett. **24**, 1819 (1997).
242. P. Lévy, *Processus Stochastiques et Mouvement Brownien* (Gauthier-Villars, Paris, 1965).
243. S. Lovejoy, Science **216**, 185 (1982).
244. R. F. Cahalan, in *Advances in Remote Sensing and Retrieval Methods*, edited by A. Deepak, H. Fleming, and J. Theon (Deepak Pub, Hampton, 1989), p. 371.
245. A. Davis, A. Marshak, R. F. Cahalan, and W. J. Wiscombe, preprint (1997).
246. V. Ramanatahn, R. D. Cess, E. F. Harrison, P. Minnis, B. R. Barkston, E. Ahmad, and D. Hartmann, Science **243**, 57 (1989).
247. R. D. Cess *et al.*, Science **245**, 513 (1989).
248. F. S. Rys and A. Waldvogel, in Ref. [3], p.461.
249. R. M. Welch and B. A. Wielicki, Clim. Appl. Meteorol. **25**, 261 (1986).
250. J. I. Yano and Y. Takeuchi, J. Meteor. Soc. Japan **65**, 661 (1987).
251. R. M. Welch, K. S. Kuo, B. A. Wielicki, S. K. Sengupta, and L. Parker, J. Appl. Meteorol. **27**, 341 (1988).
252. R. F. Cahalan and J. H. Joseph, Mon. Wea. Rev. **117**, 261 (1989).
253. G. Sèze and L. Smith, Amer. Meteor. Atmospheric Radiation 47 (1990).
254. A. Davis, S. Lovejoy, and D. Schertzer, in *Scaling, Fractals and Nonlinear Variability in Geophysics*, edited by S. Lovejoy and D. Schertzer (Kluwer, Dordrecht, 1991), p. 303.
255. Y. Tessier, S. Lovejoy, and D. Schertzer, J. Appl. Meteorol. **32**, 223 (1993).
256. A. Davis, A. Marshak, W. J. Wiscombe, and R. F. Cahalan, J. Geophys. Res. **99**, 8055 (1994).
257. W. D. King, C. T. Maher, and G. A. Hepburn, J. Appl. Meteor. **20**, 195 (1981).
258. C. Duroure and B. Guillemet, Atm. Res. **25**, 331 (1990).
259. B. Baker, J. Atmos. Sci. **49**, 387 (1992).
260. S. P. Malinowski and I. Zawadski, J. Atmos. Sci. **50**, 5 (1993).
261. A. V. Korolev and I. P. Mazin, J. Appl. Meteorol. **32**, 760 (1993).
262. S. P. Malinowski, M. Y. Leclerc, and D. G. Baumgardner, J. Atmos. Sci. **51**, 397 (1994).
263. A. Davis, A. Marshak, W. J. Wiscombe, and R. F. Cahalan, J. Atmos. Sci. **53**, 1538 (1996).
264. A. Marshak, A. Davis, W. J. Wiscombe, and R. F. Cahalan, .
265. S. Cox, D. McDougal, D. Randall, and R. Schiffer, Bull. Amer. Meteor. Soc. **68**, 114 (1987).
266. B. A. Albrecht, C. S. Bretherton, D. Jonhson, W. H. Schubert, and A. S. Frisch, Bull. Amer. Meteor. Soc. **76**, 889 (1995).
267. R. Boers, J. B. Jensen, P. B. Krummel, and H. Gerber, Quart. J. Roy. Meteor. Soc. **122**, 1307 (1996).
268. H. W. Baker and J. A. Davies, Remote Sens. Environ. **42**, 51 (1992).
269. A. Davis *et al.*, J. Atmos. Sci. **54**, 241 (1997).
270. R. F. Cahalan and J. B. Snider, Remote Sens. Environ. **28**, 95 (1989).
271. S. Lovejoy, D. Schertzer, P. Silas, Y. Tessier, and D. Lavallée, Ann. Geophysicae **11**, 119 (1993).
272. S. M. Gollmer, M. Harshvardan, and R. F. Cahalan, J. Atmos. Sci. **52**, 3013 (1995).
273. W. J. Wiscombe, A. Davis, A. Marshak, and R. F. Cahalan, Proc. of the Fourth Atmospheric Radiation Measurement (ARM) Science Team Meeting, Charleston, U.S. Dept. of Energy 11 (1995).
274. D. Schertzer and S. Lovejoy, in *Fractals: their physical origin and properties*, edited by L. Pietronero (Plenum, New York, 1989), p. 49.
275. D. Schertzer and S. Lovejoy, in Ref.[10], p. 11.

276. A. Davis, A. Marshak, W. J. Wiscombe, and R. F. Cahalan, Proc. of the 2nd Workshop on Nonstationary Random Processes and Their Applications (1995), preprint.
277. S. G. Roux, A. Arneodo, and N. Decoster, Eur. Phys. J. B (2000), to appear.
278. L. M. Romanova, Izv. Acad. Sci. USSR Atmos. Oceanic Phys. **11**, 509 (1975).
279. A. Davis, Ph.D. thesis, McGill University, Montreal, 1992.
280. R. F. Cahalan, W. Ridgway, W. J. Wiscombe, T. L. Bell, and J. B. Snider, J. Atmos. Sci **51**, 2434 (1994).
281. K. Stamnes, S.-C. Tsay, W. J. Wiscombe, and K. Jayaweera, Applied Optics **27**, 2502 (1988).
282. R. F. Cahalan, W. Ridgway, W. J. Wiscombe, S. Gollmer, and M. Harshvardan, J. Atmos. Sci **51**, 3776 (1994).
283. A. Marshak, A. Davis, W. J. Wiscombe, and R. F. Cahalan, J. Geophys. Res. **100**, 26247 (1995).
284. M. Tiedke, Mon. Wea. Res. **124**, 745 (1996).
285. M. Harshvardan, B. A. Wielicki, and K. M. Ginger, J. of Climate **7**, 1987 (1994).
286. A. Davis, A. Marshak, W. J. Wiscombe, and R. F. Cahalan, in *Current Topics in Nonstationary Analysis*, edited by G. Treviño *et al.* (World Scientific, Singapore, 1996), p. 97.
287. R. F. Cahalan, M. Nestler, W. Ridgway, W. J. Wiscombe, and T. L. Bell, in *Proc. of the 4th International Meeting on Statistical Climatology*, edited by J. Sansom (New Zealand Meteorological Service, Wellington, 1990), p. 28.
288. R. D. Cess, M. H. Zhang, Y. Zhou, X. Jing, and V. Dvortsov, J. Geophys. Res. **101**, 23299 (1996).
289. A. Davis, S. Lovejoy, and D. Schertzer, SPIE Proceedings **1558**, 37 (1991).
290. A. Marshak, A. Davis, W. J. Wiscombe, and G. Titov, Remote Sens. Environ. **52**, 72 (1995).
291. A. Arneodo, S. Manneville, J.-F. Muzy, and S. G. Roux, Applied and Computational Harmonic Analysis **6**, 374 (1999).
292. G. Ruiz-Chavarria, C. Baudet, and S. Ciliberto, Physica **99 D**, 369 (1996).
293. A. Davis, A. Marshak, H. Gerber, and W. J. Wiscombe, J. Geophys. Res. (1998), to appear.
294. C. H. Meong, W. R. Cotton, C. Bretherton, A. Chlond, M. Khairoutdinov, S. Krueger, W. S. Lewellen, M. K. McVean, J. R. M. Pasquier, H. A. Rand, A. P. Siebesma, B. Stevens, and R. I. Sykes, Bull. Am. Meteor. Soc. **77**, 261 (1996).
295. A. Marshak, A. Davis, R. F. Cahalan, and W. J. Wiscombe, Phys. Rev. E **49**, 55 (1994).
296. M. E. Cates and J. M. Deutsch, Phys. Rev. A **35**, 4907 (1987).
297. A. P. Siebesma, in *Universality in Condensed Matter*, edited by R. Julien, L. Peliti, R. Rammal, and N. Boccara (Springer Verlag, Heidelberg, 1988), p. 188.
298. J. O'Neil and C. Meneveau, Phys. Fluids A **5**, 158 (1993).
299. F. Morel-Bailly, M. Chauve, J. Liandrat, and P. Tchamitchian, C. R. Acad. Sci. Paris Sér. II **313**, 591 (1991).
300. H. Markowitz, *Portfolio Selection: Efficient Diversification of Investment* (John Wiley and sons, New York, 1959).
301. R. Merton, *Continuous-Time Finance* (Blackwel, Cambridge MA, 1990).
302. J. C. Hull, *Futures, Options and other Derivatives* (Printice-Hall, Upper Saddle River NJ, 1997).
303. M. L. Bachelier, *Thérie de la Spéculation* (Gauthiers-Villars, Paris, 1900).
304. P. A. Samuelson, *Collected Scientific Papers* (M.I.T. Press, Cambridge MA, 1972).
305. B. B. Mandelbrot, *Fractal and Scaling in Finance: Discontinuity, Concentration, Risk* (Springer, New-York, 1997).
306. R. F. Engle, Econometrica **50**, 987 (1982).
307. T. Bollersev, R. Y. Chous, and K. F. Kroner, J. Econometrics **52**, 5 (1992).
308. R. Mantegna and H. E. Stanley, Nature **376**, 46 (1995).
309. S. Ghashghaie, W. Breymann, J. Peinke, P. Talkner, and Y. Dodge, Nature **381**, 767 (1996).
310. B. Castaing, Y. Gagne, and E. J. Hopfinger, Physica **46 D**, 177 (1990).
311. B. Castaing, Y. Gagne, and M. Marchand, Physica D **68**, 387 (1993).
312. Y. Gagne, M. Marchand, and B. Castaing, J. Phys. II France **4**, 1 (1994).
313. R. Mantegna and H. E. Stanley, Nature **383**, 587 (1996).
314. A. Arneodo, J.-F. Muzy, and D. Sornette, Eur. Phys. J. B **2**, 277 (1998).
315. U. Muller, M. Dacorogna, R. D. Davé, R. B. Olsen, and O. V. Pictet, First International Conference on High Frequency Data in Finance, HFDF I, Zurich (1995).
316. R. B. Barsky and J. B. De Long, The Quaterly Journal of Economics **CVIII**, 291 (1993).
317. S. J. Kon, J. Finance **39**, 147 (1984).
318. B. B. Mandelbrot, A. Fisher, and L. Calvet, Technical report, (unpublished), working paper.
319. *Universality in Chaos*, edited by P. Cvitanovic (Helger, Bristol, 1984).
320. *Chaos*, edited by B. Hao (World Scientific, Singapore, 1984).
321. A. Arneodo, E. Bacry, and J.-F. Muzy, Europhys. Lett. **25**, 479 (1994).